

Laser fabrication and performance of NiCr strain gauges

by

Ningyue Mao

A thesis

presented to the University of Waterloo

in fulfillment of the

thesis requirement for the degree of

Master of Applied Science

in

Mechanical and Mechatronics Engineering

Waterloo, Ontario, Canada, 2022

© Ningyue Mao 2022

Author's Declaration

This thesis consists of material all of which I authored or co-authored: see Statement of Contributions included in the thesis. This is a true copy of the thesis, including any required final revisions, as accepted by my examiners.

I understand that my thesis may be made electronically available to the public.

Statement of Contributions

This thesis was solely written by the candidate. Chapter 5 of this thesis is based on a journal paper that has been published in *Sensors and Actuators A: Physical*:

N. Mao, P.D. Enrique, A.I. Chen, N. Y. Zhou, and P. Peng. Dynamic response and failure mechanisms of a laser-fabricated flexible thin film strain gauge, Sensors and Actuators A: Physical (2022): 113655.

The experimental design, sample preparation, sample characterization, analysis, and writing of the manuscript were conducted by the candidate. Prof. P.D. Enrique assisted with the interpretation of the results and writing of the manuscript. Dr. Albert I.H. Chen provided resources and technical expertise in strain gauge testing. Prof. Norman Zhou and Prof. Peng Peng provided resources and supervision for the research and edited and reviewed the manuscript.

Abstract

Increasing demand for smart devices has spurred the development of advanced sensors with smaller and more adaptable form factors. The integration of thin film technology into sensors such as strain gauges has the potential to reduce their size and allow their use in flexible applications. Laser patterning is a promising choice to replace the conventional lithography-based method for flexible microelectronic fabrications, due to its low process complexity, short development cycle for custom sensor designs and the ability to pattern on three-dimensional (3D) surfaces with high structure resolution.

The laser ablation process of NiCr film was investigated in detail by the study of the influence of laser parameters and theoretical analysis. The average power, repetition frequency, scanning speed, and pulse overlap were found to be significant parameters in controlling the quality and dimensional accuracy of ablated microchannels. An empirical threshold fluence was derived from an analytical analysis of the ablation process. This threshold value allows for predicting the geometry of the ablated structure based on the selected processing parameters. In addition, a numerical model was created in COMSOL Multiphysics to analyze the material removal process and the final geometry of the ablated structure with different laser parameter sets. Generally, ablation with a higher frequency and slower speed results in a smoother bottom surface of the ablated microchannel. The findings can be utilized to establish a process map that allows for the selection of parameters according to dimensional and structural requirements.

The laser patterning process was used to fabricate a 1025 Ω flexible thin film strain gauge using NiCr film. The characteristics and dynamic tensile response of the laser fabricated strain gauge were evaluated. The strain gauges exhibit sensitivity comparable to commercially available NiCr-based strain gauges and can reliably survive 10^6 cycles up to 1750 $\mu\epsilon$. Several failure mechanisms were identified, and these findings provide a guide to diagnose thin film strain gauge failures. Strain gauges fabricated by this unconventional technique have shown their potential for use in long-term dynamic load sensing applications.

Acknowledgements

First of all, I would like to express my sincere gratitude to my supervisor Prof. Peng Peng for his guidance and mentorship throughout my study. I would like to thank Prof. Norman Zhou and Dr. Robert Liang for giving me the opportunity to join the Centre for Advanced Materials Joining (CAMJ) group as a co-op student. A special thank you to Prof. Pablo Enrique for his advice on experiments and his assistance in drafting the manuscript. I would also like to thank my colleagues and friends at the CMAJ, for their help in the lab and inspiring discussions.

I would like to thank Dr. Albert Chen from Forcen Inc. for providing resources and feedback for this project.

I would like to thank my family for encouraging me to continue my study and providing financial support. Finally, I would like to thank my husband Jiayu for his support both academically and emotionally, you make me a better and more confident person.

Table of Contents

Author's Declaration.....	ii
Statement of Contributions	iii
Abstract.....	iv
Acknowledgements.....	v
List of Figures.....	viii
List of Tables	xi
Chapter 1 Introduction	1
1.1 Background	1
1.2 Thesis objective.....	2
1.3 Thesis overview.....	3
Chapter 2 Literature Review	4
2.1 Laser ablation	4
2.1.1 Fundamental process parameters.....	4
2.1.2 Laser-material interactions	7
2.1.3 Advantages of UV laser micromachining	10
2.2 Fundamentals and fabrication of strain gauge.....	11
2.2.1 Classification and strain sensing mechanism	11
2.2.2 Conventional fabrication method	15
2.2.3 Alternative fabrication methods	17
2.2.4 Thin film patterning by laser ablation	18
Chapter 3 Effect of laser parameters on the ablation process of NiCr films on polyimide	20
3.1 Introduction.....	20
3.2 Materials and methods	20
3.3 Experimental results and discussion	22
3.3.1 Ablation width	22
3.3.2 Ablation depth	24
3.3.3 Surface morphology	27
3.3.4 Cross-section profile.....	31
3.4 Summary	32

Chapter 4 Theoretical analysis of pulsed laser ablation process.....	33
4.1 Introduction.....	33
4.2 Analytical method.....	33
4.2.1 Theory.....	33
4.2.2 Effect of laser fluence.....	36
4.2.3 Effect of pulse overlap.....	40
4.3 Finite element simulations.....	44
4.3.1 Governing equations.....	44
4.3.2 Finite element model setup.....	46
4.3.3 Results and discussion.....	49
4.4 Summary.....	56
Chapter 5 Dynamic response of laser fabricated strain gauge.....	58
5.1 Introduction.....	58
5.2 Materials and methods.....	58
5.2.1 Strain gauge fabrication.....	58
5.2.2 Mechanical testing setup.....	59
5.2.3 Characterization.....	61
5.3 Results and discussion.....	61
5.3.1 Strain gauge characterization.....	61
5.3.2 Cyclic resistance response.....	64
5.3.3 Failure mechanisms.....	66
5.4 Summary.....	72
Chapter 6 Conclusion.....	73
6.1 Conclusion.....	73
6.2 Recommendation for future work.....	74
References.....	76

List of Figures

Figure 1. Illustration of output power of a) CW laser and b) pulsed laser.	5
Figure 2. Experimental irradiance profiles of a laser beam with a Gaussian beam profile (left) and flat-top beam profile (right). [24].....	7
Figure 3. Physical processes involved during laser irradiation, including reflection, absorption, and transmission. [17]	8
Figure 4. a) Long pulse and b) ultra-short pulse laser interaction with target material. [31] ...	9
Figure 5. The characteristic design of a metal-based strain gauge with a) wire and b) etched foil measuring grid (a-carrier material, b-measuring grid, c-connections, d-effective grid length). [39].....	12
Figure 6. Fabrication process of NiCr strain gauges using lithography method [57].....	17
Figure 7. a) Flatbed screen printing with planar substrate; b) Rotary screen printing with moving substrate; c) Inkjet printer. [59]	18
Figure 8. Thin film strain sensors on a complex surface: a) The 3D scanning trajectory visualized in a CAD program and b) results of laser patterning process on a component surface. [67]	19
Figure 9. Schematic diagram of the experimental setup.....	21
Figure 10. The effect of a) power, b) frequency, and c) scanning speed on ablation width with error bars representing standard errors.	22
Figure 11. A comparison of actual and predicted ablation width using the response surface model.....	23
Figure 12. The effect of a) power, b) frequency, and c) scanning speed on ablation depth with error bars representing standard errors.	25
Figure 13. A comparison of actual and predicted ablation depth using the response surface model.....	26
Figure 14. Comparison of surface morphology of the ablated channels by different scanning speeds and different pulse energy. a-f) 6.67 μJ ; g-l) 2.67 μJ	28
Figure 15. Microscopic images of laser ablated channels with various average power, frequency, and scanning speed.	30
Figure 16. Comparison of the ablated channels' cross-section profile with pulse energy of 9.33 μJ and different scanning speeds.	31

Figure 17. A circular Gaussian beam profile creates an ablated spot with a diameter of d if an ablation threshold $F_{th} < F_0$ exists.....	35
Figure 18. a) Ablation depth and b) ablation width squared versus the laser fluence calculated from Equation 4-8 with different frequencies.....	37
Figure 19. Illustration of area exposed by the laser in one cycle.....	37
Figure 20. a) Ablation depth and b) ablation width squared versus the fluence calculated from Equation 4-9 with different frequency.....	38
Figure 21. Illustration of area exposed by multiple laser pulses.....	38
Figure 22. a) Ablation depth and b) ablation width squared versus the fluence calculated from Equation 4-12 with different frequencies.	39
Figure 23. Illustration of different pulse overlap conditions.	41
Figure 24. a) Ablation depth and b) ablation width squared versus the fluence calculated from Equation 4-12 with different pulse overlap conditions.....	42
Figure 25. Threshold fluence as a function of scanning speed for experimentally obtained depth and width.....	44
Figure 26. Two-dimensional geometry for the computational model.	46
Figure 27. Free triangular mesh of the NiCr film.	49
Figure 28. Ablation morphology at $t =$ a) 47 ns, b) 13.301 μ s, c) 13.39 μ s, d) 26.665 μ s, e) 26.74 μ s, f) 40.04 μ s, g) 40.09 μ s and h) 399.97 μ s with $P_{avg} = 0.7$ W, $f = 75$ kHz, $P_w = 47$ ns, $V = 300$ mm/s.....	51
Figure 29. a) Cross-sectional profiles of the ablation geometry after different number of pulses; b) The simulated maximum ablation depth versus number of pulses.....	52
Figure 30. Ablation morphology at $t =$ a) 47 ns, b) 13.34 μ s, c) 13.39 μ s and d) 53.29 μ s with $P_{avg} = 0.7$ W, $f = 75$ kHz, $P_w = 47$ ns, $V = 600$ mm/s.....	53
Figure 31. a) Cross-sectional profile of the ablation geometry at 0.7 W, 75 kHz with various scanning speeds; b) Comparison of experimental and simulated maximum ablation depth at different scanning speeds.....	54
Figure 32. a) Cross-sectional profile of the ablation geometry at 0.6 W, 400 mm/s with various frequencies; b) Comparison of experimental and simulated maximum ablation depth at different frequencies.	55
Figure 33. Simulated versus experimental maximum ablation depths.	56

Figure 34. Schematic of the flexible thin-film strain gauge fabrication process. a) the flexible polyimide substrate; b) PVD deposition of the metallic NiCr layer; c) laser patterning of the strain gauge, d) laser fabricated thin-film strain gauge, and e) photo of fabricated strain gauge array. 59

Figure 35. Schematic of experiment setup for a) gauge factor testing and b) dynamic testing. 61

Figure 36. SEM images showing a) the strain gauge overview and terminology, b) higher magnification image of the traces, and c) a tilted view of the traces..... 62

Figure 37. Example of three tensile gauge factor tests. The green (dashed) and yellow (solid) lines show the expected almost-linear response, while the red dotted line shows an apparent increase in the gauge factor caused by crack opening. 64

Figure 38. Results of fatigue testing of strain gauges at various strains. Tests were typically interrupted around 10^6 cycles, at which point they were considered runout samples. 65

Figure 39. Cyclic response for strain gauges with a) no failure and b) open circuit failure, with higher magnification of the response curve shown in c) and d), respectively..... 66

Figure 40. Crack networks viewed from a) above and b) at an angle after cyclic bending loading..... 67

Figure 41. Comparison of individual conductive traces' resistance at flat and bent conditions for a) as-fabricated strain gauges and b) fatigue-tested strain gauges. 69

Figure 42. a) Response degradation failures showing upward shift in unstrained resistance while maintaining a constant peak resistance; b) schematic of crack and delamination after strain being released, and c) SEM image of delamination and crack in traces..... 70

Figure 43. a) Resistance response showing upward shift in baseline with increasing peak resistance; b) schematics showing a crack from initial unstrained condition, crack opening during bending, and crack remaining partially open after stress release; c) SEM image of a crack in the unstrained position. 71

List of Tables

Table 1. Properties of sensors based on metal-foil and silicon. [46]	14
Table 2. Summary of laser parameters used in this study.....	21
Table 3. Response surface model results for ablation width.	24
Table 4. Statistics for ablation width model in Table 3.	24
Table 5. Response surface model results for ablation depth.....	25
Table 6. Statistics for ablation depth model in Table 5.	26
Table 7. Fit parameters for laser fluence and ablation depth relationship.	40
Table 8. Fit parameters for laser fluence and ablation width relationship.....	40
Table 9. Comparison of the empirical threshold fluences for different pulse overlap conditions.....	42
Table 10. Fit parameters for threshold laser fluence and scanning speed relationship.....	44
Table 11. Material properties of NiCr and laser processing parameters.....	47
Table 12. Boundary conditions of the heat transfer model.	48
Table 13. Fit parameters of laser fluence and simulated ablation depth relationship.....	56
Table 14. Dimensions of the conductive path as described in Figure 36a.....	63

Chapter 1 Introduction

1.1 Background

Industrial and consumer demand has driven the adoption of the Internet of Things (IoT), integrating sensors for real-time data capture in a wide range of applications. The ability to measure deformation acting on a surface is useful in applications including monitoring of building and structure health [1], monitoring human health [2], and facilitating human-machine interactions [3]. This is often done with the use of a strain gauge, a device capable of measure the strain of a surface under force, pressure, and torque loads by converting mechanical distortion into an electrical signal. The principal sensing mechanism comes from the dimensional change that occurs when a strain is applied, which causes the electrical resistance of the sensor to change. With the use of a thin film sensing layer, the size of large resistance strain gauges can be greatly reduced, meaning the strain gauge would have negligible mechanical stiffness [4] and is minimally intrusive. Compared to traditional rigid sensors, flexible thin film strain gauges can be applied to arbitrarily curved surfaces such as human skin and robotic arms and can measure a larger range of deformation.

Conventional strain gauges are typically fabricated using lithography-based techniques, involving slow development cycles, and harsh chemicals. This fabrication process also requires a controlled environment, and specialized training and equipment, which increases the manufacturing complexity and cost. Although lithographic patterning offers high structure resolution quality, its conformality is not good enough to be used on curved surfaces. Alternative fabrication methods that can alleviate the limitations associated with conventional lithography-based techniques are under investigation, such as additive printing [5], direct-write thermal spray (DWTS) [6] and thin-film patterning by laser ablation [7,8]. The common drawback with other fabrication methods is that although the complexity and cost of fabrication can be reduced, the resolution is sacrificed.

Among these methods, laser patterning has shown great potential as a promising alternative. This method is a single-step process that removes the material directly through solid-vapor ablation induced by a pulsed laser, minimizing the thermal damage to the surrounding materials. The complexity and cost of the process are greatly reduced since a mask or ink is not

required and a short turnaround time for custom sensor designs is possible. This technique is also capable of patterning on three-dimensional surfaces with high structure resolution [9].

Process optimization for laser patterning is a challenging process, as this method is influenced by various factors, including but not limited to laser beam properties, film and substrate material properties, pulse energy, and scanning speed. Also, since it is an extremely fast dynamic laser-material interaction process, it is usually hard to make in-situ observations during the experiments. The trial-and-error process of designing experiments to find the optimal processing parameters and strategies in existing studies is time-consuming and costly. The obtained processing parameters are often not replicable to other sensor designs with different film thicknesses because the required ablation depths to achieve complete galvanic insulation between separated structures without any damage to the underlying substrate are different. Hence, the laser ablation process needs to be further studied to better understand the process and facilitate the selection of optimal processing parameters.

Sensitivity and reliability are two key characteristics of flexible strain gauges. Generally, the electrical and mechanical properties of thin films are not identical to those in the bulk form [10], such that special consideration should be taken to evaluate the properties of thin-film strain gauges. The effect of cyclic loading on the electrical response and fatigue failure of thin film strain gauges has not been well studied and is critical if they are to be widely implemented in industrial and consumer applications.

1.2 Thesis objective

The objective of this thesis is to develop an alternative fabrication method for flexible thin film sensors on polymer substrates, using pulsed laser for patterning, which reduces the complexity and cost of fabrication and alleviates the limitations of the conventional lithography-based technique. This thesis investigates various factors that influence the laser patterning process and evaluates the characteristics of the laser fabricated strain gauges. The specific objectives are as follows:

1. Explore the role of laser average power, repetition frequency, and scanning speed on the NiCr film ablation process to obtain optimal processing parameters.
2. Establish a process map that allows for the selection of parameters according to dimensional and structural requirements.

3. Investigate the performance of laser fabricated strain gauges through sensitivity and reliability testing.

1.3 Thesis overview

The thesis is organized into six chapters.

Chapter 2 presents a background review on the fundamentals of laser processing parameters and mechanisms of laser-material interaction, classification and sensing mechanisms of strain gauges, and various fabrication methods for thin film sensor fabrication.

Chapter 3 explores the effect of laser parameters on the laser ablation process through an experimental study. The relationship between various parameters and resulting ablation depth and width are quantified using response surface methodology.

Chapter 4 introduces two theoretical models, including an analytical method which relates the dimension of ablated structure with incident laser fluence, and a finite element model to reveal the material removal process.

Chapter 5 investigates the sensitivity and resistance response of the laser fabricated strain gauge towards varying dynamic loads. The failure mechanisms of thin film strain gauges are also discussed.

Chapter 6 summarizes the main findings presented in this thesis and proposes future work to complement this study.

Chapter 2 Literature Review

2.1 Laser ablation

Laser ablation is the thermal or nonthermal process of irradiating a solid with an intense continuous wave (CW) or pulsed laser beam to selectively remove materials. Ablation occurs only when the material absorbs enough energy to be melted or vaporized. It can be used for cleaning [11], cutting [12], grain-refining in welding [13], drilling [12], surface treatment and modification [14] of various materials with remarkable precision in micro- and nanoscale. The history of laser ablation began with the discovery of the first working laser, a ruby laser, by Theodore Maiman in 1960 [15]. It was discovered in 1965 that diamond drilling could be achieved by using laser ablation mechanisms [16]. Also, the process of laser beam irradiation has been further investigated in the mid-1960s, and it was found that electrons, ions and neutral atoms removed from the solid surface form a glowing plasma near the surface with a temperature of $10^3 - 10^4$ K [17]. From the 1960s to the 1970s, there were mainly CW or long-pulsed lasers such as CO₂ and Nd:YAG laser equipment that is typical of high-power laser systems. Laser welding technology was developed in the 1970s, attributed to the sufficient laser power and energy density to melt metals [18]. The application of laser equipment further expands with the development of lasers with high-energy density and short wavelengths in the 1980s to 1990s [17], which is particularly useful for film deposition. In laser ablation for material processing, a nonthermal effect was observed with the enhanced laser power density and shortened pulse duration. In the 1980s, ultraviolet (UV) excimer lasers with nanosecond or picosecond pulse width could perform many precise processing tasks, such as drilling, etching and surface heat treatment on metallic and nonmetallic materials such as polymers and ceramics [19,20]. The processing precision can be greatly improved with a short-wavelength laser since the laser beam can be easily focused on a small area.

2.1.1 Fundamental process parameters

Over the years, significant advances in laser material processing technology have been achieved due to the full utilization of the laser properties, the characteristics of the beam delivery system and the inherent properties of the propagating coherent light. These aspects can be classified according to the controllable parameters commonly used in materials processing, such as wavelength, energy/power fluence, processing beam character, and spatial and temporal

properties. The optimal laser wavelength for a given use case mainly depends on the application. Since different materials have unique wavelength-dependent absorption properties in materials processing, the interaction between the laser and materials is different. In general, shorter wavelength lasers facilitate the creation of small and precise features with minimal peripheral heating, due to the smaller focused spot [21]. Therefore, laser sources with shorter wavelengths are more suitable for precise material processing.

Considering the properties of light propagation, there are two desired characteristics of the laser for ablation applications, which are the monochromaticity and directionality of the beam [22]. The monochromaticity means all emitted light has the same wavelength; this consistent wavelength is very practical for the analysis of the laser-material interactions. The directionality means the laser beams have a small beam divergence angle, which results in better controllability and easier focusing [22].

The pulsed laser is the most widely used type of laser for the ablation process. Compared to the CW laser, whose output is continuous once the laser is turned on, the output of the pulsed laser only lasts for a short duration ranging from milliseconds to femtoseconds with no emission between pulses (Figure 1).

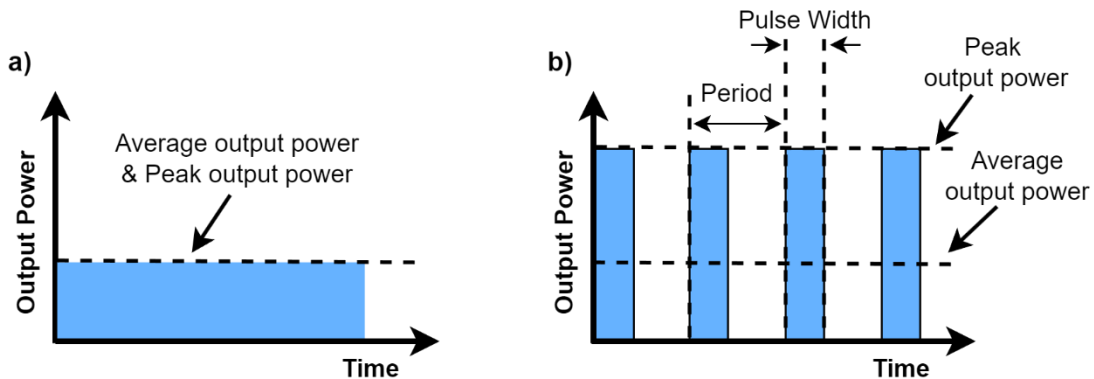


Figure 1. Illustration of output power of a) CW laser and b) pulsed laser.

Given the same average output power, the peak output power of a pulsed laser beam is much higher than that of a CW laser beam, which is identical to the average power. Pulse energy (E) is a commonly used measure to evaluate the total emission of a single pulse that is the only light emitted by the laser over the entire period and can be calculated from the average power

(P_{avg}) using Equation 2-1. The peak power (P_{peak}) for a pulsed laser is dependent on its pulse energy and pulse width (τ), also called pulse duration, which is the time measured across a pulse at the beam's full width half maximum (FWHM) and it can be determined by Equation 2-2. Theoretically, based on the relation between parameters, short pulses and long periods may protect the irradiated samples from being overheated by allowing them to cool down between light emission pulses. On the other hand, even with moderate peak power, long pulses and short periods could deliver large total energy.

$$E = \frac{P_{avg}}{f} \quad (2-1)$$

$$P_{peak} \approx \frac{E}{\tau} \quad (2-2)$$

Besides the parameters of the laser system, the shape and quality of laser beams also play important roles in ablation. A laser beam's diameter, often defined at the $1/e^2$ width of the beam, is directly related to laser fluence and has a significant impact on the ablation process. The fluence is a quantitative measure of total laser energy over the area represented by the focal spot size and is typically measured in $J\ cm^{-2}$ [22]. Hence, a smaller beam diameter would lead to a higher energy density. The intensity distribution of the laser beam not only controls the laser pulse duration and beam diameter, but also determines the formed structure on the ablated sample material. Two common beam profiles are Gaussian and flat-top beams (Figure 2). Realistically, no laser can produce a perfectly Gaussian or perfectly flat-top beam whose beam profile matches its characteristic function perfectly, since there are always some fluctuations inside a laser. The difference between a laser's actual beam profile and that of an ideal beam is often described by the beam quality (M^2) factor, which is defined as:

$$M^2 = \frac{\pi\omega_0\theta}{\lambda} \quad (2-3)$$

where ω_0 is the beam waist, θ is the divergence angle of the laser and λ is the laser wavelength. An M^2 factor of 1 represents an ideal Gaussian beam, while an M^2 factor greater than 1 corresponds to deviation from an ideal Gaussian beam and a factor less than 1 cannot be achieved. The M^2 factor can also be used to estimate the actual radius of the beam as it propagates by

replacing the theoretical laser wavelength with the wavelength multiplied by the M^2 factor in the Gaussian beam propagation equations [23].

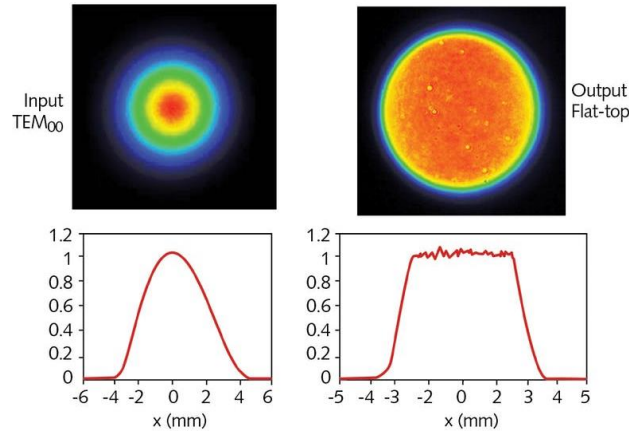


Figure 2. Experimental irradiance profiles of a laser beam with a Gaussian beam profile (left) and flat-top beam profile (right). [24]

In addition, the position of the laser focus on the sample material would also influence the ablation efficiency, ablation shape and morphology of the formed structure on the surface [25]. Wang et al. compared the effect of two typical focus positions, and it was reported that the convergent beam results in better surface quality of the ablation shape than that ablated by the divergent beam [26].

2.1.2 Laser-material interactions

The laser-material interaction is an interdisciplinary and complicated subject [27] and it greatly relies on the time scale of the laser pulse duration, which is also a common way to classify laser source. The pulsed lasers are classified into millisecond (10^{-3} s), microsecond (10^{-6} s), nanosecond (10^{-9} s), picosecond (10^{-12} s) and femtosecond (10^{-15} s) lasers. Different laser pulse duration would differ the interactions between laser and target material and so ablates material based on varying mechanisms.

Several physical processes are involved when a laser irradiates the target surface, such as reflection, dispersion, absorption and transmission. As shown in Figure 3, $P_0, P_R, P_\zeta, P_\beta$ are the total incident energy, the reflected energy, the transmitted energy and absorbed energy, respectively. These energy components can be related as follows based on the energy conservation rule:

$$P_0 = P_R + P_\beta + P_\zeta \quad (2-4)$$

or

$$\frac{P_R}{P_0} + \frac{P_\beta}{P_0} + \frac{P_\zeta}{P_0} = R + \beta + \zeta = 1 \quad (2-5)$$

where R is the reflectivity, β is the absorbance, ζ is the transmittance, respectively. Typically, the laser ablation phenomenon occurs when the energy absorbed by the target reaches a specific value (ablation threshold).

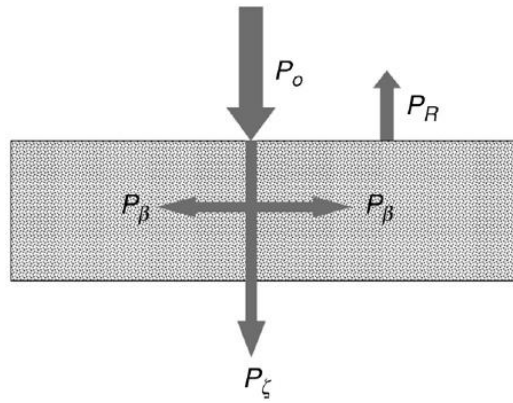


Figure 3. Physical processes involved during laser irradiation, including reflection, absorption, and transmission. [17]

There have been various proposed mechanisms for explaining the laser ablation process, which is a special interaction between laser radiation and matter that is not only affected by laser parameters (output power, wavelength, etc.) but also depends on the physical properties of the material (e.g., optical properties such as reflectivity, absorbance, and thermal properties such as thermal conductivity and specific heat capacity). For CW and long-pulsed (ns) lasers, when it irradiates on a target, most of the laser energy is accumulated on the surface and part of the energy is absorbed by a thin layer under the irradiated surface which causes a continuous increase of the surface temperature. Simultaneously, the energy further penetrates into the target and so the thickness of the heated region increases. The temperature gradient gets smaller and gradually decreases the heat conduction rate until zero as the thickness increases. That is, the laser heat energy can only penetrate to a certain thickness of the target, and it is defined as the thermal diffusion depth [28]. If the laser energy density is high enough, the excited electrons will transfer

energy to the lattice through collisions and result in the target heating up. Hence, the thermal motion of some atoms in the lattice is accelerated and these high-energy atoms can overcome the attraction of their neighbors, causing physical phenomena such as melting, vaporization, or boiling to occur, which indicates the beginning of ablation. The vapor formed above the irradiated surface contains atoms, molecules, some clusters, micrometer-sized droplets and solid particles, which continuously absorb laser energy until ionization takes place and a plume is produced near the surface [17]. The temperature of the irradiated surface is mainly affected by the vaporization mechanism. In brief, the CW and long-pulsed laser ablation is dominated by photothermal reaction (Figure 4a), however, the actual physical process of the interaction between the laser and the target is much more complex than the process described above. Other complicated processes happen simultaneously such as electron excitation effects, photoelectronic effects and atom or cluster emission, etc. [29,30]. In addition, for long-pulsed laser ablation, the threshold is greatly affected by dopants and various defects in the lattice because of the dependence of the avalanche ionization and so the ablation threshold is different for different materials [17].

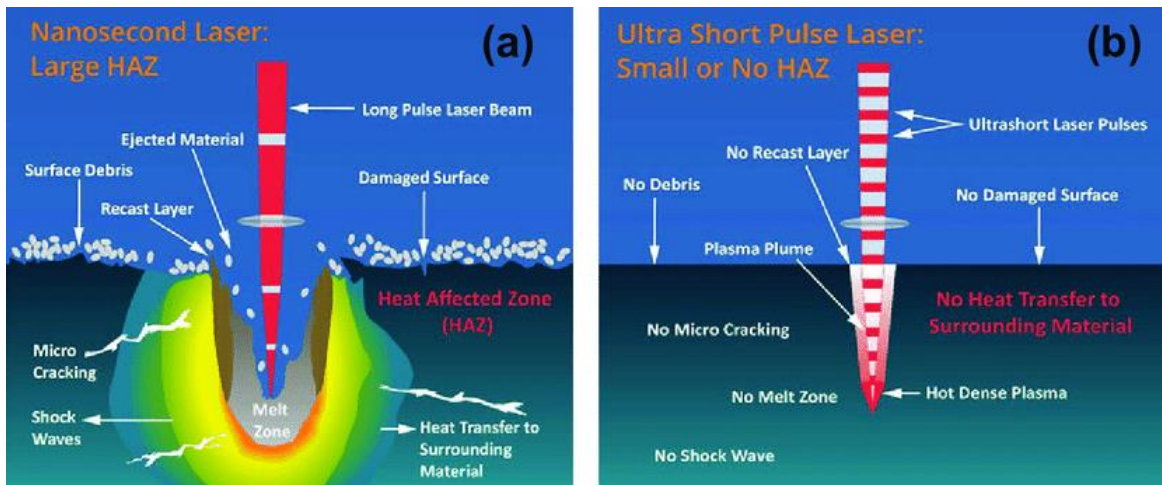


Figure 4. a) Long pulse and b) ultra-short pulse laser interaction with target material. [31]

The physical mechanism of femtosecond laser ablation is quite different from nanosecond laser ablation due to the effect of ultrashort pulse duration (Figure 4). The impact of the relaxation time of electron-phonon interaction, which is on the order of a picosecond, needs to be considered in the case where the pulse duration time is less than a picosecond [32]. The initial phase of the ablation process is similar to long-pulsed laser ablation, when the femtosecond laser focuses on

the surface of the target, the electrons absorb the photon energy and accelerate, leading to a dramatic increase in temperature. However, during the short pulse, there is no time for electrons to transfer the obtained energy to the lattice. Therefore, the temperature of the lattice subsystem keeps relatively low, while the electron subsystem has very high energy, in which ionization is dominating for material removal instead of vaporization, resulting in a ‘cold’ ablation. Compared to long-pulsed laser ablation, the femtosecond laser ablation process produces electrons primarily by multiphoton ionization or tunneling ionization mechanisms [17]. Also, in this case, the doped impurities and defects only have a small impact on the generation and recombination of electron and vacancy pairs, hence, the ablation thresholds for different materials are similar for femtosecond laser ablation [33].

2.1.3 Advantages of UV laser micromachining

The laser wavelength is one of the critical factors to be considered when choosing the laser source for a specific field of application. In general, long-wavelength lasers are not suitable for metal ablation, as most of the incident laser energy will be reflected by the metal surface. Thus, short-wavelength lasers are more efficient to ablate metals or other energy-reflective materials. One of the good candidates for metal ablation is a short-pulsed UV laser with a short wavelength. There are two main types of UV lasers. The first type is the solid-state laser with special crystals, such as neodymium-doped yttrium aluminum garnet (Nd: YAG) and neodymium-doped yttrium orthovanadate (Nd: YVO₄) to change the infrared 1064nm wavelength to the ultraviolet wavelength. The other type is the excimer laser, which emits fast electrical discharge in a high-pressure mixture of a rare gas and a halogen gas [34]. In contrast to solid-state laser, the excimer laser has the advantages of higher pulse energy, shorter pulse duration and shorter wavelength. However, since the optical modes of excimer lasers are worse than the solid-state laser and their repetition frequency is also much lower, the beam diameter and resulting heat-affected zone are relatively larger. Hence, it is difficult to fabricate high-precision patterns by focusing excimer laser beams directly. Fine patterns with high resolution can be achieved with the aid of a pattern mask and a special optical system to homogenize the excimer laser beam [35].

Besides photothermal ablation, UV lasers can modify the surface of a material through direct chemical bond breaking [36]. When the absorbed photon energy by the material is greater

than the chemical bond energy of the material, photochemical ablation occurs and so minimizing the heat effects on the surrounding material. The energy of the laser beam can be calculated as:

$$E = \frac{hc}{\lambda} \quad (2-6)$$

where E is the photon energy, h is the Planck constant (6.626×10^{-34} J s), c is the speed of light (3×10^8 m/s) and λ is the laser wavelength. The photon energy increases as the wavelength decreases. This feature makes UV laser micromachining very attractive for ablating polymeric materials, and small-feature patterning applications, as thermal damage to the non-processed area can be dramatically reduced and so produce tiny features with sharp and clean edges that would be melted away by thermal processing. Another distinct advantage of UV lasers over longer-wavelength laser sources is the superior spatial resolution. Since the minimum spot size of a focused laser beam increases with longer wavelengths and deterioration of beam quality, UV lasers with high beam quality can be used to fabricate small features at the micron and submicron scale.

2.2 Fundamentals and fabrication of strain gauge

2.2.1 Classification and strain sensing mechanism

Strain sensors are a class of electronic devices, which transduce external mechanical stimuli into output electrical signals. It is widely used to measure the amount of distortion in a component under loading. There are many types of strain sensors including but not limited to resistive, capacitive, and piezoelectric [37,38]. However, most conventional strain sensors are resistive, they are well developed and used commercially.

Two major types of sensing materials are metallic (including metals and metal alloys) and semiconducting. Metals were first studied and then expanded to semiconductors with evolving fabrication techniques. Both materials convert mechanical strain into a change in electrical resistance. When they deform, the electrical resistance changes as a function of the applied mechanical strain. After releasing strain sensors from tensile/compressive strains, the resistance recovers to its initial value and this process is reversible so the deformation state can be easily measured by recording changes in the electrical resistance of resistive strain sensors. However, these two types of materials have different mechanisms for resistance change.

Metal-based resistive strain sensors were first introduced in the early 1940s, which consist of a nichrome wire bonded to a paper backing [39]. The typical design of the resistive strain gauges used today differs little from earlier iterations of the sensor, typically consisting of a wire or metal foil as the strain sensing element in a meandering pattern (Figure 5). The metallic strain gauge shows great linearity and stability over time for both static and dynamic strain measurements of up to 5%, such as small deformations in composite materials and rigid bodies [40].

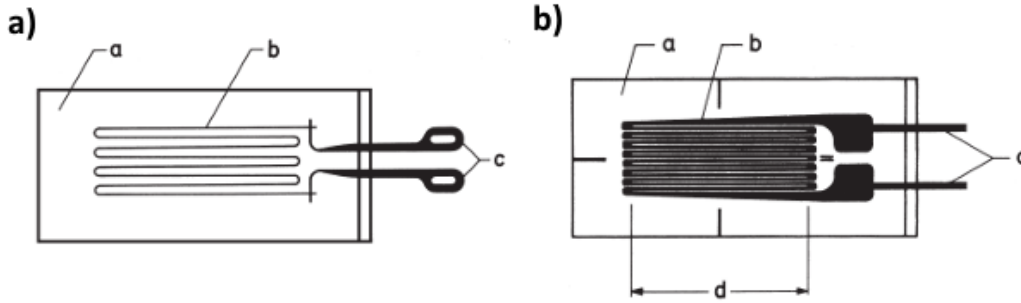


Figure 5. The characteristic design of a metal-based strain gauge with a) wire and b) etched foil measuring grid (a-carrier material, b-measuring grid, c-connections, d-effective grid length). [39]

It is common to express the strain gauge's sensitivity in terms of the relative change of resistance, this quantity is known as the gauge factor (GF) and is generally given by the following equation,

$$GF = \frac{\Delta R/R_0}{\varepsilon} \quad (2-7)$$

where R is electrical resistance and ε is the applied strain. For metals, the variation in resistance is primarily due to the dimensional changes in the device. When materials are stretched, they tend to elongate along the direction of stretching and contract in the transverse direction based on Poisson's ratio. According to the equation of electrical resistance (Equation 2-8),

$$R = \frac{\rho l}{A} \quad (2-8)$$

where ρ is the electric resistivity of the material, l is the length and A is the cross-sectional area; when the strain gauge is subjected to a tensile load, its length would increase and the cross-sectional area would shrink, leading to an increase in resistance. Since the resistance change of

metal strain gauge is primarily geometry dependent, the gauge factor equation could be expressed as a function of Poisson ratio (ν), described in Equation 2-9. The gauge factors of metal strain sensors usually range from 2 to 6 [41].

$$GF = \frac{(1 + 2\nu)\varepsilon}{\varepsilon} = (1 + 2\nu) \quad (2-9)$$

For semiconductor materials, their resistance is mainly dependent on the piezoresistive effect, which is a change in the electrical resistivity when strain is applied. When a strain is applied, the change in interatomic spacing would alter the bandgap of the material, which changes the excitation energy needed for an electron to travel from the valence to the conduction band. This results in a change in charge carrier concentration, thus affecting the resistivity of the material [42].

Equation 2-10 describes the total resistance change for semiconductors. In this case, the change of resistivity is dominating, while the resistance change due to geometry variation is below 2% of the total [39]. Semiconductors show a wider range of gauge factors than metals, which can be over 100 [43].

$$\frac{\Delta R}{R_0} = \frac{\Delta l}{l_0} + \frac{\Delta A}{A_0} + \frac{\Delta \rho}{\rho_0} \quad (2-10)$$

Besides sensitivity, linearity is also one of the most frequently used parameters to characterize strain sensors. The linearity of a strain sensor is quantified by the coefficient of determination (R^2) obtained from a linear regression of a sensitivity graph [44]. It describes how close the slope of the sensitivity graph is to a straight line. It is desirable for the strain sensors to have a linear response over a large strain range since the nonlinearity adds complexity to the calibration and data processing of the output signal. Metal strain sensors generally have excellent linearity ($R^2 \approx 1$) [45] because their gauge factors only depend on the Poisson's ratio (Equation 2-9). For semiconductors, their linearities are usually lower than metals, because of the different sensing mechanisms. Temperature also poses an effect on the sensor's linearity. Since the resistivity of metals changes proportionally with temperature, and such a proportional relation was not found for semiconductors, it shows a relatively low degree of linearity for semiconductors.

A strain sensor is expected to be reliable, which could provide consistent normal function without degradation. The reliability can be affected by many factors, such as environmental influence including operating temperature, magnetic fields and humidity, and cyclic stability of the sensing material. Temperature is the most common factor influencing sensor performance. The sensitivity to temperature changes is a useful parameter for choosing the most suitable strain sensors based on the environmental conditions and calibration of the output signal. The temperature coefficient of resistance (TCR) describes the change in resistance in parts per million for each degree change in temperature, while the temperature coefficient of gauge factor (TCGF) illustrates the change in sensitivity to temperature [46]. A comparison between the metal foil and semiconductor strain sensor is shown in Table 1. Although semiconductors provide strain sensors with higher sensitivity than metals, their performance is often significantly affected by temperature. Due to its large TCR and TCGF values, semiconductor strain sensors often require recalibration after environmental temperature changes [42]. The cyclic stability of a strain sensor represents the long-term consistency of the electrical response under repetitive loadings, which can be observed by comparing the sensitivity plots after different loading/unloading cycles.

Table 1. Properties of sensors based on metal-foil and silicon. [46]

Strain Gauge Type	Gauge Factor	TCR (ppm/°C)	TCGF (ppm/°C)	Stability
Metal-foil	2-6	20	20-100	Excellent
Silicon	50-200	400-2000	2000	Good

Due to the demand for wearable electronics, the structure of resistive strain sensors has shifted from brittle material to a stretchable format. The development of flexible and robust strain sensors to replace traditional rigid sensors has drawn great research interest due to its wide range of applications. With advancements in flexibility, the strain sensor can be applied to arbitrarily curved surfaces such as the human body to detect a variety of human physiological activities, including large bending movements of hands, arms, and legs, as well as smaller movements of breathing, swallowing, muscle vibrations during vocalization, and blood pressure [47,48]. They can be attached to the clothing or even directly on the human skin for real-time monitoring with minimum discomfort [49]. On the other hand, flexible strain sensors have also shown great

potential in soft robotics as sensory skins, enabling robots to actively interact with the surrounding environment including humans [50].

Flexible strain sensors are typically composed of a layer of active sensing material combined with flexible and stretchable supporting substrates [51]. Generally, the active materials are in the form of conducting micro-/nanomaterials-polymers composites, thin films, or conductive yarn/fabrics. This conductive layer acts as a resistor under an applied voltage. Most flexible substrates are made from polymers, and they are often available in transparent or opaque forms. In addition to a wide range of mechanical properties, they also show good dielectric properties and are relatively cost-effective to produce. There are two main factors for choosing polymer substrates, which are the thermal and chemical robustness. These factors are important because the commonly used microelectronic production processes are based on lithography and chemical etching, which usually involves a heating process, and the use of etchants which limit the selection of suitable substrate materials. The most common flexible insulating backings are made of polyimide (PI) [52], glass-fiber-reinforced epoxy-phenolic [5], or polydimethylsiloxane (PDMS) [53].

For flexible thin film strain gauges, copper-nickel (Cu-Ni) and nickel-chromium (Ni-Cr) alloys are commonly used in recent decades as the sensing layer. The common material composition of Ni-Cr alloy is Ni 80%:Cr 20% and its resistivity is about twice that of the Cu-Ni alloy. This larger resistivity makes the Ni-Cr alloy a suitable material for small volume resistance strain gauges. The properties of the nichrome alloy can be greatly improved by supplementing with small quantities of other metal elements. For this purpose, trace elements, such as aluminum, iron, and copper, have been added into nichrome alloys. Among these, the Ni-Cr-Al-Fe alloy (also known as Karma/Evanohm) is adopted as the main sensitive material for high-precision resistance strain gauges. This alloy is suitable for the production of very small strain gauges for applications requiring a large resistance value, because of its high resistivity of more than 130 Ohm/cm. Another advantage of Karma alloy is its relatively low TCR value (10 ppm/°C) [54].

2.2.2 Conventional fabrication method

Thin film sensing layers are typically deposited using a physical vapor deposition (PVD) technique called sputtering. Another commonly used type of PVD process such as thermal

evaporation is not suitable for alloys such as NiCr, because each component has a different evaporation temperature. Sputter deposition is based on ion bombardment of source material and takes place under vacuum conditions. This process generally uses a magnetron source in which positive ions in a magnetically enhanced glow discharge plasma bombard the target [55]. The high energy bombardment knocks out target atoms that deposit on the substrate surface. The process can be induced in various ways, ranging from direct current (DC) for conductive targets to radio frequency (RF) for nonconductive targets [55]. The properties of the deposited film such as morphology and resistivity are greatly influenced by the deposition parameters chosen during the sputtering process. It was reported that a proper vacuum environment is important in thin film deposition to avoid impurities in the deposited films and achieve the target composition [56].

Pattern generation for deposited films can be achieved in a variety of ways. A simple patterning method is to use a stencil called a shadow mask to selectively deposit materials in a defined area to form a pattern. However, the resolution of this method is limited. To achieve smaller and complex features, photolithography is widely used to pattern thin films. This process could be performed in two ways, etching or liftoff. Both methods involve the application of a photoresist, a photosensitive polymer that either becomes developable in alkaline solutions when exposed to sufficient doses of UV light (positive photoresist) or becomes crosslinked and resistant to development in alkaline solutions (negative photoresist). For an etching process, the film is deposited over the entire substrate, followed by coating a layer of photoresist. Then a UV light is used to selectively expose certain areas of the coated substrate using a photomask. After development in an alkaline solution, the patterned photoresist can be used as the etching mask for the thin film, which can be done by wet chemical etch or dry etch. Finally, the photoresist is removed to reveal the desired pattern. The fabrication process shown in Figure 6 is an example of patterning a thin-film strain gauge using an etching method.

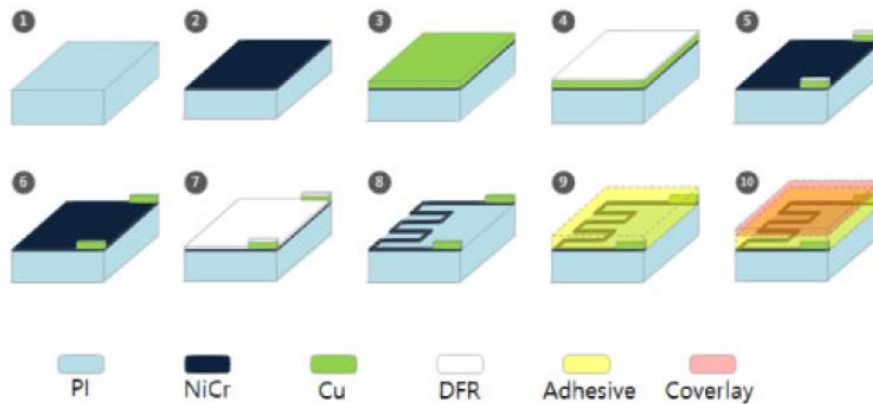


Figure 6. Fabrication process of NiCr strain gauges using lithography method [57].

The liftoff process is slightly different which starts with a layer of photoresist coated on the entire substrate, followed by patterning and developing. Then the film material is deposited over the photoresist coated substrate. The underlying photoresist is then dissolved away, which also removes the film on top of the photoresist and only the patterned thin film is left on the substrate. The advantage of the liftoff process is that it can deposit arbitrary materials without the consideration of etchant chemistry for removal [58]. In this process, the use of photoresist is similar to the shadow mask used for patterning during deposition. Hence, some disadvantages of the liftoff method include a worse attainable resolution during patterning and the inability to deposit films at temperature beyond the decomposition temperature of the photoresist.

Although a lithography-based fabrication process provides high resolution for small feature size, it involves slow developmental cycles, use of toxic chemicals for etching, and requires controlled environments. In addition, this process offers little flexibility in terms of customized designs for small production volumes, due to high fixed costs and long lead times.

2.2.3 Alternative fabrication methods

Other fabrication methods that can alleviate the limitations associated with conventional lithography-based techniques are under investigation, such as additive printing [5], direct-write thermal spray (DWTS) [6] and thin-film patterning by laser ablation [7,8]. Traditional additive printing processes such as screen, and inkjet are utilized for fabricating sensors and electronics, which are more advantageous as compared to conventional lithographic method because of its roll-to-roll (R2R) capabilities, which significantly improves production throughput and thus lowers the

manufacturing cost [59]. Two different assemblies of a screen printer, flatbed and rotary, are commonly used for R2R manufacturing described in Figure 7a&b. The nominal values of common print resolution are between 50 to 100 μm with a wet thickness of a few microns [59]. For inkjet printing (Figure 7c), it provides more flexibility in terms of sensor design but has lower throughput compared to screen printing. Both printing methods offer low pattern resolution in the range of 20-50 μm , due to the spreading of solution on the target substrate. In addition, postprocessing is required to cure the printed ink, which limits the selection of substrates.

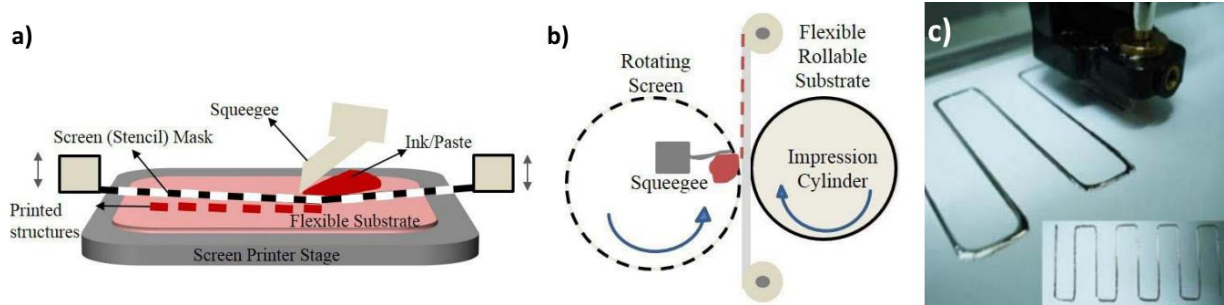


Figure 7. a) Flatbed screen printing with planar substrate; b) Rotary screen printing with moving substrate; c) Inkjet printer. [59]

Thermal spray is commonly used to apply protective coatings on sensors for applications in harsh environments, hence strain sensors fabricated by this technique are expected to be equally reliable [60]. A special feature of this direct-write approach is that the sensor design can be customized on a part-by-part basis simply by adjusting the material deposition toolpath. However, challenges remain in improving accuracy for fabricating small feature size patterns using this method, since the minimum feature size of thermal spray technology is around 100 μm [60].

2.2.4 Thin film patterning by laser ablation

In the last decades, material processing using pulsed laser has been extensively studied for selective patterning of thin films, which is a promising alternative to lithography for microelectronics applications such as strain gauges [8,61], solar cell [62], antenna [63], temperature [64] and pressure sensors [65]. This approach is based on using laser ablation to remove certain areas of the conductive film to achieve functional structures. Ideally, ablation is done selectively to accomplish complete galvanic insulation between separated structures without any damage to the polymer substrates.

The direct laser approach reduces the complexity of the patterning process into a single step, as no postprocessing is required. Consequently, the choice of substrate material can be extended because chemical robustness no longer needs to be considered. Also, the sensor geometry could be directly adopted from a computer model, which offers great flexibility for customized design with a short development cycle.

In addition, conventional and alternative fabrication methods are all limited to a planar surface. Laser patterning has demonstrated the ability to pattern film sensors on 3D-shaped surfaces [66,67], which has the potential for many novel applications of thin film strain sensors, such as direct patterning on drive shafts or complex machine components. The patterning on arbitrary surfaces is achieved by utilizing a dynamic laser beam modulator based on the incidence angle to compensate for the spot size effect and reflectivity changes on a tilted surface. Figure 8 shows an example of the laser patterned strain gauges on a curved surface and both sensors are electrically isolated from the body of the component. The processing time for each strain gauge is less than 20s [67]. A spatial resolution of $30\ \mu\text{m}$ can be patterned on a 3D surface and around $10\ \mu\text{m}$ for a planar surface with a focused laser beam [66].

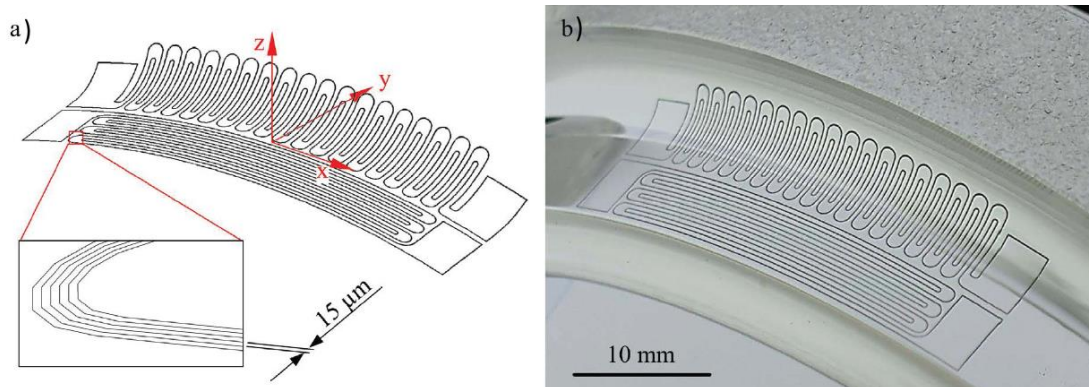


Figure 8. Thin film strain sensors on a complex surface: a) The 3D scanning trajectory visualized in a CAD program and b) results of laser patterning process on a component surface. [67]

Chapter 3 Effect of laser parameters on the ablation process of NiCr films on polyimide

3.1 Introduction

Literature has reported that the quality and dimensional accuracy of laser patterning is not only affected by laser beam characteristics (beam profile, wavelength, fluence), but also by repetition frequency, pulse overlap and many other factors such as substrate material and material properties [68,69]. This makes the optimization of process parameters a challenging process. In this chapter, NiCr thin films on flexible polyimide substrate were used to investigate the relationship between various laser parameters including average power, repetition frequency and scanning speed on the ablation width and depth for flexible thin-film sensors manufacturing. The laser ablation process could be optimized to obtain high-quality thin film sensors that have the potential to offer custom sensor production at a low cost with short lead times.

3.2 Materials and methods

Figure 9 illustrates the UV laser system used for thin film patterning. A diode-pumped solid-state (DPSS) Nd: YVO₄ UV pulsed laser (Samurai Desktop 3500) with a wavelength of 355 nm assembled with a 103 mm f-theta lens was used for the experiment, exhibiting a focused beam diameter of 10 μm. The energy distribution is in TEM₀₀ mode with a beam quality factor of less than 1.25 as declared by the laser manufacturer. The maximum pulse energy and pulse repetition rate of the laser system are 33 uJ and 100 kHz respectively, and the pulse duration varies with the repetition frequency ranging from 20 ns to 80 ns. The studies were conducted in air at room temperature and atmospheric pressure on 5-um thick Evanohm (80%Ni, 20%Cr) films, which were made by hot-pressing on polyimide substrates.

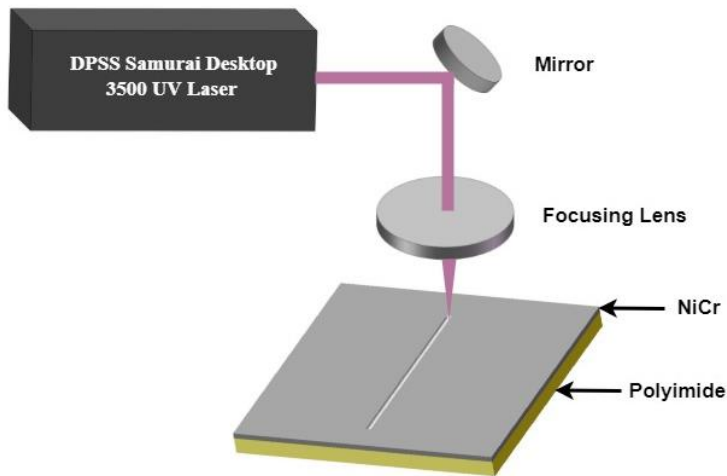


Figure 9. Schematic diagram of the experimental setup.

The detailed laser parameters used in this study to ablate a straight line with a length of 500 μm on NiCr film are summarized in Table 2. The surface morphology of the laser-ablated lines was evaluated using an Olympus BX51M optical microscope and the width of the lines ablated using different parameters was measured in ImageJ by taking an average of 8 measurements at different locations along the ablated lines. For measuring the ablation depth, an optical profiler is the most ideal technique as it does not make direct contact with the sample, however, due to the poor reflectivity at the ablated area, the stylus profiler provides more accurate measurements. Hence, in this study, the depth and the cross-section profile for each line were obtained with a DektakXT stylus surface profiler.

Table 2. Summary of laser parameters used in this study.

Factors	Values
Power (W)	0.2; 0.4; 0.6; 0.7; 0.8; 0.9; 1
Scanning Speed (m/s)	0.1; 0.2; 0.3; 0.4; 0.5
Frequency (MHz)	0.03; 0.05; 0.075; 0.1

To quantify the effect of laser parameters on ablation width, a response surface methodology was implemented for this analysis using Develve software. It is a statistical technique to explore the relationships between several explanatory variables (power, speed and frequency)

and one or more response variables (ablation width and depth). To identify the process parameters that have a significant impact on the measured ablation width, the parameter with the largest p-value was removed, and the remaining p values were re-examined. This process was repeated until only significant ($p < 0.05$) parameters remained.

3.3 Experimental results and discussion

3.3.1 Ablation width

A comparison of the impact of the laser average power, repetition frequency and scanning speed on the ablation width is shown in Figure 10. Each data point represents the average of a range of line widths created at that parameter level. The laser power and repetition frequency were major factors in determining the amount of energy passed onto the thin film, hence, they have a more significant effect on the ablation width. Based on the definition of pulse energy (Equation 2-1), an increase in power boosts the energy per pulse and widens the ablation width (Figure 10a). As mentioned previously, the pulse width varies with repetition frequency; a higher frequency would result in larger pulse width. Hence, according to Equation 2-1 and Equation 2-2, an increase in frequency not only decreases the energy per pulse but also lowers the peak power, resulting in narrower ablation widths. The ablation width could be doubled if the frequency is decreased from 100 kHz to 30 kHz (Figure 10b). The scanning speed has a less pronounced effect, although a slight decrease in width is observed with faster scanning speeds, which can be attributed to less overlap between ablated spots.

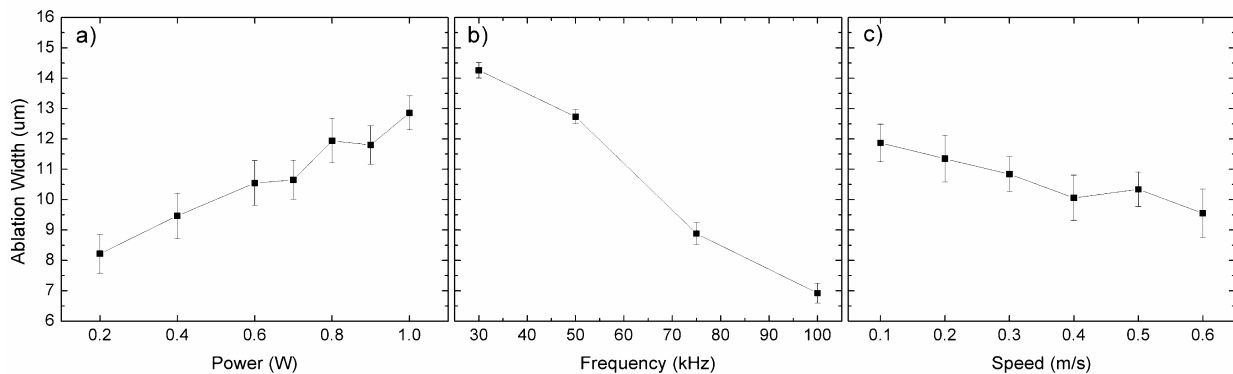


Figure 10. The effect of a) power, b) frequency, and c) scanning speed on ablation width with error bars representing standard errors.

The relationship obtained between laser parameters (average power - P_{avg} , frequency - f , and speed - V) and ablation width (W) using a second-order polynomial model is shown in Table 3 with model statistics shown in Table 4. This model fits the measured ablation width data with a high degree of accuracy, and this is quantified with the high correlation coefficient value for the model ($R^2=0.913$) and the standard deviation between the predicted and actual values (S) is 1.038 μm . Based on the obtained model, the ablation width could be predicted by substituting the process parameters using Equation 3-1. As shown in Figure 11, the actual and predicted values of the ablated width are distributed uniformly along the identity line, which further verifies the accuracy of the model.

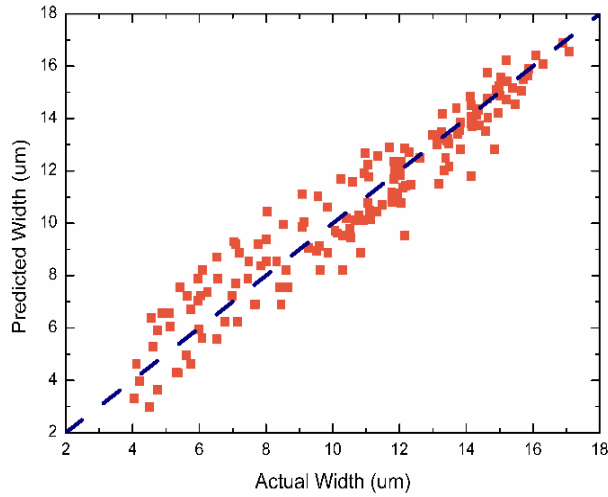


Figure 11. A comparison of actual and predicted ablation width using the response surface model.

A last R^2 method is performed to quantify the effect of each parameter. It is implemented by determining the change in R^2 when excluding each parameter from the model, representing the individual contribution of each parameter to explain the variance of the experimental data [70]. According to the last R^2 value, frequency is found to be the most critical factor on the ablation width, while power has the second greatest influence. These correspond well with the data presented in Figure 10. The negative coefficient for frequency and speed followed the expected relation to the thermal effect during laser ablation.

$$W = 3.71 \times P_{avg} - 128.54 \times f - 3.31 \times V + 28.18 \times P_{avg} \times f + 16.51 \quad (3-1)$$

Table 3. Response surface model results for ablation width.

	Coefficient	Standard Error of Coefficient	T-value	p-value	Last R ²	Model Fit
Constant	16.51	0.594	27.807	< 0.001	-	
Power (W)	3.71	0.813	4.557	< 0.001	0.182	S =
Frequency (MHz)	-128.54	8.248	-15.584	< 0.001	0.704	1.038
Speed (m/s)	-3.31	0.487	-6.801	< 0.001	0.024	R ² =0.913
Power (W) x Frequency (MHz)	28.18	11.793	2.39	0.018	0.03	

Table 4. Statistics for ablation width model in Table 3.

Analysis of variance (ANOVA)	Degrees of freedom (Df)	Sums of squares (SS)	Mean squares (MS)	F-value	p-value
Regression	4	1705.78	426.45	395.98	< 0.001
Error	151	162.62	1.08		
Total	155	1868.4			

3.3.2 Ablation depth

Similar analysis is conducted on the depth of ablated lines measured by a stylus profilometer. Figure 12 summarizes the influence of individual factors on the ablation depth. In general, the effect of these three parameters resembles that of width, but with larger variations. The depth is tripled when the power increases from 0.2 to 1 W. The scanning speed is shown to have a more important influence on the ablation depth compared to width. The depth of the line scanned by 0.6 m/s is only half of that scanned by 0.1 m/s due to the larger distance between adjacent pulses. There is a noticeable transition as the speed increases from 0.3 to 0.4 m/s, because at the speed of 0.4 m/s, the distance between pulses is close to the diameter of the laser beam which means there is no overlap between them. Therefore, the resulting cut is shallower due to single pulse exposure at the irradiated area. The reduction in speed or frequency can expand the overlapped area, resulting in multiple exposures at the same area and greater depth.

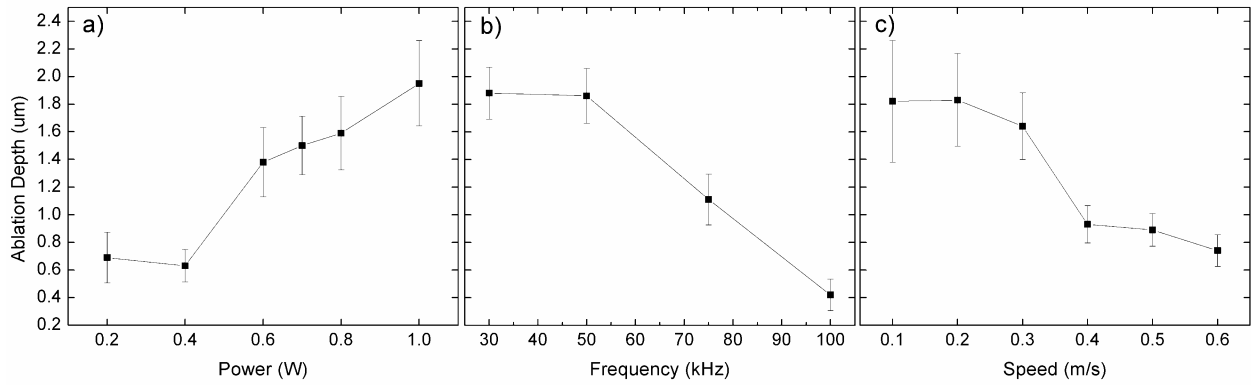


Figure 12. The effect of a) power, b) frequency, and c) scanning speed on ablation depth with error bars representing standard errors.

Equation 3-2 below represents the relationship between the three laser parameters and the ablation depth (D). The details of the model and its statistics are summarized in Table 5 and Table 6 respectively. There are more factors involved when predicting the ablation depth based on the obtained experimental results. It is interesting to note that similar to width, which is significantly affected by the frequency, the frequency squared term has the largest contribution among the factors and the depth is not linearly dependent on frequency in the range studied. Since the ablation depth has an inverse relationship with speed, the coefficient of speed and the product of power and speed terms are negative as expected.

$$D = 4.58 \times P_{avg} - 9.55 \times V - 6.9 \times P_{avg} \times V + 66.25 \times f \times V - 386.18 \times f^2 + 7.92 \times V^2 + 2.66 \quad (3-2)$$

Table 5. Response surface model results for ablation depth.

	Coefficient	Standard error of coefficient	T-value	p-value	Last R ²	Model Fit
Constant	2.66	0.391	6.796	< 0.001	-	
Power (W)	4.58	0.448	10.222	< 0.001	0.158	S =
Speed (m/s)	-9.55	1.828	-5.222	< 0.001	0.159	0.539
Power (W) x Speed (m/s)	-6.9	1.106	-6.236	< 0.001	0.052	R ² =0.79
Frequency (MHz) x Speed (m/s)	66.25	10.769	6.152	< 0.001	0.065	

Frequency (MHz) ²	-386.18	32.981	-11.709	< 0.001	0.345
Speed (m/s) ²	7.92	2.029	3.902	< 0.001	0.011

Table 6. Statistics for ablation depth model in Table 5.

Analysis of variance (ANOVA)	Degrees of freedom (Df)	Sums of squares (SS)	Mean squares (MS)	F-value	p-value
Regression	6	134.97	22.49	77.57	< 0.001
Error	124	35.96	0.29		
Total	130	170.93			

This response model also has a high degree of accuracy for correlating the laser parameters with the ablation depth, which has an R^2 value of 0.79. Due to the shape of the Gaussian beam, the resulted structure generally has a tapered shape and so the ablation depth may not be uniform along the ablated line. Especially for the samples with shallower cuts, a small variation in the measurement location might lead to a value less than the actual maximum depth. Since the model is based on experimental values, under-measured data would cause the model to underpredict the ablation depth at the shallower cut region. Overall, the predicted and measured depth lies closely along the 45° line (Figure 13) and hence further proves the accuracy of the model.

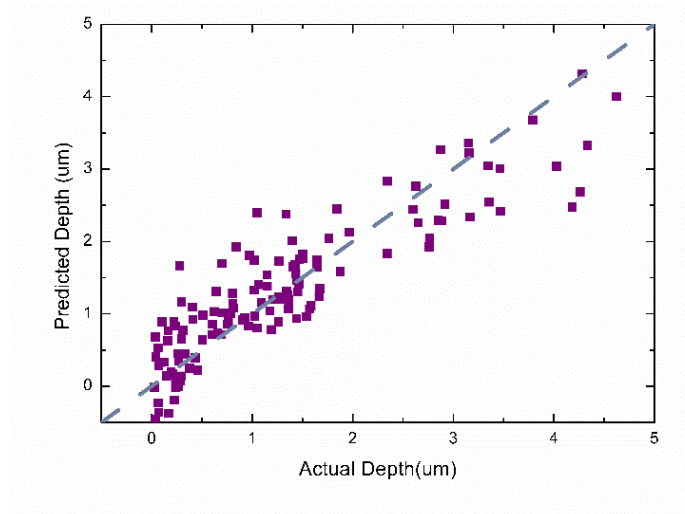


Figure 13. A comparison of actual and predicted ablation depth using the response surface model.

3.3.3 Surface morphology

Although as mentioned previously, the scanning speed has limited influence on the width of the ablated line, it has a more pronounced effect on the edge shape and surface morphology of the resulted geometry due to the difference in pulse overlap factor (ψ). This can be calculated using Equation 3-3 [71],

$$\psi = \frac{v/f}{2 \times w_0} = \frac{Lp}{D_0} \quad (3-3)$$

where v is the scanning speed, f is the frequency, w_0 is the laser beam radius, Lp is the distance between adjacent pulses, D_0 is the diameter of the laser beam. A $\psi = 0$ means the two pulses are completely overlapped and $\psi > 1$ represents no overlap between pulses. Hence, faster speed would lead to a larger overlap factor and so less overlap between two pulses. To reduce edge roughness, pulse overlaps above 90% ($\psi < 0.1$) are commonly used in the literature [72].

The difference in the surface morphology with varying scanning speeds can be observed in the microscopic images as shown in Figure 14. Regardless of applied pulse energy, the cut edge is straighter with a larger overlap factor, since with insufficient overlap, the shape of the laser pulse would contribute to the wavy edge. In addition, the heat generated due to laser irradiation would accumulate in the overlapped region, which leads to more discoloration in the surrounding area. At the speed of 400 mm/s, the distance between two pulses is close to the actual beam diameter, hence the resulted ablation line consists of a row of circles adjoining each other. Above this speed, the overlap factor exceeds 1, hence un-ablated gaps between pulses can be found in Figure 14e & f. At lower pulse energy (Figure 14g-l), the energy input is not high enough to evaporate all melted material, and so the melted material would be pushed outwards by the vapor pressure and solidifies around the border of the circular pulse where the temperature is the lowest, resulting in the formation of channel ridges. This makes the un-ablated area between pulses is less obvious (Figure 14k & l) compared to the resulting channels with lower frequency (Figure 14e & f).

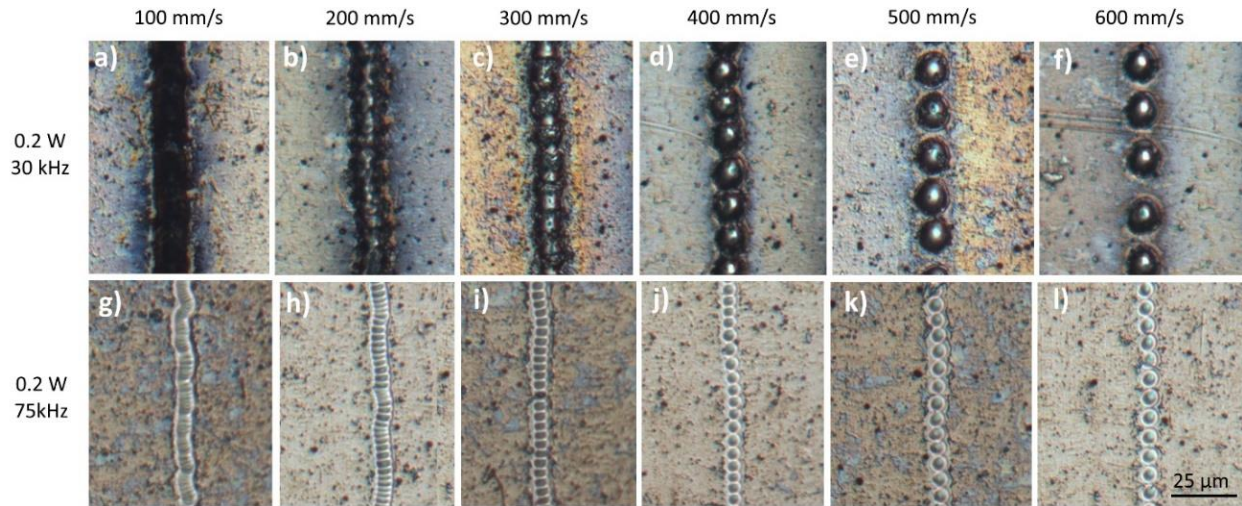


Figure 14. Comparison of surface morphology of the ablated channels by different scanning speeds and different pulse energy. a-f) $6.67 \mu\text{J}$; g-l) $2.67 \mu\text{J}$.

The effect of pulse energy on formed structures is further compared in Figure 15. It was found that the pulse energy also had a significant effect on the geometry of ablated microchannels. With the constant average power, increasing frequency has the same impact as decreasing scanning speed, which results in a smaller overlap factor (Equation 3-3). It is noticeable that among these four different repetition rates, the channel made at 30 kHz have the largest width and depth for all power levels. In addition, more discoloration is observed at lower frequencies, especially at a high input power of 1 W (Figure 15a & e). According to the equation of pulse energy (Equation 2-1), with lower frequency, each pulse contains more energy and so more heat is generated on the target surface after laser irradiation, leading to a larger heat-affected zone.

The average power has an intuitive influence on the ablated channels, as the larger emission energy intensifies the material removal process. At an average power of 1 W, the irradiation energy is sufficient to ablate through the film. As the energy reduces to 0.8 W, due to smaller energy distribution at the pulse edge, there are residual strings left in the channel (Figure 15i & j), which is not ideal for applications that require complete galvanic insulation between separated structures. As the energy is further reduced (0.6 W), the input power is only sufficient to ablate through the material at the center of the pulse where the energy is the maximum, and unable to remove all the irradiated material at 0.4 W.

For some of the ablated channels such as in Figure 15m & n, an inconsistency in depth is observed, which may be attributed to the imperfection of laser power stability. Among all the parameter sets, the combination of 1 W, 75 kHz and 100 mm/s produces the cleanest and straightest channel with minimal discoloration.

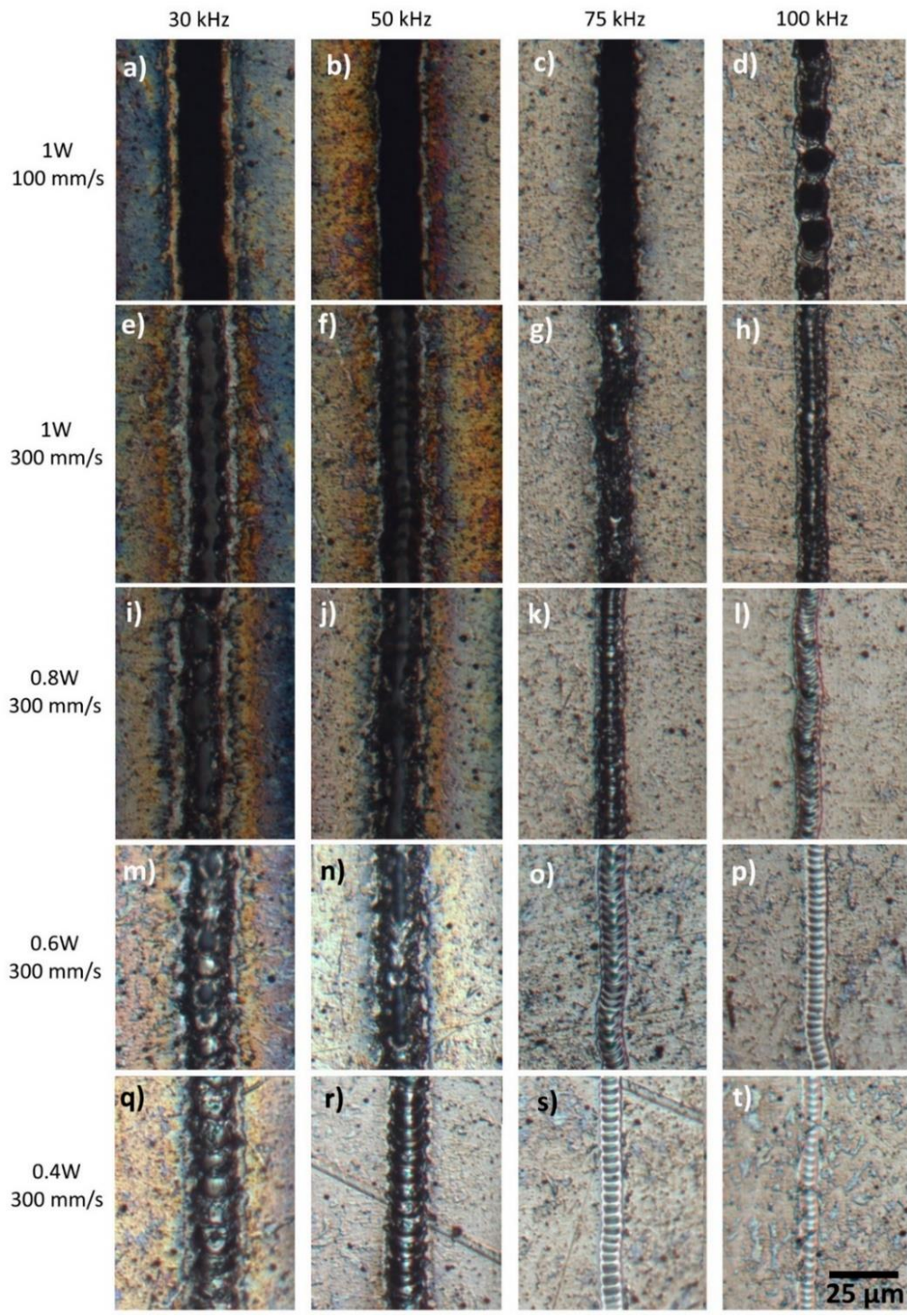


Figure 15. Microscopic images of laser ablated channels with various average power, frequency, and scanning speed.

3.3.4 Cross-section profile

Figure 16 shows representative two-dimensional cross-section profiles of ablated channels made at different scanning speeds and constant pulse energy of $9.33 \mu\text{J}$. It can be observed from the profile image that the microchannels are ablated by the Gaussian beam and the round shape of the crater in Figure 14 confirms the good beam quality. Although there is no remarkable difference in ablation width due to varying speed as shown in Figure 14, the ablation depth is greatly affected by the speed. An increase in speed from 100 to 600 mm/s only resulted in a width reduction by around 15% (from $12.65 \mu\text{m}$ to $10.59 \mu\text{m}$ with a pulse energy of $6.67 \mu\text{J}$), whereas the depth decreased by 75% from 3705.8 nm to 558.2 nm . This could be explained by the faster heat loss at the surface and more energy accumulation in the vertical direction.

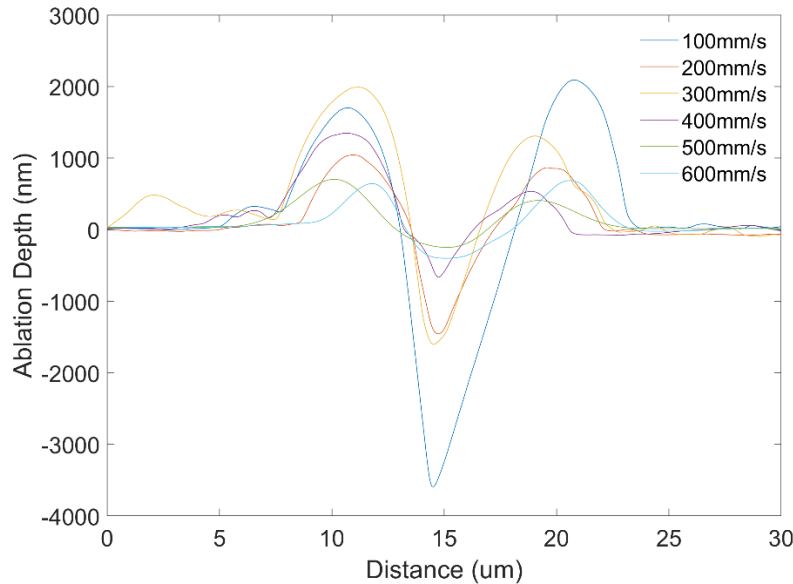


Figure 16. Comparison of the ablated channels' cross-section profile with pulse energy of $9.33 \mu\text{J}$ and different scanning speeds.

There are channel ridges formed on both sides of the microchannels. It was proposed by various researchers that for high laser energy density ($\sim 100 \text{ J/cm}^2$), the resulting recoil pressure due to the formed vapor above the sample surface would be extremely high, which induces a shock wave and generates a hydrodynamic melt motion on the liquid melt pool [73,74]. As a result, the liquid metal is ejected out from the laser-material interaction region and its temperature drops dramatically. When the surface temperature drops below vaporization temperature, the recoil pressure no longer influences the molten material. At the end of a laser pulse, the surface tension

and gravity drive the liquid metal back to its original position [75]. Due to the self-quenching effect and fast cooling rate, the liquid material instantly solidifies and forms a liquid pile around the laser-material interaction zone. Thus, it can be observed from Figure 16 that at slower speeds, as more vaporization and melting occur, the resulting ridges are larger.

3.4 Summary

The average laser power, repetition frequency, and scanning speed are found to be significant parameters of laser patterning process in controlling the quality and dimensional accuracy of ablated microchannels. The size of the microchannels is strongly dependent on laser pulse energy and pulse overlap. High pulse overlaps are desired to fabricate good-quality channels.

These parametric results can be used to develop process maps that allow for the selection of parameters based on required feature sizes in thin film sensors. In practical use, a lower bound to the operating space is set by selecting parameters with sufficient overlap between adjacent pulses, while parameters that form large heat-affected zones provide an upper bound.

Chapter 4 Theoretical analysis of pulsed laser ablation process

4.1 Introduction

A clear theoretical understanding of the impact of the process parameters on the material removal rate can improve the efficiency of laser energy utilization and enhance the ablation rate. In this chapter, two approaches are implemented for further investigation of process optimization. An analytical method is used to find an empirical threshold fluence based on the experimental results discussed in Ch. 3, which can be used to predict the dimensions of the ablated channel by various processing parameter sets. In addition, a finite element model is designed using COMSOL Multiphysics to simulate the geometry ablated by a moving laser source and establish a guideline for selecting processing parameters based on the desired dimensions.

4.2 Analytical method

Process optimization for laser patterning is a challenging process because of the various factors involved in the process. The trial-and-error method of optimization is often time-consuming and not applicable to diverse sensor designs with different film thickness. Hence, an analytical method is utilized to describe the behavior of pulsed laser ablation process of NiCr films to assist the development of optimized process parameters to achieve required functional structures without damage to the underlying substrate material.

4.2.1 Theory

The Bouguer-Lambert-Beer absorption law, also known as Beer's law, is an essential component of many laser ablation models. It relates the attenuation of light to the properties of the material which the light is traveling through:

$$I_t = I_0 10^{-\alpha l} \quad (4-1)$$

where I_t and I_0 are the intensities of the light beam before and after transmission through a layer of material with thickness l , and α is the absorptivity of the material at the given wavelength [76]. If one assumes that laser ablation is a two-step process, which includes initial energy absorption followed by material ablation, then Beer's law can be utilized to calculate the ablation depth of a single laser pulse:

$$F_x = F_{inc} e^{-\alpha x} \quad (4-2)$$

where F_x is the attenuated laser fluence at depth x into the material and F_{inc} is the incident pulse fluence [77]. Since the laser ablation phenomenon generally occurs when the energy absorbed by the target reaches a threshold value (F_{th}), F_x needs to be equal to F_{th} . When this is true, the incident fluence must be increased over the threshold fluence by a factor of $e^{\alpha x}$ so that ablation occurs at the desired depth x . The factor $e^{\alpha x}$ compensates for the exponentially decreasing energy density as the beam penetrates the material.

$$F_{th} = F_{inc} e^{-\alpha x} \quad (4-2-1)$$

$$F_{inc} = F_{th} e^{\alpha x} \quad (4-2-2)$$

By rearranging Equation 4-2-2, the formula for single pulse ablation depth (L_f) can be obtained (Equation 4-3). This expression has been utilized in one form or another in many studies [76–78].

$$L_f = \frac{1}{\alpha} \ln \left(\frac{F_{inc}}{F_{th}} \right) \quad (4-3)$$

On the other hand, for a laser source with a Gaussian beam profile, the spatial and temporal distribution follows the equation below, when neglecting beam diffraction:

$$I(r, t) = I_p \exp\left(\frac{-2r^2}{\rho^2}\right) \exp\left(\frac{-t^2}{\tau^2}\right) \quad (4-4)$$

where I_p is the peak intensity, ρ and τ are the spatial and temporal radius at the 1/e intensity contour, r is the radial coordinate of distance from the propagation axis and t is the time variable [79]. According to the definition of the laser beam, ρ is also the theoretical beam radius (ω) of the focused laser source. Then the spatial distribution of the energy fluence is given by:

$$F(r) = \int_{-\infty}^{\infty} dt I(r, t) = \sqrt{\pi}\tau I_p \exp\left(\frac{-2r^2}{\omega^2}\right) = F_0 \exp\left(\frac{-2r^2}{\omega^2}\right) \quad (4-5)$$

where F_0 is the peak fluence at the center of the beam and is equal to $\sqrt{\pi}\tau I_p$. Based on the method proposed by Liu [79], which defines the ablation threshold fluence (F_{th}) as the local fluence

corresponding to the rim of the ablated crater with a radius equal to R , Equation 4-5 can be rewritten as follows,

$$F_0 = F_{th} \exp\left(\frac{2R^2}{\omega^2}\right) \quad (4-6)$$

By taking its logarithm, this expression can be transformed into a linear relationship between the ablation threshold fluence and the diameter (D) of an ablated crater as expressed by Equation 4-7. The diameter of the ablated geometry is equal to the diameter of the Gaussian beam at the threshold fluence as shown in Figure 17. This method is particularly simple and advantageous as it does not require full knowledge of laser beam characterization and can be used to estimate the laser spot size on the target surface regardless of the specific optical arrangement.

$$D^2 = 4R^2 = 2\omega^2 \ln\left(\frac{F_0}{F_{th}}\right) \quad (4-7)$$

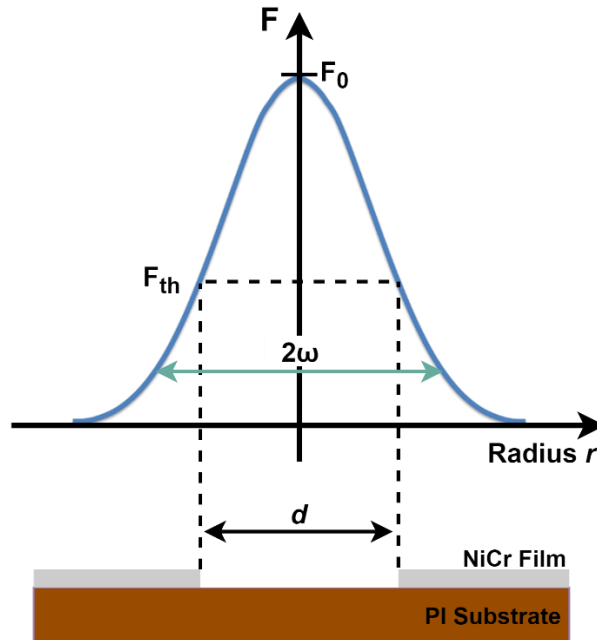


Figure 17. A circular Gaussian beam profile creates an ablated spot with a diameter of d if an ablation threshold $F_{th} < F_0$ exists.

Hence, the empirical ablation threshold fluence can be estimated, which can be utilized for predicting the depth and width of the ablated crater with selected process parameters.

4.2.2 Effect of laser fluence

The general definition of the fluence of a laser pulse is the optical energy delivered per unit area. There are various approaches to evaluating fluence. According to the Equation 4-3 and Equation 4-7, the fluence is a critical factor in determining the threshold fluence for laser ablation. In the following section, experimental results of ablation width and depth are evaluated using several different fluence definitions.

The most commonly used method for calculating fluence is using the total energy of a single laser pulse, which is equal to the product of the pulse's peak power and pulse duration (τ) or the average power and pulse period ($1/f$), divided by the effective focal spot area,

$$F = \frac{P_{peak} \times \tau}{\pi\omega^2} = \frac{P_{avg}/f}{\pi\omega^2} \quad (4-8)$$

Using this definition, the ablation depth and width obtained experimentally are plotted in Figure 18 against the corresponding fluence in the base e scale. Each dataset is divided into four groups based on the repetition frequency. Generally, higher laser fluences produce the expected wider and deeper craters. According to Equation 4-3 and Equation 4-7, both relationships between the depth versus fluence and width versus fluence are expected to be linear on the semi-log plot. However, for the depth plot, there is a large variation in the high fluence region, and no clear linear trend can be observed. In addition, in both plots, each fluence value has multiple corresponding depth and width values. This is because this definition of laser fluence does not consider the effect of scanning speed, it only varies with the average input power and repetition frequency. In the experiment, a continuous line is ablated instead of a single spot exposure on the NiCr surface. Hence, the definition of the fluence needs to be adjusted to incorporate the scanning speed.

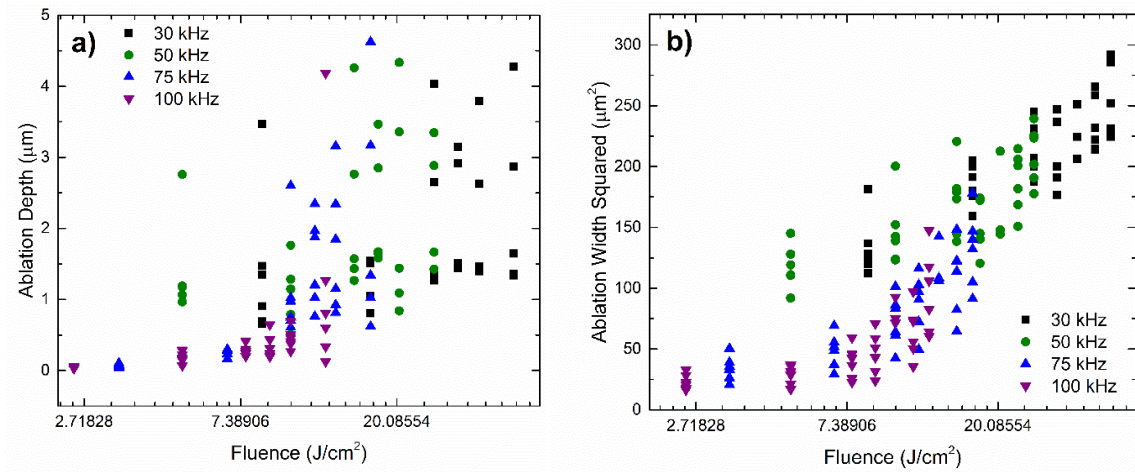


Figure 18. a) Ablation depth and b) ablation width squared versus the laser fluence calculated from Equation 4-8 with different frequencies.

To add the impact of scanning speed into the definition of fluence, the area covered by the laser beam is reconsidered. In the previous equation (Equation 4-8), the laser beam is assumed to only irradiate on a circular area that is equal to the size of the laser beam. However, the actual area that the laser beam travels during a cycle is larger than the size of the beam, since a portion of the distance traveled is spent in the off state. As illustrated in Figure 19, the total area exposed by one laser pulse is the sum of half the beam area and a rectangular region which depends on the scanning speed and frequency. Hence, the definition of fluence is adjusted as shown below,

$$F = \frac{P_{avg}/f}{\frac{\pi\omega^2}{2} + \frac{2\omega V}{f}} \quad (4-9)$$

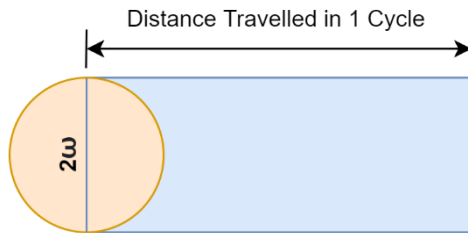


Figure 19. Illustration of area exposed by the laser in one cycle.

With the adjusted fluence definition, the depth and width are replotted as shown in Figure 20. The trend is more apparent in both plots compared to the previous ones (Figure 18). However,

the data points are separated by frequency in both depth and width plots, hence, the frequency is not sufficiently considered in this fluence definition. Further improvement on the fluence equation is needed to incorporate the effect of all the processing parameters.

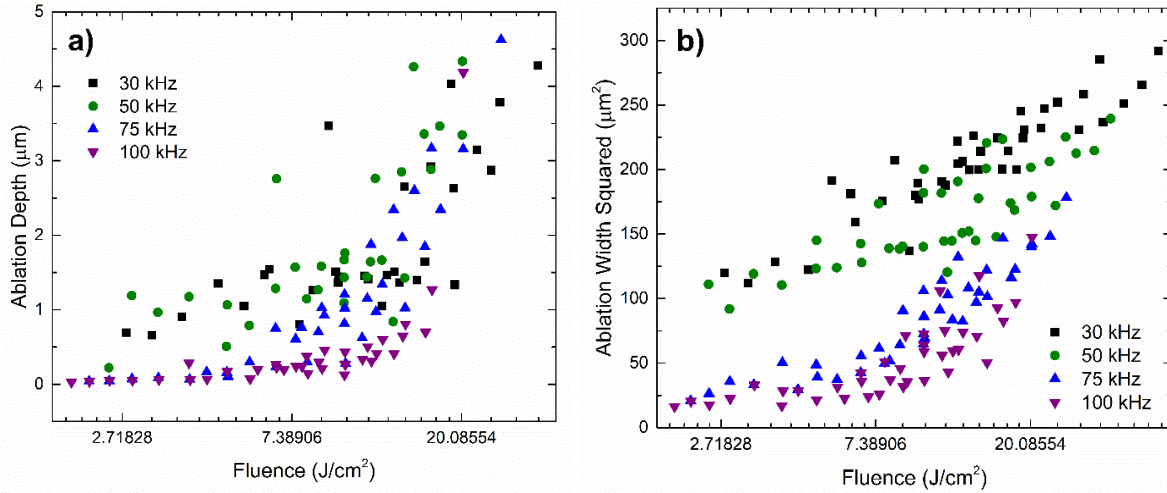


Figure 20. a) Ablation depth and b) ablation width squared versus the fluence calculated from Equation 4-9 with different frequency.

Since the depth and width are measured from the ablated channels, it is necessary to consider multiple pulses in the fluence definition. Assuming there is a finite number of pulses (n), the total energy would become n times the pulse energy and the total covered area is the sum of the semicircle and n numbers of rectangles (Figure 21). As the n approaches infinity, the area of the semicircle would be negligible and so the n and f terms in the numerator and denominator can be canceled out. Hence, the equation can be simplified as shown below.

$$F = \lim_{n \rightarrow \infty} \frac{n \left(\frac{P_{avg}}{f} \right)}{\frac{\pi \omega^2}{2} + n \left(\frac{2\omega V}{f} \right)} = \frac{P_{avg}}{2\omega V} \quad (4-10)$$

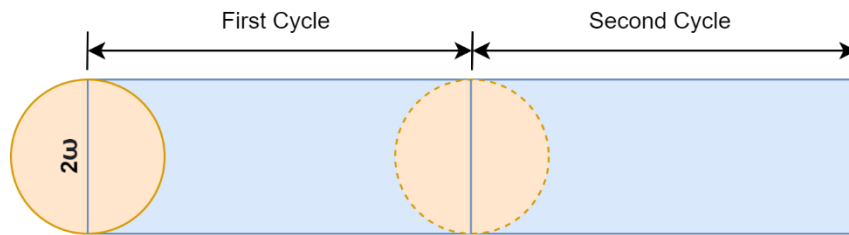


Figure 21. Illustration of area exposed by multiple laser pulses.

In addition, since the laser source used in the experiment of Ch. 3 is a ns laser, as a result, the area of the actual exposed surface is much smaller than the area that the laser travels in one cycle. To improve the accuracy of the model, a new factor, duty cycle, should be included, which is the ratio of pulse duration and pulse period. It represents the fraction of time in which the laser is on. In this definition, the actual area irradiated by the laser is equal to the product of the duty cycle and the total area traveled by the laser. Equation 4-12 represents the final equation proposed for finding the empirical threshold fluence.

$$Duty\ Cycle = \frac{\tau}{1/f} = \tau f \quad (4-11)$$

$$F = \frac{P_{avg}}{2\omega V \times \tau f} \quad (4-12)$$

Figure 22 shows the ablation depth and width versus the fluence calculated by the final equation that takes into account the actual exposed area and shows best-fit lines calculated using Equation 4-3 and Equation 4-7 respectively. The best-fit parameters for the linear relationships, as well as the R^2 and normalized root-mean-square error values are summarized in Table 7 for the depth model and Table 8 for the width model. With the further developed fluence equation, the relationship between fluence and the size of the ablated channel is more clearly shown in the plots.

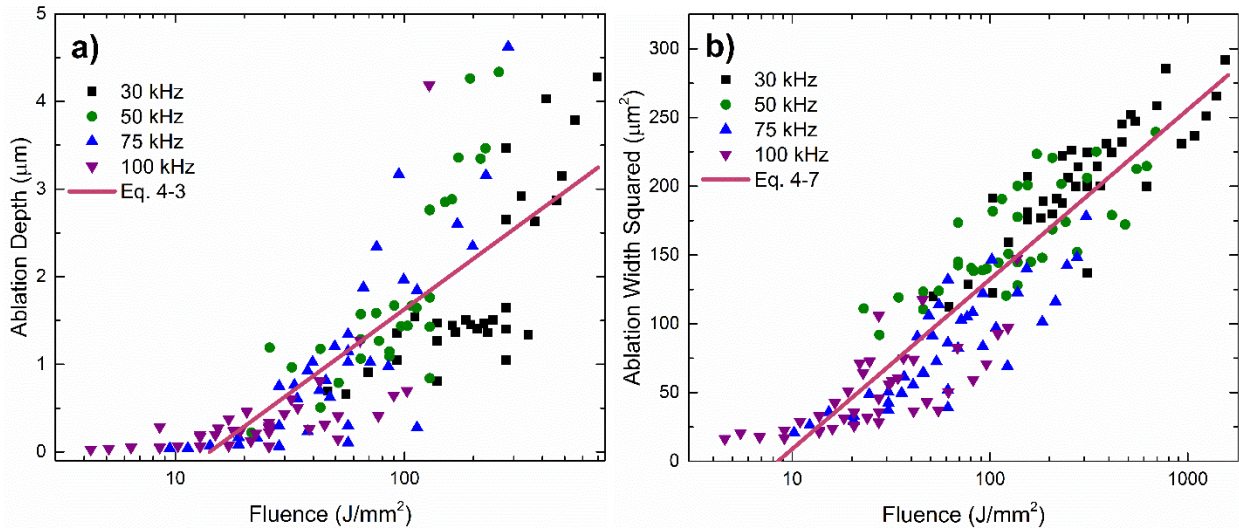


Figure 22. a) Ablation depth and b) ablation width squared versus the fluence calculated from Equation 4-12 with different frequencies.

The obtained threshold fluence using experimental depth values is close to that from width values. The difference between the threshold fluence might be caused by measurement error due to difficulties measuring nonuniform channel depths in cases where there is low pulse overlap, which leads to a smaller measured value than the actual depth. Hence, the empirical threshold fluence is slightly larger when calculated using experimental depth values and is likely more accurate when calculated using the experimental width values. This also explains the higher R^2 value for the model when using the width data. The calculated beam radius by fitting Equation 4-7 to the experimental width (5.18 μm) is almost identical to the value declared by the laser manufacturer when the beam is properly focused (5 μm), supporting the validity of the model.

Table 7. Fit parameters for laser fluence and ablation depth relationship.

Fit Parameters			Model Summary	
Form	α (μm^{-1})	F_{th} (J/mm^2)	R^2	NRMSE
Equation 4-3	1.203	14.108	0.62	0.1542

Table 8. Fit parameters for laser fluence and ablation width relationship.

Fit Parameters			Model Summary	
Form	ω (μm)	F_{th} (J/mm^2)	R^2	NRMSE
Equation 4-7	5.176	8.466	0.82	0.1108

4.2.3 Effect of pulse overlap

Literature on laser studies has reported that many materials show an incubation effect, i.e. the threshold fluence also depends on the number of pulses applied [80,81]. In general, the threshold fluence decreases when the number of pulses is increased. The decrease of the threshold fluence for multi-pulse irradiation is attributed to the accumulation of laser-induced chemical and/or structural changes in the material [82]. The physical mechanism of incubation is still controversial. One most likely hypothesis is that after multi-pulse irradiation, the surface roughness would increase due to ripple formation and accumulation of surface defects, which enhance the absorption of the next coming laser pulses and so increase the material removal rate [80]. This phenomenon could be expressed in the incubation model proposed by Jee et al. [81]

$$F_{th}(N) = F_{th}(1) N^{S-1} \quad (4-13)$$

Equation 4-13 relates the multi-pulse threshold fluence, $F_{th}(N)$, to the single pulse ablation threshold, $F_{th}(1)$, by introducing the so-called incubation coefficient S in a power law. However, this incubation model is only developed for stationary laser ablation, as all the pulses are irradiated at the same location. In this study, a moving laser source is used, which results in an ablated channel rather than a single crater. Hence, instead of studying the effect of the number of pulses on the threshold fluence, the influence of pulse overlap is analyzed. The depth and width datasets are classified into three groups, overlap distance larger than pulse radius ($\psi < 0.5$), overlap less than half of pulse size ($0.5 < \psi < 1$) and no overlap ($\psi > 1$), with some examples of pulse overlap and the corresponding numerical value shown in Figure 23.

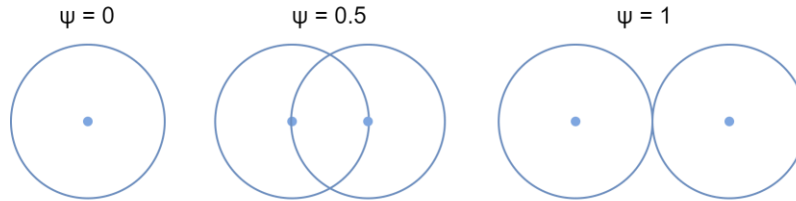


Figure 23. Illustration of different pulse overlap conditions.

Figure 24 presents the experimental depth and squared width values versus fluence with the best-fit lines calculated using Equation 4-3 and Equation 4-7 respectively. The fluence values when the depth and width values are zero is corresponding to the threshold values and are summarized in Table 9.

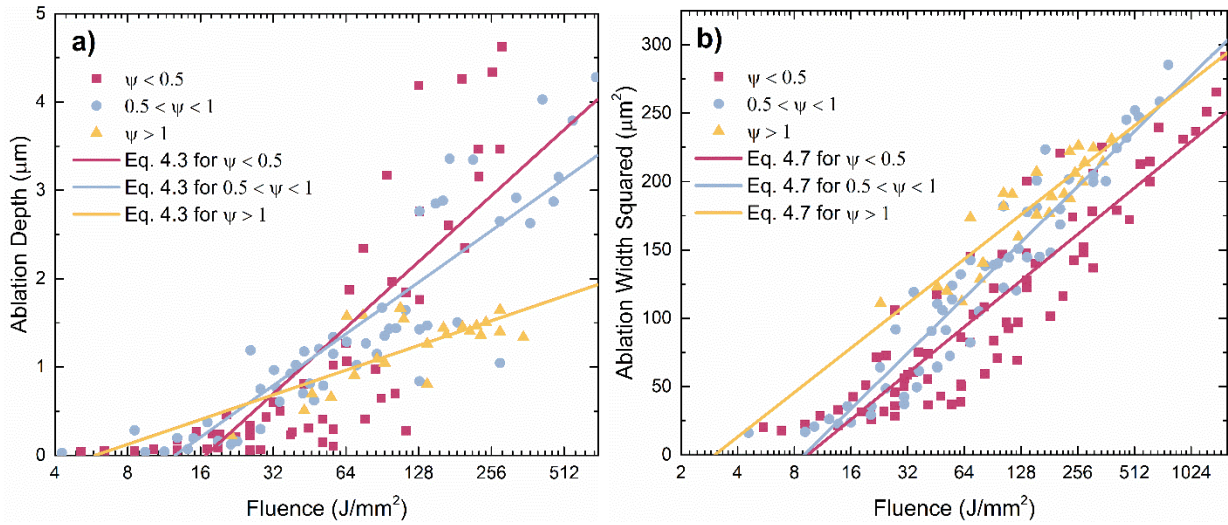


Figure 24. a) Ablation depth and b) ablation width squared versus the fluence calculated from Equation 4-12 with different pulse overlap conditions.

Table 9. Comparison of the empirical threshold fluences for different pulse overlap conditions.

Overlap	$\psi < 0.5$	$0.5 < \psi < 1$	$\psi > 1$
F_{th} - Depth	16.771	12.5377	5.8607
F_{th} - Width	9.408	8.9705	3.0167

It was found that the pulse overlap factor has an opposite effect compared to the number of pulses; as the overlap between pulses gets smaller, the threshold fluence decreases. For both depth and width, the threshold value is tripled changing from no overlap to more than half overlap. This could be attributed to the formed cluster consisting of particle and/or plasma and/or vapor shielding the target surface after the first pulse irradiation, which scatters and absorbs a portion of the laser energy of the subsequent pulses. It was reported by Niso et al. that when ablating stainless steel in a frequency range from 50 kHz to 400 kHz, an increase of the ablation threshold is observed for both pulse duration of 650 fs and 10 ps, which can be ascribed to shading effects [83]. However, for repetition rates higher than 400 kHz, a decrease in the ablation threshold is found, which is attributed to the heating of the sample by heat accumulation that could overbalances particle shielding at higher repetition rates. In this case, the effect of heat accumulation at high frequency is similar to the multi-pulse irradiation, both of them reduce the ablation threshold.

In addition, Ancona et al. presented a comparison study on the number of pulses required to ablate through stainless steel and copper as a function of frequency at high pulse energy (30 μJ - 70 μJ) [84]. It was found that for stainless steel, an increase in the number of pulses is observed when the frequency increases from 50 to 400 kHz for pulse energies of 30 μJ , and a decrease is observed at an even higher frequency [84]. This is the same as the trend reported by Niso et al. [83] for stainless steel. However, for copper, the number of pulses to drill through is close to constant, which is independent of the repetition frequency [84]. In this case, the particle shielding and heat accumulation both have a negligible influence on the ablation efficiency of copper. This is likely due to the high thermal conductivity and thermal diffusivity of copper, preventing the heat accumulation effect interfere with the process at high frequency. Also, since the heat could be dissipated quickly in copper, the formation of a superheated layer could be reduced. As a result, the emission of particles originating from the superheated layer due to phase explosion caused by homogeneous nucleation could also be reduced [85]. Because NiCr has a thermal conductivity close to stainless steel [86] and the experimental values are obtained with a repetition frequency of 30 to 100 kHz, the particle shielding is expected to have an effect on the ablation rate, leading to an increase in threshold fluence similar to the steel.

On the other hand, as mentioned in Ch. 3.3.3, after laser irradiation, there is molten material solidified and built up at the rim of the ablated spot. As a result, when pulses overlap, the second and subsequent pulses need to remove not only the material under the surface but also those ridges formed after the previous pulse. Therefore, more energy input is required to achieve the same depth or width at larger overlaps.

To further quantify the effect of pulse overlap on threshold fluence, an formula similar to the incubation model is proposed to relate the threshold values, $F_{th}(V)$, with scanning speed (V) through a base fluence F_0 . Figure 25 presents the scanning speed versus threshold fluence with the fit of Equation 4-14. The fit parameters for the relationship following a power function are shown in Table 10. The obtained F_0 value from depth and width measurements are similar, as well as the S values, hence the same relationship is valid for both width and depth.

$$F_{th}(V) = F_0 V^S \quad (4-14)$$

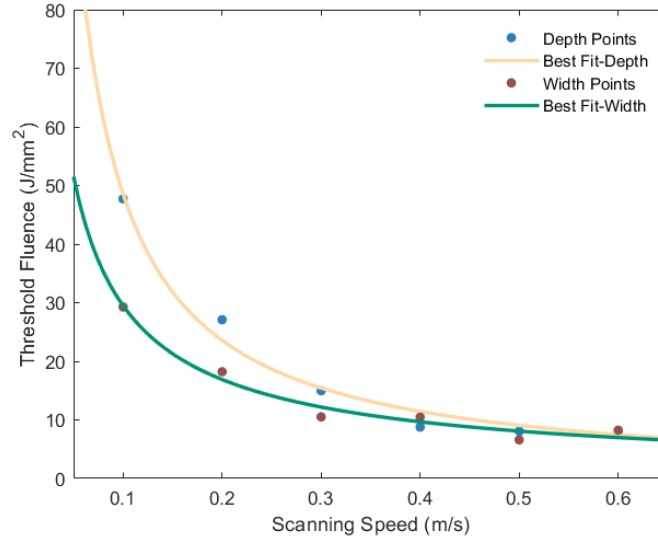


Figure 25. Threshold fluence as a function of scanning speed for experimentally obtained depth and width.

Table 10. Fit parameters for threshold laser fluence and scanning speed relationship.

Fit Parameters			Model Summary	
Form	F_0	S	R^2	NRMSE
Depth	4.3985	-1.0429	0.9826	0.0587
Width	4.6289	-0.8042	0.9751	0.0663

4.3 Finite element simulations

Due to the extremely fast dynamic laser-material interaction process, it is usually hard to make in-situ observations during the laser ablation experiments. Therefore, finite element analysis is implemented to better comprehend the physical phenomenon of the interaction process between the UV pulsed laser and NiCr film and provide insight into the interpretation of experimental results presented in Ch. 3.

4.3.1 Governing equations

During the laser ablation process, the material undergoes a phase change (solid to liquid to vapor or directly from solid to vapor) as temperature rises. In addition, the heat (latent heat of fusion and evaporation or latent heat of sublimation) consumed or released during the phase change significantly affects the surface temperature and melt pool size. Therefore, the temperature-

dependent material properties of NiCr, such as density, thermal conductivity and specific heat are incorporated into the computational model to improve the accuracy.

The heat transfer model solves for Equation 4-15 derived from the principle of conservation of energy, which represents that the variation of internal energy in time is balanced by convection of internal energy, thermal conduction, radiation, dissipation of mechanical stress and additional heat source [87].

$$\rho C_p \left(\frac{\partial T}{\partial t} + u_{trans} \cdot \nabla T \right) + \nabla \cdot (q + q_r) = -\alpha T \frac{dS}{dt} + Q \quad (4-15)$$

where ρ is the density, C_p is the specific heat capacity, T is the absolute temperature, u_{trans} is the velocity vector of translational motion, q is the heat flux by conduction (Equation 4-16), q_r is the heat flux by radiation (Equation 4-17), α is the coefficient of thermal expansion, S is the second Piola-Kirchhoff stress tensor and Q is the additional heat source.

$$q = -k \nabla T \quad (4-16)$$

$$q_r = \varepsilon \sigma (T_{amb}^4 - T^4) \quad (4-17)$$

In the case of laser ablation, thermoelectric effects in the solid are not considered. Therefore, the first term on the right-hand side of Equation 4-15 can be neglected. The only additional heat source comes from laser irradiation. The average laser power density in Gaussian distribution can be expressed by Equation 4-18 [75].

$$P_g = A \left[\frac{E_p}{P_w \left(\frac{\pi}{4} D^2 \right)} \right] \exp \left[-\frac{(x - x_r)^2}{2\phi^2} \right] \quad (4-18)$$

where A is the absorptivity, E_p is the pulse energy, P_w is the pulse width, D is the laser beam diameter, x_r is the reference point to represent the center of the laser beam, and ϕ is the standard deviation of the Gaussian laser beam. In order to incorporate the effect of scanning speed (V) and multi-pulse irradiation on the resulted geometry, a moving laser source is implemented instead of a stationary heat source. Hence, here the reference point of the laser beam center is defined as,

$$x_r = x_0 + V t \quad (4-19)$$

Since the heat source is a pulsed laser, during the application of a single pulse, the laser is on for a specific time equal to the pulse width followed by cooling until the end of a pulse. To simulate this, an analytic function (β , Equation 4-20) is used, which includes a rectangular function to set the laser turn-on time (lower and higher limits of 0 and P_w s, respectively) and a mod function to control the repetition period (frequency, f), that returns the total number of pulses in time t ,

$$\beta = \text{rect}\left(\text{mod}\left(t, \frac{1}{f}\right)\right) \quad (4-20)$$

4.3.2 Finite element model setup

A two-dimensional and time-dependent computational model, which incorporates heat transfer and deformed geometry is developed. The model is used to analyze the temperature variation in the NiCr film over time, while also including the heat of sublimation and the resultant material removal rate, and the final geometry of the ablated structure when the surface is subjected to various laser machining conditions. The initial geometry used in the heat transfer model is presented in Figure 26.

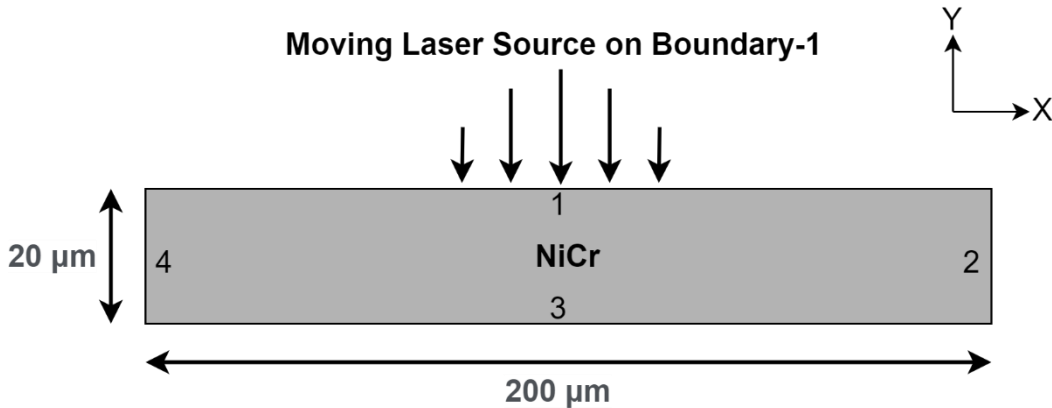


Figure 26. Two-dimensional geometry for the computational model.

Several assumptions are made in this model. First, to simplify the computation, only those materials that go directly to the gas phase are considered. In this case, it can be assumed that the material is being heated in such a way that its surface reaches its maximum temperature and that there is no internal heating that may result in a gas-filled interior of the solid. Hence, the sublimation should occur at the material's top surface. In addition, an assumption is made that the material is no longer thermally significant and does not interact with the laser source once it

transitions to the gas phase because the laser system is equipped with a ventilation system and the surrounding gas flow carries the vaporized material away.

Table 11 summarizes the material properties of NiCr and the laser processing parameters used in the model. Since the thermal properties of NiCr have not been well studied in the literature, the properties of Ni are used instead for approximation. The governing equation and various boundary conditions employed in this model are also summarized in Table 12. One important boundary condition is that the temperature in the solid material cannot exceed the vaporization temperature, because when the material is at its vaporization temperature, its state changes to gas and is removed from the modeling domain. This rate of mass loss from the irradiated surface is governed by the material density and the heat of sublimation (Equation 5 in Table 12). To incorporate this limit, ablative heat flux is introduced to the model as represented by Equation 6 in Table 12, where q_a is the heat flux due to material ablation, T_v is the vaporization temperature, and $h_a = h_a(T)$ is a temperature-dependent heat transfer coefficient that is zero for $T < T_v$ and increases linearly as $T > T_v$. The slope of the curve of h_a could be arbitrary but it needs to be very steep to enforce the temperature of the solid material cannot markedly exceed the vaporization temperature.

The Deformed Geometry interface in COMSOL is used to model the material removal. A prescribed zero displacement is set at the bottom surface of the material to enforce no deformation and a normal mesh velocity defined by Equation 5 in Table 12 is set at the top surface to apply the material removal rate.

Table 11. Material properties of NiCr and laser processing parameters.

Property	Nomenclature	Value (units)	References
Latent of sublimation	H_s	7.06 (kJ/g)	[88]
Ambient temperature	T_{amb}	293.15 (K)	-
Heat transfer coefficient	h	10 (W/ (m ² K))	[89]
Density	ρ	8300 (kg/m ³)	[86]
Vaporization temperature	T_v	3186.15 (K)	[90]
Emissivity	ε	0.88	[86]

Stefan–Boltzmann constant	σ	5.67×10^{-8} (W/m ² K ⁴)	[87]
Absorptivity	A	0.6	[91]
Beam diameter	D	10 (μm)	-
Standard deviation of the Gaussian laser beam	ϕ	2.3 (μm)	-
Average Power	P_{avg}	0.2, 0.4, 0.6, 0.7, 0.8 (W)	-
Frequency	f	30, 50, 75, 100 (kHz)	-
Pulse duration	P_w	24, 31, 47, 78 (ns)	-
Scanning speed	V	0.1, 0.2, 0.3, 0.4, 0.5 (m/s)	-
Laser start position	x_0	20 (μm)	-

Table 12. Boundary conditions of the heat transfer model.

No.	Boundary condition	Equation	Boundary number
1	Governing equation	$\rho C_p \left(\frac{\partial T}{\partial t} \right) = k \left[\frac{\partial^2 T}{\partial x^2} + \frac{\partial^2 T}{\partial y^2} \right]$	Whole Geometry
2	Laser heat flux, natural convection cooling and radiation	$-k \frac{\partial T}{\partial y} = \beta P_g + h(T_{amb} - T) + \varepsilon \sigma (T_{amb}^4 - T^4)$	1
3	Natural convection cooling and radiation	$-k \frac{\partial T}{\partial y} = h(T_{amb} - T) + \varepsilon \sigma (T_{amb}^4 - T^4)$	2, 4
4		$-k \frac{\partial T}{\partial x} = h(T_{amb} - T) + \varepsilon \sigma (T_{amb}^4 - T^4)$	3
5	Material removal	$v_a = \frac{\beta P_g}{\rho H_s}$	1
6	Ablative heat flux	$q_a = h_a (T - T_v)$	1

In order to avoid the mesh size affecting the results, a mesh sensitivity analysis was carried out for four different mesh sizes and the optimal mesh size was used for computation. To reduce the computation time, the geometry domain is divided into two sections with different mesh sizes (Figure 27). Since the resultant ablation depths are expected to be smaller than 10 μm based on the

experimental measurements presented in Ch. 3.3.2, the top half of the geometry, where the deformation occurs, has the finest triangular meshing with a maximum element size of $1\ \mu\text{m}$ and minimum element size of $0.005\ \mu\text{m}$ to obtain the most accurate result that is comparable with the experimental values. The mesh of the bottom half section is set to physics-controlled extra fine mesh.

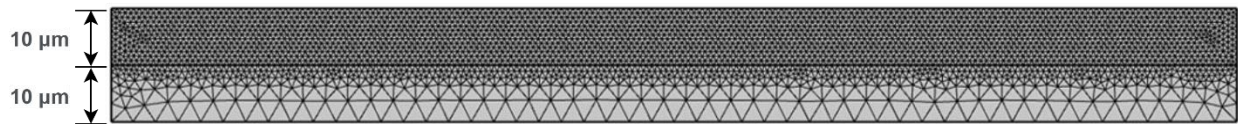


Figure 27. Free triangular mesh of the NiCr film.

4.3.3 Results and discussion

The ablation characteristics including temperature field and ablation morphology are greatly affected by the processing parameters. Figure 28 exhibits simulation results of an ablation process at different time nodes and the relations between cross-sectional profile and maximum ablation depth versus the number of pulses are plotted in Figure 29. As the repetition rate is $75\ \text{kHz}$, the single pulse width is $47\ \text{ns}$ and there is a $13.29\ \mu\text{s}$ cooling time after each pulse. Since the power intensity within the laser spot is Gaussian-distributed, the higher intensity in the central part resulted in a deeper ablation depth. Hence, the ablation pit by a single pulse has a tapered shape (Figure 28a). At time $47\ \text{ns}$, when the laser turns off during the first pulse, a pit with a depth of $1.1\ \mu\text{m}$ is generated at the starting point ($x=40\ \mu\text{m}$). Because of the short pulse duration, the heat flux does not diffuse far and so only the region around the ablation pit has a high temperature gradient, while the temperature of most of the region remains at room temperature. At the end of the first pulse (Figure 28b), the whole film is completely cooled down and the ablation depth is unchanged. After the second laser irradiation at time $13.38\ \mu\text{s}$, the ablation pit depth increased to $1.49\ \mu\text{m}$ due to the effect of pulse overlap and the heat concentrated in the area underneath the irradiated surface as shown in Figure 28c. The film is cooled down to ambient temperature again at the end of the second pulse (Figure 28d).

After the third pulse, the maximum ablation depth reaches a plateau at $1.55\ \mu\text{m}$ and so the ablated geometry is only extended in length and the depth remains constant after the fourth pulse (Figure 28g). The ablation depth gradually increases during single pulse irradiation. As can be

observed in Figure 28f ($t = 40.044 \mu\text{s}$, i.e., during laser-on time) and Figure 28g ($t = 40.091 \mu\text{s}$, i.e., after laser-on time), there is a small increase in depth as more heat passed onto the surface. The geometry after the fourth pulse has the same shape as the final geometry presented in Figure 28h.

Although numerically the ablation depth stabilizes after the third pulse, as shown in Figure 29a, the cross-sectional profile of the ablation geometry becomes identical after 9 laser pulses, and the peak-to-peak distance is equal to the distance between consecutive pulses. The variation in shape for the first few pulses (third to eighth pulses) is expected to be caused by relatively poor convergence at the beginning of the computation.

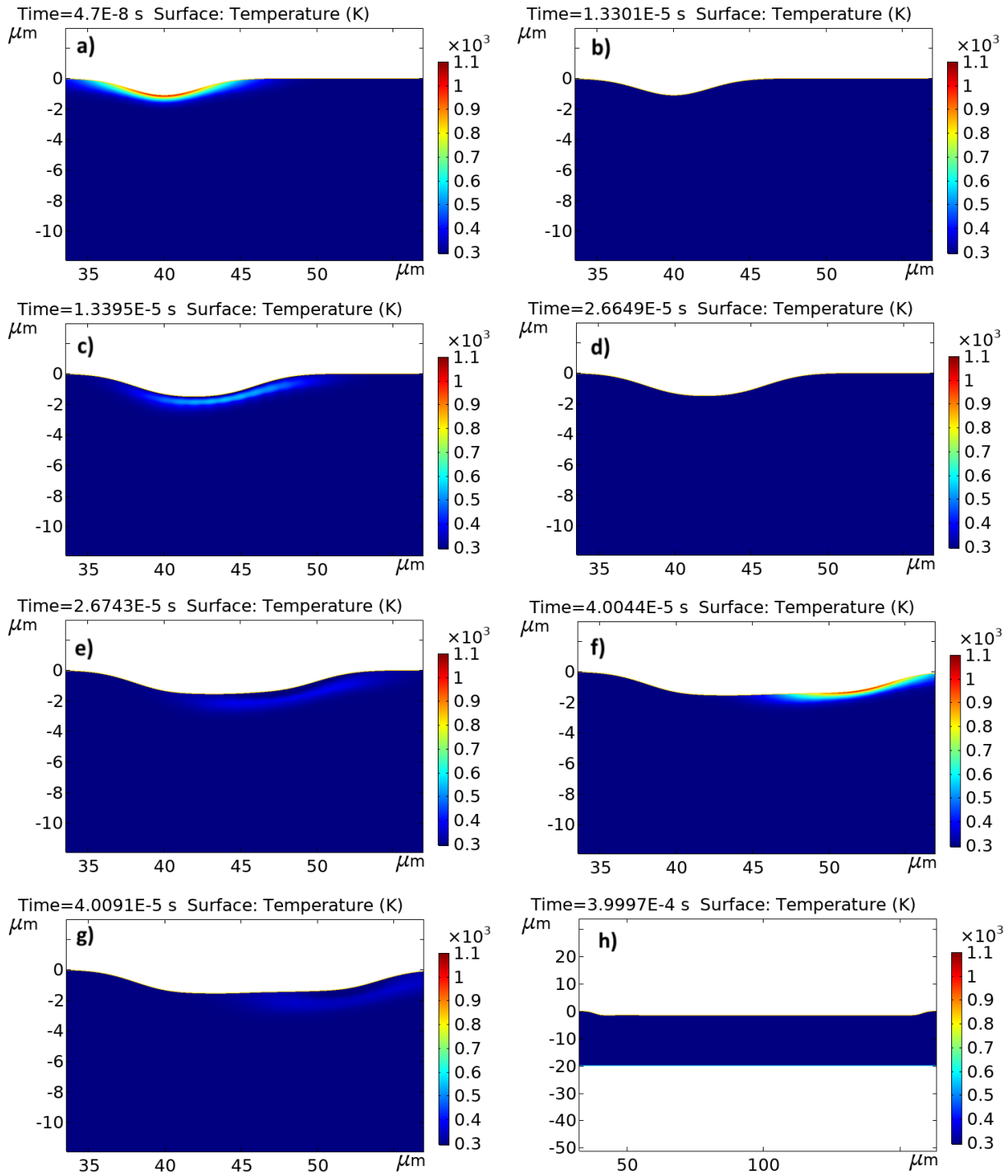


Figure 28. Ablation morphology at $t =$ a) 47 ns, b) 13.301 μs, c) 13.39 μs, d) 26.665 μs, e) 26.74 μs, f) 40.04 μs, g) 40.09 μs and h) 399.97 μs with $P_{avg} = 0.7$ W, $f = 75$ kHz, $P_w = 47$ ns, $V = 300$ mm/s.

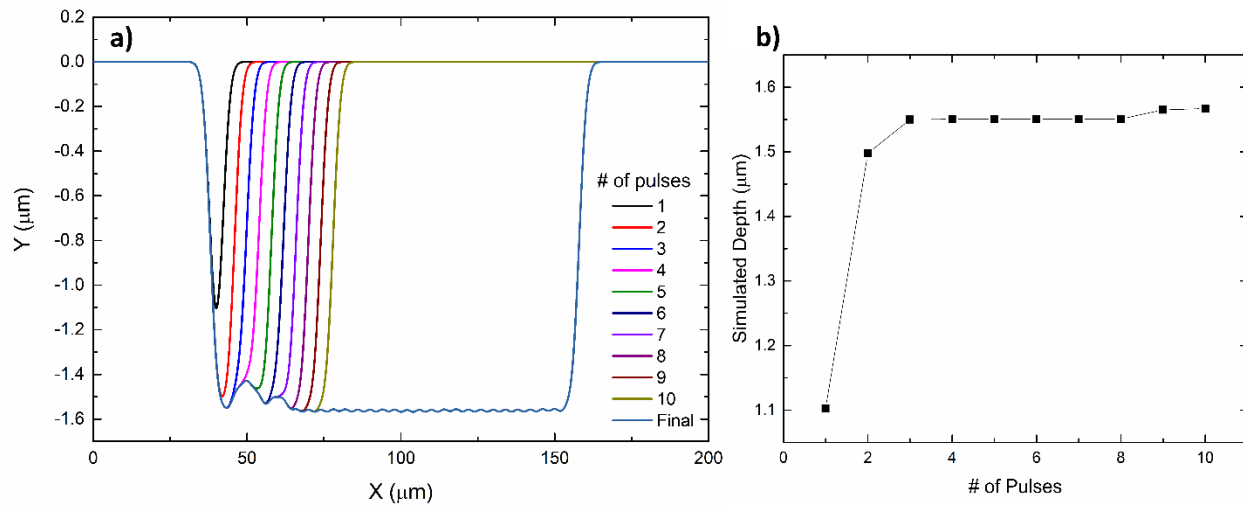


Figure 29. a) Cross-sectional profiles of the ablation geometry after different number of pulses; b) The simulated maximum ablation depth versus number of pulses.

As reported in Ch. 3.3.3, the pulse overlap has an important influence on the ablation morphology. To investigate the effect of pulse overlap, the univariate approach is applied, i.e., the other processing parameters are kept constant while the scanning speed is increased from 300 to 600 mm/s. As a result, the pulse overlap factor is doubled compared to the previous model (Figure 28). The ablation pit formed after the first laser remains the same with a maximum depth of 1.1 μm (Figure 30a vs. Figure 28a), because the pulse energy is constant regardless of the scanning speed. However, due to the faster speed, the distance between consecutive pulses is increased to 8 μm, and so the ablated spots overlap only a small area. Hence, after the second laser pulse, the maximum ablation depth is not affected, instead, there is a residual island between two ablation pits, which has a depth of around 0.5 μm. The temperature distribution is similar to the previous case, as the largest temperature gradient occurs near the surface and most of the region is almost unaffected (Figure 30b & c). In addition, the film is able to cool down to room temperature at the end of each pulse.

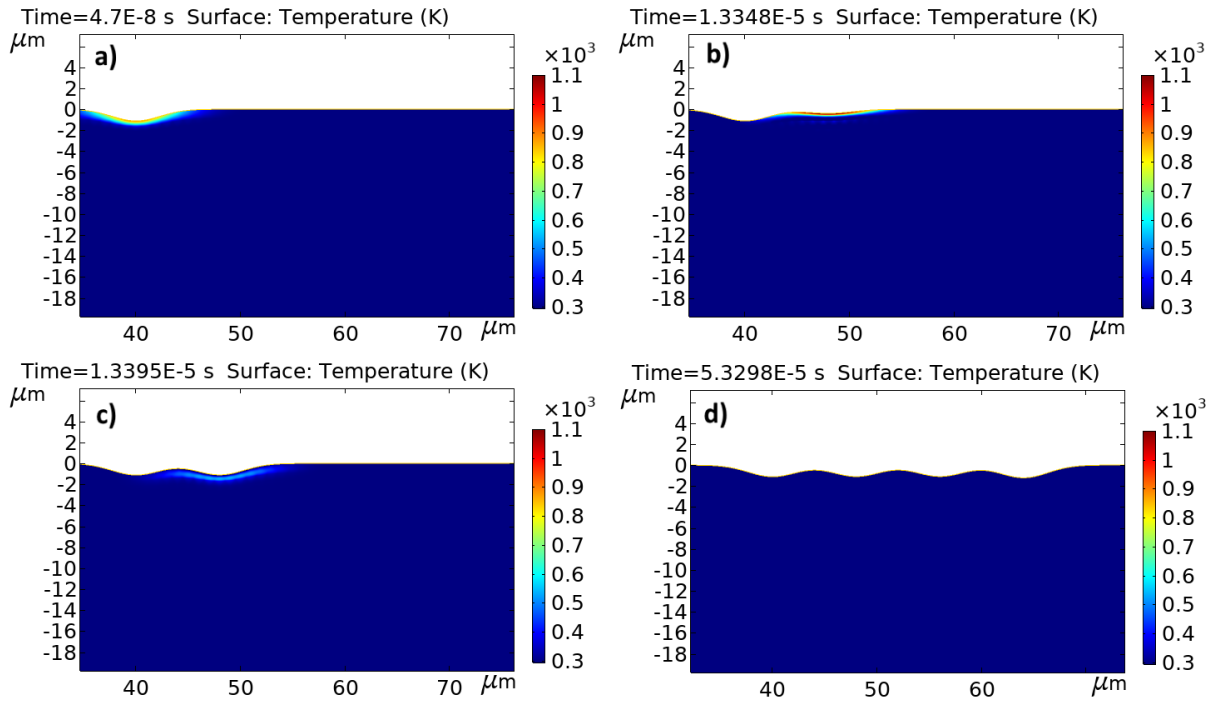


Figure 30. Ablation morphology at $t = a) 47 \text{ ns}$, $b) 13.34 \mu\text{s}$, $c) 13.39 \mu\text{s}$ and $d) 53.29 \mu\text{s}$ with $P_{avg} = 0.7 \text{ W}$, $f = 75 \text{ kHz}$, $P_w = 47 \text{ ns}$, $V = 600 \text{ mm/s}$.

To further analyze the impact of scanning speed, the cross-sectional profiles for five different speeds are plotted together in Figure 31a. As the speed decreases, the bottom surface of the ablation channel tends to be flatter. This is due to the insufficient pulse overlap at a fast speed, which results in an unablated island between two pulses, hence, leading to a large variation in ablation depth. The largest variation is at 600 mm/s , whose depth varies by around $0.5 \mu\text{m}$. This also explains the large difference between experimental and simulated ablation depth at 600 mm/s as shown in Figure 31b. Since the experimental depth is measured in the direction perpendicular to the ablated channel, it is possible that the measurement is taken at the pulse overlapped region where the residual island structure formed, instead of the center of a pulse, where the depth is maximum. The distance between these two locations is less than $4 \mu\text{m}$; hence, the depth value might be measured at the pulse overlapped region, which is close to the simulated island height ($0.5 \mu\text{m}$). At the speed of 200 mm/s , the simulated depth is larger than the value measured experimentally. This lower value might be caused by the shading of ejected particles after previous pulse irradiation, which

reduces the energy delivered to the target surface by the subsequent pulses. Since this effect is not considered in the simulation, the predicted depth is larger than the measured value at 200 mm/s.

It is interesting to note that the profile for the first pulse is consistent and independent of the speed as expected. For a speed of 500 mm/s and 600 mm/s, the maximum depths are almost the same (around 1.1 μm), which also equals to the first pulse depth reported in Figure 28a.

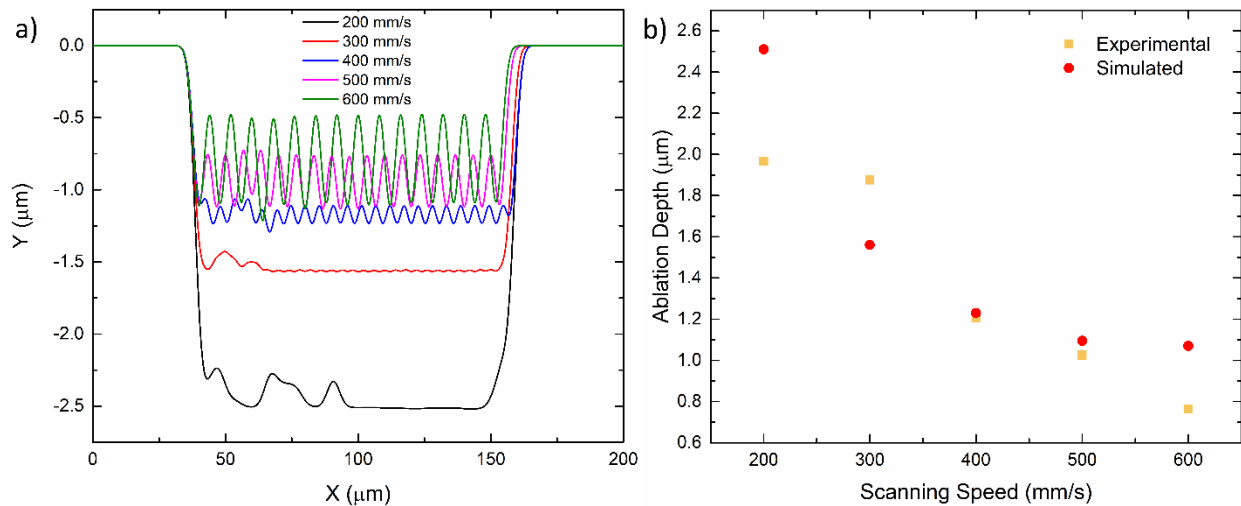


Figure 31. a) Cross-sectional profile of the ablation geometry at 0.7 W, 75 kHz with various scanning speeds; b) Comparison of experimental and simulated maximum ablation depth at different scanning speeds.

Another parameter controlling the overlap factor is the repetition frequency; therefore, the impact of the frequency on the ablation morphology is also investigated. As presented in Figure 32a, the cross-sectional profiles for four different frequencies are compared. The effect of frequency is similar to the effect of speed. The ablated channel has a smoother bottom surface at a higher frequency, attributed to the large overlap between consecutive pulses. Since the pulse energy varies with frequency, the first pulse depths are also different regardless of the pulse overlap distance. Compared to the experimental values, the largest variation is found at 30 kHz, this might also be due to the measurement location being a little off from the pulse center, where the power intensity is the highest. At 30 kHz, the depth is simulated to vary from 0.5 to 2.615 μm , therefore, a small variation in measurement location could lead to a large difference in the measured depth.

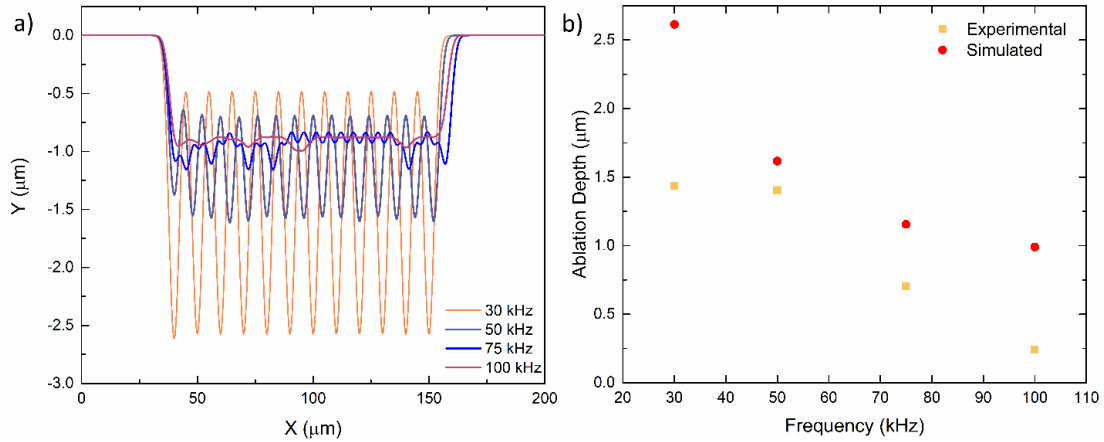


Figure 32. a) Cross-sectional profile of the ablation geometry at 0.6 W, 400 mm/s with various frequencies; b) Comparison of experimental and simulated maximum ablation depth at different frequencies.

To verify the accuracy of the simulation model, the obtained maximum ablation depths from the models are compared with the experimental depth values reported in Ch. 3 for 34 parameter sets (Figure 33). Generally, the simulation seems to be able to accurately predict the depth similar to the experimental measurements for an overlap factor larger than 0.5 and overpredicts the depth for overlap factors smaller than 0.5. Since the particle shielding has an important effect at large pulse overlap conditions and this effect is not considered in the simulation model, the simulated depth is often larger than the measured value for an overlap factor less than 0.5. On the other hand, these differences might be due to variations in measurement location. The measurement is expected to be taken at the center of a pulse where the deepest ablation occurs, however, it is difficult to measure exactly at the center point to get the actual maximum depth. Hence, the measured depths are smaller than the predicted values.

In addition, the variation between the experimental and predicted values could be reduced if more accurate material properties are available. Due to insufficient studies on the thermal properties of NiCr, the properties of pure Ni are used for approximation, which would affect the accuracy of the model when compared with the experimental results.

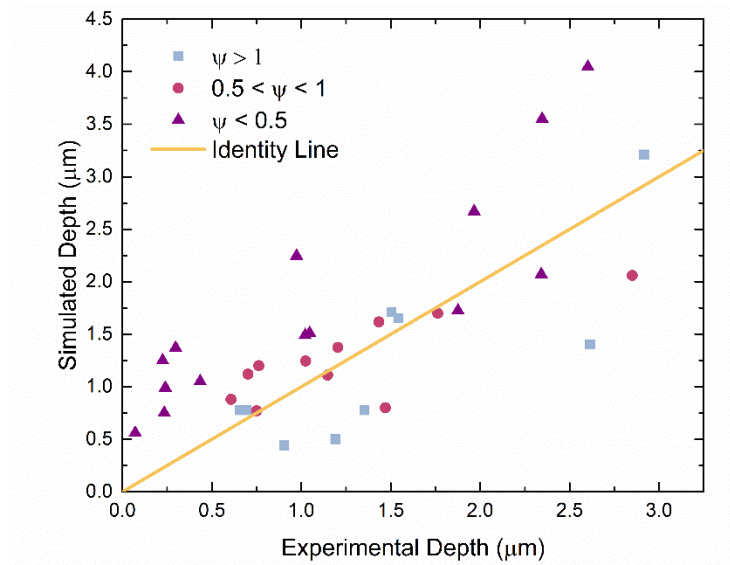


Figure 33. Simulated versus experimental maximum ablation depths.

To further compare with the experimental results, the equation that relates the ablation depth with incident fluence (Equation 4-3) is fitted to the simulated depth data and the best-fit parameters are summarized in Table 13. The obtained threshold fluence from simulation results (8.42 J/mm^2) is essentially identical to the empirical threshold value reported in Ch. 4.2.2 (8.47 J/mm^2). Furthermore, the simulated absorptivity of NiCr ($1.257 \text{ } \mu\text{m}^{-1}$) is also the same as the value derived from experimental depth values ($1.203 \text{ } \mu\text{m}^{-1}$). Hence, the simulation result shows a good agreement with the experimental data.

Table 13. Fit parameters of laser fluence and simulated ablation depth relationship.

Fit Parameters			Model Summary	
Form	$\alpha \text{ (}\mu\text{m}^{-1}\text{)}$	$F_{th} \text{ (J/mm}^2\text{)}$	R^2	NRMSE
Equation 4-3	1.257	8.4195	0.43	0.1891

4.4 Summary

The ablation depth and width are shown to have a logarithmic relationship with the incident laser fluence. A definition of laser fluence that considered the effect of various processing parameters including power, frequency, scanning speed and pulse duration is derived to obtain an empirical ablation threshold fluence from the experimental results presented in Ch. 3. This

threshold value is useful for predicting the geometry of the ablated structure based on the processing parameters. In addition, it was found that pulse overlap has an important influence on the ablation threshold value. The threshold value could be tripled with the smallest overlap due to the particle shielding effect, only partial pulse energy is delivered onto the target surface.

A finite element model is created in COMSOL to reveal the material removal process. For slower scanning speed, the maximum ablation depth gradually increases, which is attributed to larger pulse overlap. The simulation results show that the maximum depth reaches a plateau after three pulses at a speed of 300 mm/s. For fast speeds, the maximum depth is equal to the first pulse depth. Generally, ablation with a higher frequency and slower speed results in a smoother bottom surface. Overall, the findings from the simulations are consistent with the experimental observations and can be used to estimate a processing window according to the machining requirements.

Chapter 5 Dynamic response of laser fabricated strain gauge

5.1 Introduction

In previous two chapters, the laser ablation process on NiCr film has been detailly studied through the investigation on effect of laser parameters and the theoretical analysis. This process could be utilized to fabricate various flexible sensors. As an example, the application of laser ablation to fabricate NiCr-based strain gauges on flexible polyimide substrates to achieve comparable gauge resistance to a commercially available strain gauge is presented in this chapter. The sensitivity and resistance response of the strain gauge towards varying dynamic tensile loads are investigated. Additionally, several failure mechanisms of thin film strain gauges are discussed.

5.2 Materials and methods

5.2.1 Strain gauge fabrication

The thin-film strain gauges were fabricated using the steps shown in Figure 34, starting with a flexible polyimide substrate with a thickness of 75 μm . This was followed by a physical vapor deposition (PVD) step – performed by Angstrom Engineering, Canada – in which a 500 nm thick Evanohtm (NiCr) layer is deposited on the substrate. The Evanohtm layer is then patterned by laser ablation into the shape of a strain gauge. A UV laser system is used for patterning, with a 1 W laser, a wavelength of 355 nm, and a pulse width of 40 ns. A pulse energy of 11 μJ and an energy density of 0.23 J/mm^2 were selected for the patterning process. Since the development of strain gauges with more compact designs and smaller feature sizes are demanded, a high-precision laser system is required for microfabrication. Compared to CO_2 laser systems with longer wavelengths, which are widely used in manufacturing processes and rely on the photothermal effect, UV laser systems can reduce thermal damage to the patterned material and achieve smaller feature sizes due to a larger contribution from the photochemical effect [92,93]. The strain gauge pattern is designed to obtain a nominal 1025 Ω resistance, with curvature added to contact pads and traces to reduce the effect of sharp corners on fatigue life. The overall size of the strain gauge is 1.4 mm by 3.2 mm with a gage length of 1 mm.

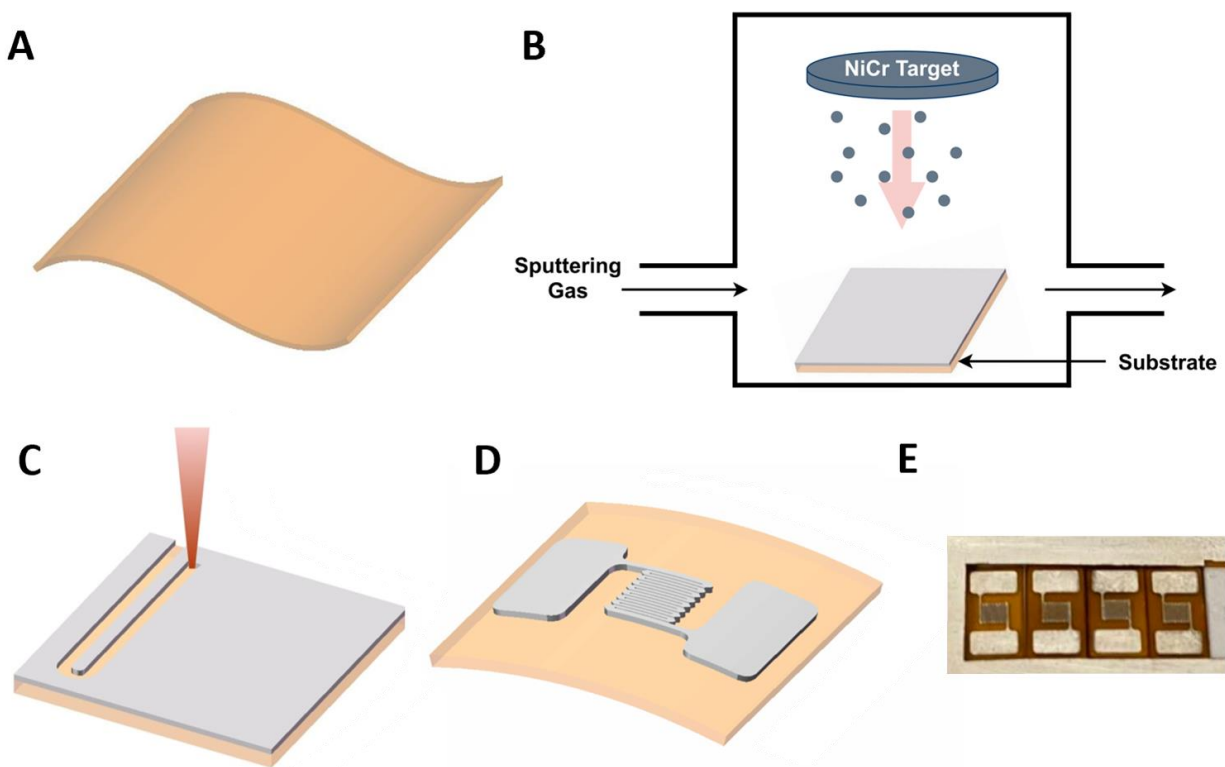


Figure 34. Schematic of the flexible thin-film strain gauge fabrication process. a) the flexible polyimide substrate; b) PVD deposition of the metallic NiCr layer; c) laser patterning of the strain gauge, d) laser fabricated thin-film strain gauge, and e) photo of fabricated strain gauge array.

5.2.2 Mechanical testing setup

To verify the sensitivity of the fabricated strain gauges, the gauge factor was measured and compared with a commercial strain gauge using a cantilever setup assembled on an Instron tensile tester (Figure 35a). A 5052 H14 tempered aluminum alloy beam with dimensions of $60 \text{ mm} \times 10 \text{ mm} \times 0.7 \text{ mm}$ was used as the cantilever. One end of the beam is fixed on the lower grip fixture of the tensile tester and the other end is free to move. The fabricated strain gauge was attached to the top surface of the cantilever, 11 mm away from the fixed end. The upper grip of the tensile tester applies a continuous range of tensile strains on the cantilever at a constant displacement load of 1 mm/min. An Agilent 34401A digital multimeter is used to monitor and record the electrical resistance of the strain gauge as the upper grip descends. The electrical connection between the mounted strain gauge's contact pads and lead wires was soldered with a tin/lead rosin core solder wire (63% Sn, 37% Pb).

During gauge factor testing, the strain experienced at the gauge's location was calculated from the extension data returned by the tensile tester. This was done starting with Equation 5-1, which relates the deflection of the beam (δ) at a distance (x) from the fixed end when a known force (F) is applied at a distance (a) from the fixed end, using the beam material's modulus of elasticity (E) and moment of inertia (I). The equation can be rearranged and solved for the force at position $x = a$ using the displacement results obtained by the tensile tester as shown in Equation 5-2. This expression for the force can then be substituted into the equation for the bending moment at location x (Equation 5-3).

$$\delta = \frac{-Fx^2}{6EI}(3a - x) \quad (5-1)$$

$$F = \frac{-3\delta_a EI}{a^3} \quad (5-2)$$

$$M = -F(a - x) = \frac{3\delta_a EI}{a^3}(a - x) \quad (5-3)$$

The stress at location x on the top surface of the beam can be expressed as shown in Equation 5-4, in terms of the bending moment, half the beam thickness (c) and the moment of inertia. This expression can then be substituted into the equation for strain, as shown in Equation 5-5. The benefit to this approach is that it does not require knowledge of the beam's properties (E), and only requires reading of the displacement (δ_a) at position a , the position of the strain gauge on the beam (x), and half of the beam thickness.

$$\sigma = \frac{Mc}{I} = \frac{3\delta_a Ec}{a^3}(a - x) \quad (5-4)$$

$$\varepsilon = \frac{\sigma}{E} = \frac{3\delta_a c}{a^3}(a - x) \quad (5-5)$$

Long-term cyclic fatigue testing was conducted by applying dynamic bending loading on the test beam. The test beam is prepared in a similar manner as the gauge factor test, then installed on a cyclic testing fixture (Figure 35b) with cams of different sizes to apply different deflections. The cam is driven by a DC stepper motor to apply a cyclic tensile strain at up to 4.36 Hz. As the

cam rotates, the metal beam will be pushed downward and the deflection of the beam will transfer to the strain gauge, resulting in a change in its resistance. Due to the shape of the cam, one full cam rotation results in three beam bending cycles.

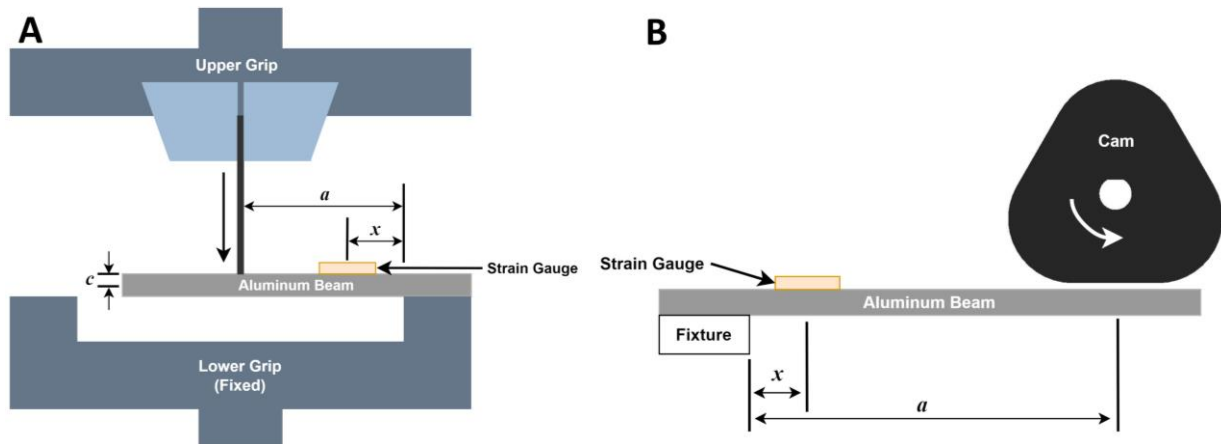


Figure 35. Schematic of experiment setup for a) gauge factor testing and b) dynamic testing.

5.2.3 Characterization

The microstructure and morphology of the strain gauge were characterized using scanning electron microscopy (SEM, Zeiss Leo and Zeiss Ultra Plus). The electrical properties of fabricated strain gauges were measured by a four-point probe (Keithley 4200-SCS), specifically to identify defects and causes of sensor failure by measuring and comparing the resistance of each conductive trace.

5.3 Results and discussion

5.3.1 Strain gauge characterization

A representative sample of the final fabricated strain gauge is shown in *Figure 36a*, with the soldered contact pads visible in the top left and bottom right corners of the image, the winding conductive trace connecting the two contact pads visible in between, and the exposed polyimide substrate appearing dark under the SEM. A higher magnification image in *Figure 36b* displays a visible texture on the exposed polyimide, caused by the laser tracks used to ablate the Evanohm layer. Some spatters along the edge of the conductive trace also exist due to molten material splashing and solidifying outside of the laser ablated region. This suggests that UV laser irradiation of the NiCr thin film induces melting as expected in a nanosecond pulsed laser ablation process,

and the material ablation likely occurs due to the formation of vapor and ejection of liquid droplets [94,95]. A tilted view of the conductive trace and underlying polyimide is shown in *Figure 36c*, showing the material buildup at the edge of the traces, and the peaks left behind by the ablation process in the exposed polyimide.

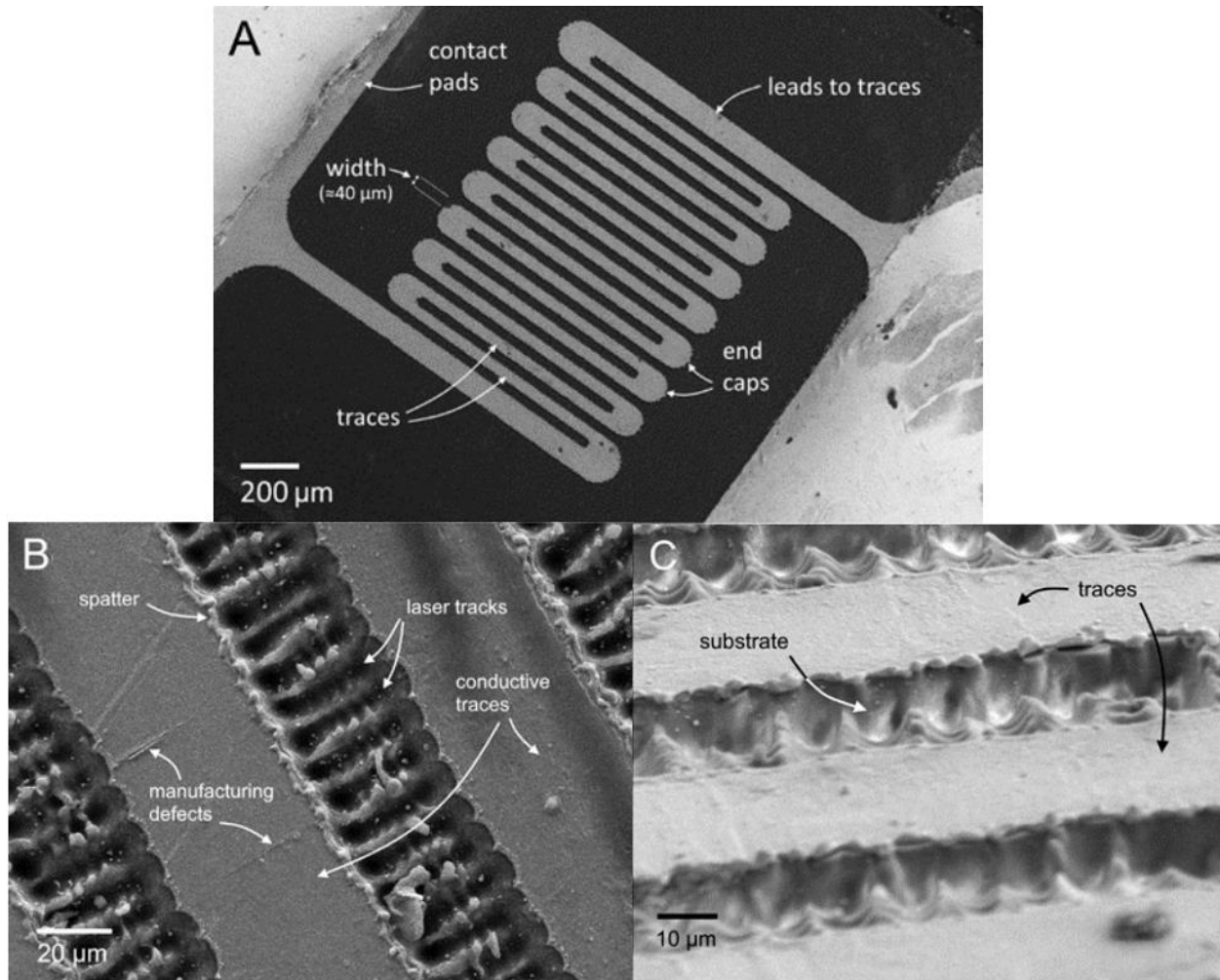


Figure 36. SEM images showing a) the strain gauge overview and terminology, b) higher magnification image of the traces, and c) a tilted view of the traces.

An average width of $40.2 \mu\text{m} \pm 3.5 \mu\text{m}$ was measured for the conductive traces in the strain gauges as labelled in *Figure 36*. A summation of all the lengths (L) and widths (w) in the conductive path (*Table 14*) that composes the strain gauge is used in Equation 5-6 to determine the expected resistance of the fabricated strain gauge, where ρ is the electrical resistivity of Evanohm ($133 \Omega \cdot \text{cm}$) and t is the Evanohm thickness (500 nm). The average measured resistance

of the laser fabricated strain gauges is $1048 \Omega \pm 53 \Omega$, in agreement with the calculated resistance of approximately 1025Ω . The slight variation in the patterned strain gauge dimensions can cause slight difference in the measured resistance.

Table 14. Dimensions of the conductive path as described in Figure 36a.

Location	Width	Length
Leads	$84.8 \mu\text{m} \pm 5.4 \mu\text{m}$	0.31 cm
End caps	$108.1 \mu\text{m} \pm 6.4 \mu\text{m}$	0.14 cm
Traces	$40.2 \mu\text{m} \pm 3.5 \mu\text{m}$	1.35 cm

$$R = \sum_1^n \frac{\rho L_n}{tw_n} \quad (5-6)$$

The gauge factor, defined as the relative change in resistance ($\Delta R/R$) to the relative change in length (or strain, ϵ), denotes the strain gauge's sensitivity to an applied strain. This value is obtained from the slope of the linear region of the $\Delta R/R$ versus strain curves in *Figure 37*, with a resulting gauge factor of 2.3 ± 0.2 . This value is a combination of the dimensional changes and resistivity changes of the metal layer when strained, as well as the ability of the cyanoacrylate adhesive and polyimide substrate to transfer the strain from the aluminum beam to the metal layer [96]. For comparison, the gauge factor was measured for a conventionally manufactured commercial strain gauge with an Evahnm sensing layer approximately $3.5 \mu\text{m}$ thick, and was found to be 2.0 ± 0.4 . The two gauge factors are statistically similar and are within the expected range [97]. Although recent research has proposed supersensitive strain gauges with gauge factors larger than 5000 [98], the gauge factor is usually determined by the material composition. For Evahnm strain gauges, the gauge factor is reported to be in the range of 1.95 to 2.5 and it is constant for a film thickness of 15 nm and above [56].

Notable deviations from a linear response are observed when crack opening occurs, as can be seen in the red dotted line in *Figure 37*. As the crack faces separate with increasing strain, the measured resistance increases faster than would be expected due to the changing dimensions of the traces alone, a phenomenon known super-sensitivity [99]. Although some strain gauges can

incorporate pre-made cracks for this purpose [98], the presence of cracks in the flexible thin film strain gauge of this study results in a non-linear response that is detrimental to the accurate correlation of resistance change to strain.

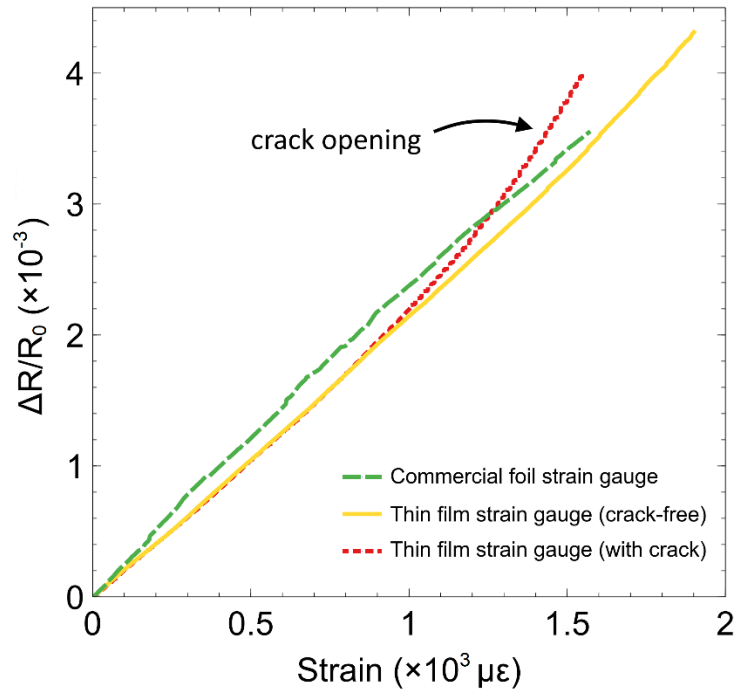


Figure 37. Example of three tensile gauge factor tests. The green (dashed) and yellow (solid) lines show the expected almost-linear response, while the red dotted line shows an apparent increase in the gauge factor caused by crack opening.

5.3.2 Cyclic resistance response

A total of 24 strain gauges were fatigue tested in tension at various strains, as shown in *Figure 38*. Failure was not observed below 1750 $\mu\epsilon$ while the highest strain level that resulted in a sample reaching over 10^6 cycles was 2625 $\mu\epsilon$. The rated fatigue life of the commercial strain gauge with a similar sensing layer composition and substrate material is approximately 10^6 cycles at $\pm 1800 \mu\epsilon$, or 10^6 cycles at 3240 $\mu\epsilon$ when only tested in tension. However, commercial strain gauges have a protective top coating, and testing conditions (testing fixture, testing frequency, adhesive, etc.) for the commercial and current thin film strain gauge are different. Above 1750 $\mu\epsilon$, two failure mechanisms can be identified in the thin film strain gauges. Four samples which survived on the order of 10^3 to 10^5 cycles at elevated stain levels suffered from open circuit failures

that manifested as an infinite resistance reading on the multimeter. Nine strain gauges also tested at high strain levels experienced response degradation, which includes significantly larger resistance change during cycling than expected and/or a translation of the resistance curve.

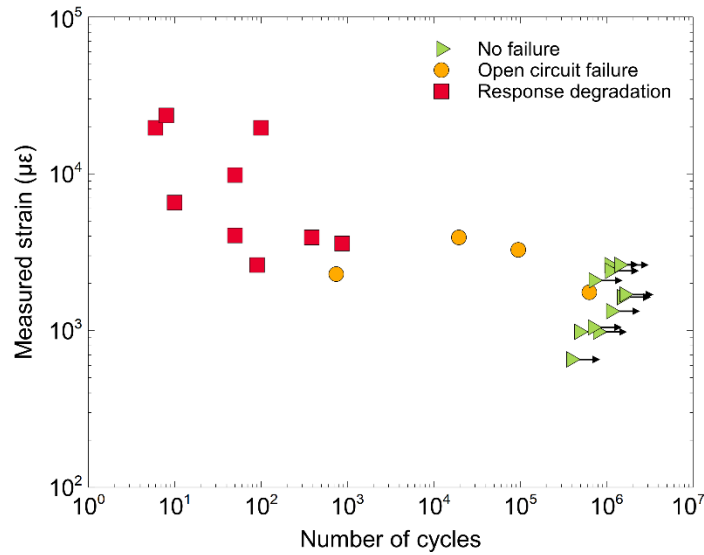


Figure 38. Results of fatigue testing of strain gauges at various strains. Tests were typically interrupted around 10^6 cycles, at which point they were considered runout samples.

A typical cyclic response is shown in *Figure 39a*, after the data is processed with a 5-point moving average filter to reduce noise. Strain gauges that experience runout maintain a consistent resistance change throughout the entire test, although slight variations in resistance change can be observed when looking more closely at individual cycles (*Figure 39c*). Since these samples are tested in tension, the resistance is at its lowest point when the beam and strain gauge are flat and at the highest point when fully bent. The amount of bending dictates the strain measured at the location on which the strain gauge is mounted to the beam. Small differences in the size of the three cam corners (*Figure 35b*) that induce bending result in slightly different resistance changes that repeat consistently throughout the test. When a strain gauge is in good condition – without cracks or defects as in the case of *Figure 39c* – the small difference in resistance response caused by the imperfect cam shape can be distinguished (labeled “cam peaks”). However, strain gauges that are damaged and are exhibiting super-sensitivity are no longer sensitive to the difference in the cam peaks (*Figure 39d*).

Strain gauges that exhibited an open circuit failure mode showed atypical resistance changes prior to complete failure, as shown in *Figure 39b*. A slight increase in the resistance change when bent was observed near 9.3×10^4 cycles, which is attributed to the formation of the fatigue crack and separation of the crack faces during bending. This is followed by an infinite resistance reading near 9.4694×10^4 cycles as shown in *Figure 39d*. Continuing to cycle the strain gauge shows the resistance returning to the original un-strained value, explained by the crack opening fully while the strain gauge is bent and then closing fully when returned to the flat position. Further cycling shows an increase in the resistance measured when returned to the flat position, suggesting that further damage occurs and the crack faces improperly mate, until the measured resistance is infinite regardless of whether the strain gauge is bent or flat.

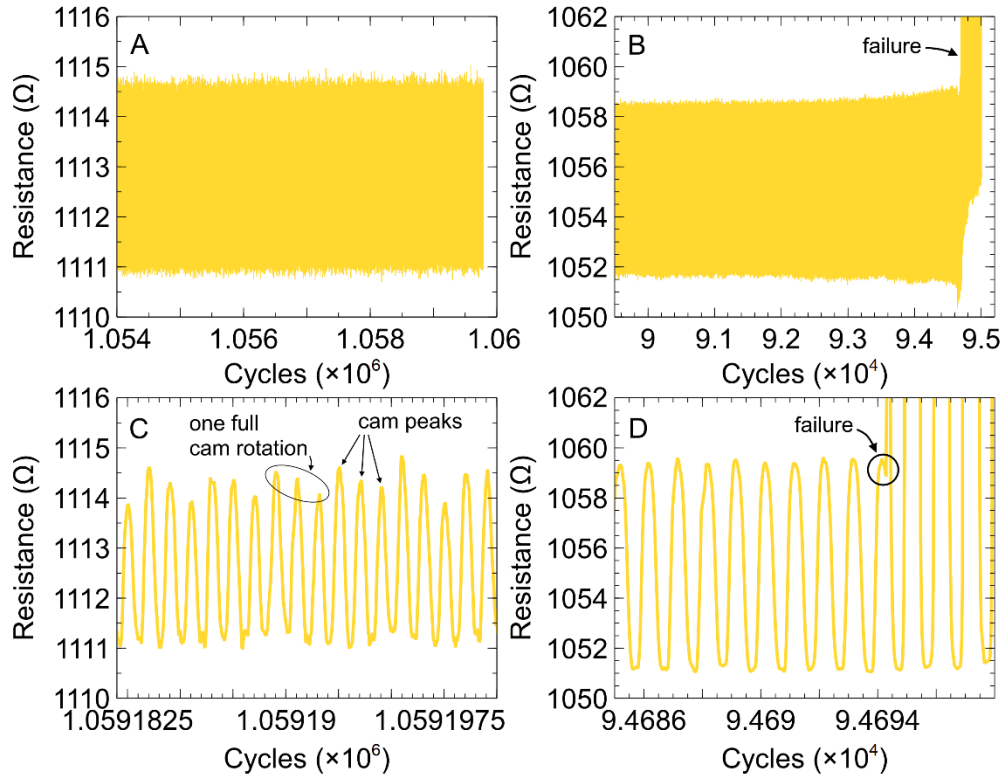


Figure 39. Cyclic response for strain gauges with a) no failure and b) open circuit failure, with higher magnification of the response curve shown in c) and d), respectively.

5.3.3 Failure mechanisms

Crack networks and limited material extrusion as shown in *Figure 40* were observed on strain gauges with open circuit failures. Small crack networks were also visible on samples that

reached runout and were considered to have not failed, although in these cases the cracks occupied a small fraction of the entire trace width. This type of failure mechanism was reported in studies of Cu and Ag films by Kraft et al [100] and Zhang et al [101], specifically identified as a transition from larger material extrusion and transgranular cracking in thicker films with larger grain sizes, to minimal extrusion and intergranular cracking in thin films with smaller grains. A decrease in grain size and a decrease in film thickness are expected to increase the fatigue life. This was demonstrated by Kim et al. [102] when comparing a 200 nm Cu film to that of a 1 μm Cu film under the same bending strain conditions, showing the thicker film undergoing fatigue failure while the thinner film does not. Zhang et al [101] suggests that the small thicknesses and small grain sizes inhibit dislocation formation and movement during fatigue.

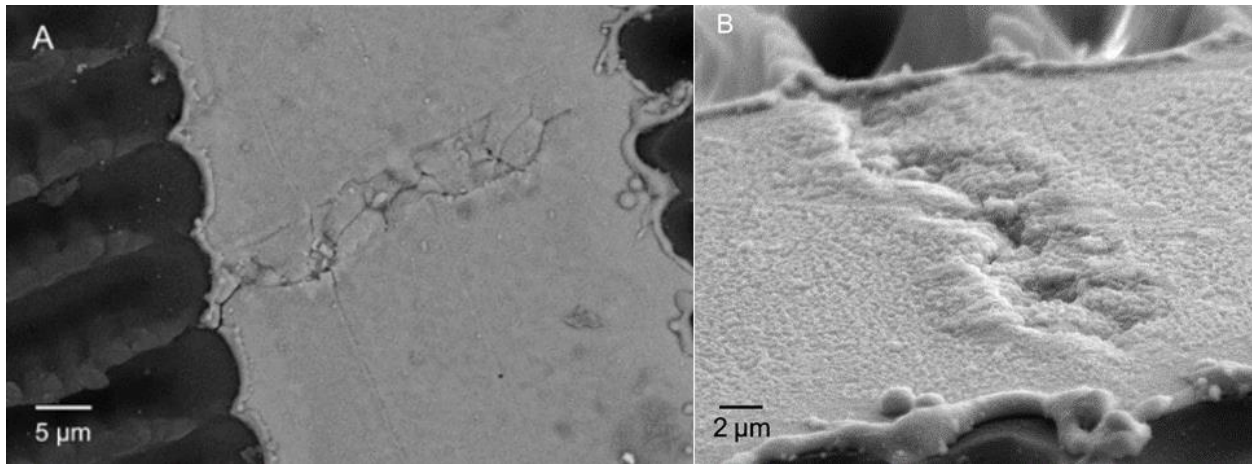


Figure 40. Crack networks viewed from a) above and b) at an angle after cyclic bending loading.

Strain gauges that suffered from “response degradation” as labeled in *Figure 38* displayed unusual cyclic responses such as increases in resistance and baseline shifts that would qualify the strain gauge as unfit for use in real-world applications. When these responses appeared during cyclic testing, the strain gauges would be considered as failed. A four-point probe was then used to evaluate the resistance of individual trace sections in both unstrained and strained conditions to identify which traces were responsible for the increased resistance or unusual response. Theoretically, the resistance of traces #2-16 should be identical while leads #1 and #17 have smaller resistance due to their larger widths (labeled as “leads to traces” in *Figure 36*). However, there are some small variations in resistance between traces on the same strain gauge or between

different strain gauges in the as-fabricated condition as shown in *Figure 41a*. This can be attributed to previously identified variations in trace widths (*Table 14*) and the presence of small defects that can occur during laser patterning (*Figure 36b*). *Figure 41b* compares the resistance of two strain gauges that have abnormal resistance responses during long-term cyclic testing. If localized damage is occurring in the form of cracks, some traces should only experience slight increases in resistance due to bending while other damaged traces will experience larger than expected value. The first strain gauge (Sample 1) experiences larger than expected increases in resistance (based on the gauge factor and the applied deflection) on traces #2 (10 Ω), #3 (7 Ω), #5 (7 Ω), and #6 (13 Ω) in the bent condition; while the second strain gauge (Sample 2) shows significant increases in trace #2 (137 Ω), #7 (18 Ω), #8 (40 Ω), and #16 (7 Ω). Obviously, the largest contributors to the failure of Sample 2 appear in trace #2 and #8. This suggests cracks in traces with large resistance increases are opening when a strain is applied, and failure may be localized to a small number of traces while others continue to function normally.

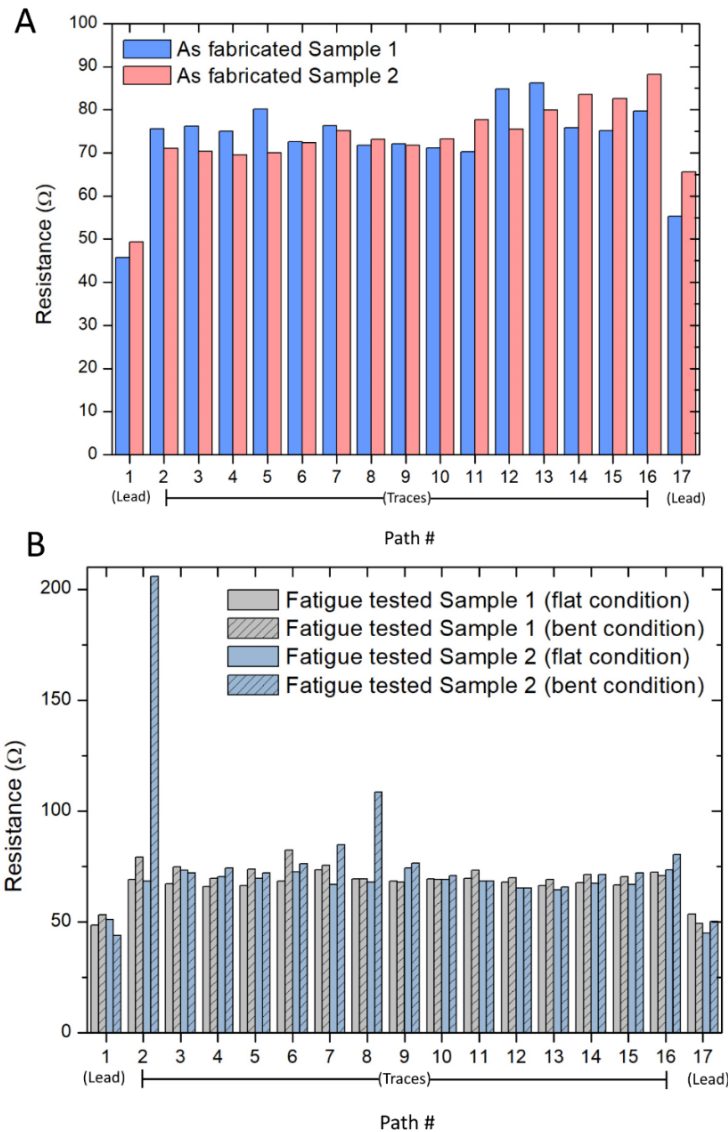


Figure 41. Comparison of individual conductive traces' resistance at flat and bent conditions for a) as-fabricated strain gauges and b) fatigue-tested strain gauges.

The first failure mode identified from resistance measurements is shown in *Figure 42*. This strain gauge experiences a regular cyclic response – although with a larger resistance change than expected – and suddenly experiences an upward shift in resistance when returning to the flat position on each cycle as shown in *Figure 42a*. The larger than expected resistance change in the traces suggests that crack opening is occurring under high strain, and upward resistance shift when returning to the flat unstrained position suggests the crack faces are mating incorrectly (as

proposed in *Figure 42b*). *Figure 42c* identifies delamination between the Evanohm and the polyimide at the site of cracking, which may account for the unstrained resistance shift. The crack begins to close as the beam unbends, which decreases the resistance. However, prior to reaching the fully unstrained position, the crack opens back up as the Evanohm buckles and causes a resistance increase.

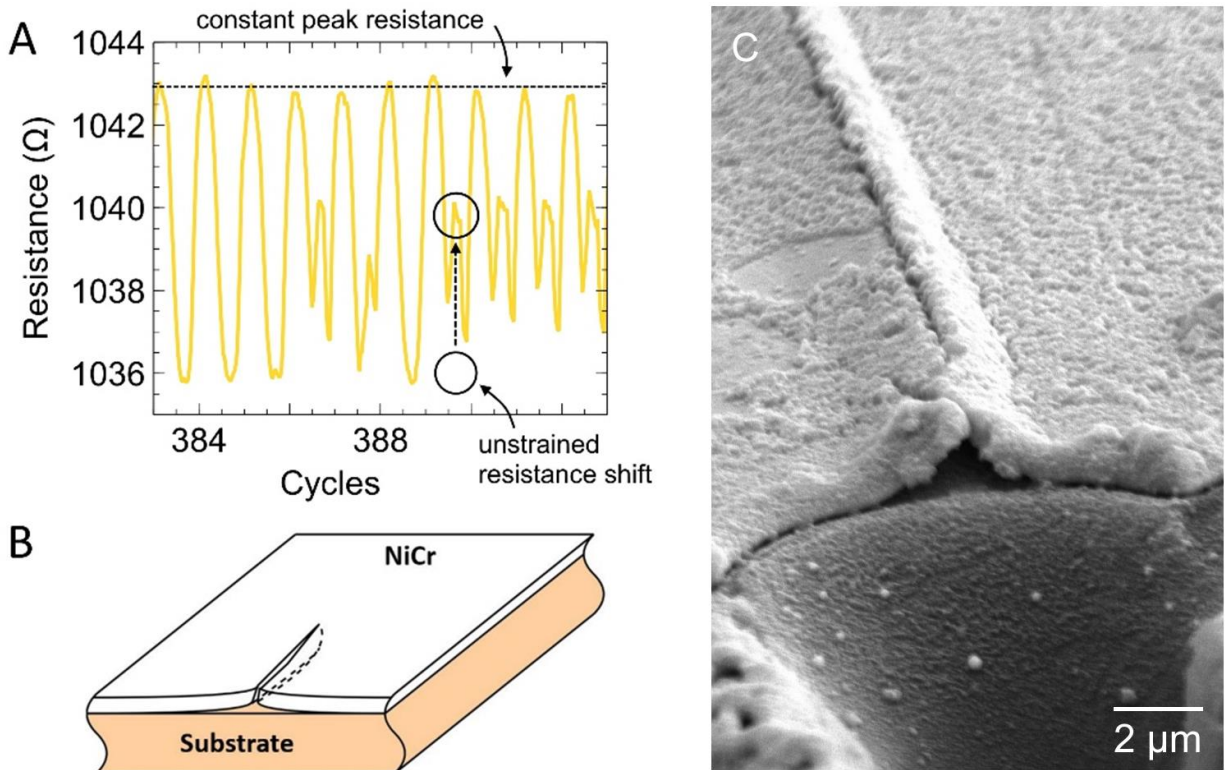


Figure 42. a) Response degradation failures showing upward shift in unstrained resistance while maintaining a constant peak resistance; b) schematic of crack and delamination after strain being released, and c) SEM image of delamination and crack in traces.

A second failure mode is shown in *Figure 43*, where both the peak and baseline resistance during cycling increases, but the peak resistance is a finite value and not an open circuit failure as was shown in *Figure 39*. Instead, the strain gauge continues to display a cyclic response, but the change in resistance is not representative of the strain experienced by the beam. The increasing peak resistance with increasing cycling suggests that crack growth is occurring, while the upwards drift in the baseline resistance indicates that the cracks do not fully close when returning to an

unstrained state (Figure 43b). Figure 43c shows a SEM image of this remaining open crack when returned to the flat position. The rough crack edges suggest that an intergranular cracking mechanism may be occurring. These cracks might be initiated at the edge of traces due to the rapid cooling during laser irradiation, which can then propagate into the trace caused by residual stresses and further grow under an applied stress during testing.

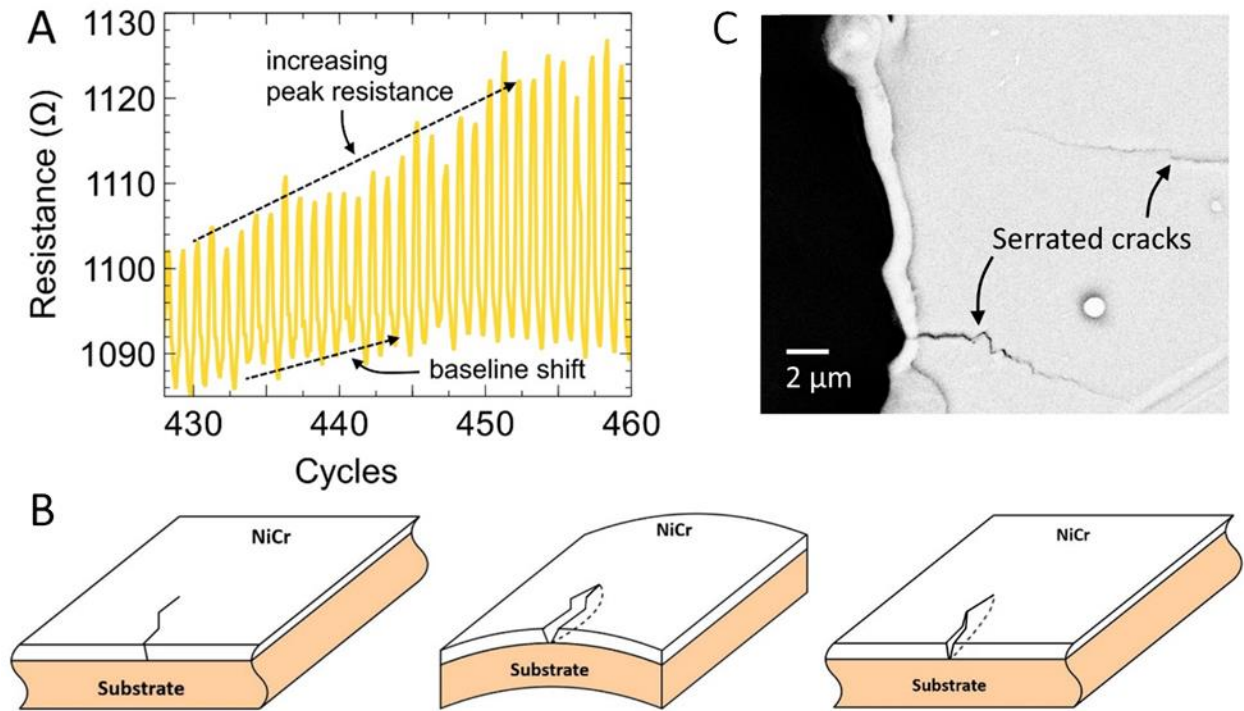


Figure 43. a) Resistance response showing upward shift in baseline with increasing peak resistance; b) schematics showing a crack from initial unstrained condition, crack opening during bending, and crack remaining partially open after stress release; c) SEM image of a crack in the unstrained position.

All cracks observed in the Evanohm traces initiated from the edge and propagated across the trace. Several possible approaches can be used to address this. The first is to reduce edge defects that appear during manufacturing, which may act as initial sites for crack formation during loading. These defects are theorized to occur due to thermal cycling during patterning and molten material solidifying after laser exposure. This can be addressed by using picosecond or femtosecond laser systems that rely less on the photothermal effect to remove material. Otherwise,

reducing the pulse energy and increasing the number of passes by the UV nanosecond laser to minimize the thermal gradients and the quantity of molten material generated during processing can also address the formation of these defects. Secondly, the serrated nature of the trace edges may introduce regions with higher stress concentration during bending, encouraging crack nucleation and propagation. Careful control of pulse overlap can be used to obtain straighter edges. Lastly, applying a suitable coating with sufficient stiffness [103] could deter manufacturing defects from propagating or fatigue cracks from forming, although care would have to be taken to prevent the coating from affecting the sensitivity of the strain gauge.

5.4 Summary

The laser fabrication of a flexible thin-film strain gauge using UV laser ablation was demonstrated. The strain gauge characteristics and the dynamic tensile performance were evaluated. The experimentally measured resistance for the fabricated strain gauges ($1048 \Omega \pm 53 \Omega$) was close to the expected theoretical resistance of 1025Ω . Additionally, a gauge factor of 2.3 ± 0.2 was measured, which matches the gauge factor of commercially available Evanohm foil-based strain gauges.

Resistance measurements of individual strain gauge traces after cyclic loading in both the strained and unstrained conditions exhibited that failure was attributed to defects occurring on a fraction of the traces while the majority continued to function normally. Fatigue failure ($< 10^6$ cycles) during cyclic bending loading was not observed below $1750 \mu\epsilon$, and the highest strain level at which a strain gauge experienced runout was $2625 \mu\epsilon$.

Several failure mechanisms were identified. Open circuit failures in samples that survived 10^3 to 10^5 cycles were attributed to the growth of fatigue crack networks in the sensing layer. Response degradation of samples that survived less than 10^3 cycles was attributed to two types of failures. The first is a combination of cracking and delamination, which manifested as a peak in the unstrained resistance during cyclic testing. The second is the growth of cracks without delamination which manifested as an increasing baseline resistance and an increasing peak resistance.

Chapter 6 Conclusion

6.1 Conclusion

Laser ablation has the potential to cost-effectively fabricate flexible sensors without sacrificing high resolution. An experimental study is performed to investigate the effect of laser parameters on the ablation process of NiCr film, including average power, repetition frequency, and scanning speed. A response surface methodology was implemented to quantify the relationship between these three laser parameters and the resulted ablation width and depth. It was found that the laser power and frequency have a more significant effect on the dimension of the ablated geometry since they are major factors in determining the amount of energy passed on to the film. The ablation width and depth usually increase with increasing power or decreasing frequency. In addition, larger heat-affected zones were observed at lower frequencies, especially at a high laser power, due to the large energy input. Although the scanning speed has limited influence on the width of the ablated channel, it has a more pronounced effect on the edge shape and surface morphology of the resulted geometry due to the difference in pulse overlap factor. A large pulse overlap could facilitate the production of microchannels with smoother edges.

To improve the efficiency of laser energy utilization and enhance the ablation rate, a theoretical analysis of the ablation process is conducted. An analytical method based on Beer's law and the Gaussian beam profile is implemented to relate the ablation width and depth with incident laser fluence. A new laser fluence definition that incorporates the impact of all laser parameters is derived. By fitting the experimental data into the equations, an empirical threshold fluence is obtained. The pulse overlap factor was found to have an important influence on the threshold fluence. As the overlap increases, more energy input is required to initiate the ablation process, attributed to the shielding effect of the cluster ejected in previous pulses that scatters and absorbs a fraction of the laser energy of the subsequent pulses. This analytical method provides a guideline for selecting processing parameters based on the desired sensor geometry.

Due to the extremely fast dynamic interaction process between the laser and the material in the ablation process, it is usually difficult to make observations during the experiment, hence a finite element model is built to reveal the material removal process, especially the patterning morphology. The general trend is that the higher the frequency and slower the scanning speed, the

smoother the bottom surface of the ablated channel. The simulated ablation depth has a good match with the experimental values when the pulse overlap factor is larger than 0.5. This computation model could be used to improve the efficiency in the trial-and-error process of designing experiments to find the optimal processing parameters for other film materials or thicknesses.

Furthermore, the fabrication of a 1025 Ω flexible thin film strain gauge using a UV laser patterning process is demonstrated. The strain gauges exhibit a sensitivity comparable to the conventionally fabricated commercial alternative. Long-term cyclic fatigue testing was conducted to evaluate its resistance response to dynamic bending loading for a total of 24 strain gauges. It was found that the laser-fabricated strain gauges can reliably survive 10^6 cycles up to 1750 $\mu\epsilon$. Above this strain level, several failure mechanisms are identified, with unique electrical responses corresponding to physical damage observed on the strain gauges. These findings provide a guide to diagnose thin film strain gauge failures, demonstrate an unconventional fabrication technique, and show its potential for use in long-term dynamic load sensing applications.

6.2 Recommendation for future work

Future work of this research can be performed from two aspects, expanding the application of the laser ablation process to other materials and sensor fabrication, and further investigation and improving the performance of the laser fabricated strain gauges.

This study focused on the ablation of NiCr film. With some simple modifications, this process could be applied to fabricate other types of devices using NiCr such as capacitive strain gauges. Further research in studying laser ablation of nanomaterial-polymer composites would also be of great value, as this type of material has great potential for wearable electronics due to its excellent stretchability.

The simulation results show a good agreement with the experimental data for a pulse overlap factor larger than 0.5. The accuracy of the presented model could be further improved by considering some physical effects during the ablation process, such as particle shielding and hydrodynamic motion of the melted material.

On the other hand, one of the included studies evaluated the laser fabricated strain gauge characteristics and its dynamic tensile performance. The performance of the strain gauge under

environmental influences such as operating temperature, magnetic fields and humidity would be of interest, to further compare with the conventionally fabricated commercial alternative.

References

- [1] H. Choi, S. Choi, H. Cha, Structural Health Monitoring system based on strain gauge enabled wireless sensor nodes, Proceedings of INSS 2008 - 5th International Conference on Networked Sensing Systems. (2008) 211–214.
<https://doi.org/10.1109/INSS.2008.4610888>.
- [2] M. Cheng, G. Zhu, F. Zhang, W. lai Tang, S. Jianping, J. quan Yang, L. ya Zhu, A review of flexible force sensors for human health monitoring, J Adv Res. 26 (2020) 53–68.
<https://doi.org/10.1016/J.JARE.2020.07.001>.
- [3] A.G. Leal-Junior, A. Frizera, C. Marques, M.R.A. Sánchez, T.R. Botelho, M. v. Segatto, M.J. Pontes, Polymer optical fiber strain gauge for human-robot interaction forces assessment on an active knee orthosis, Optical Fiber Technology. 41 (2018) 205–211.
<https://doi.org/10.1016/J.YOFTE.2018.02.001>.
- [4] K. Bethe, D. Schön, Thin-film strain-gauge transducers, 1980.
- [5] A.K. Bose, X. Zhang, D. Maddipatla, S. Masihi, M. Panahi, B.B. Narakathu, B.J. Bazuin, J.D. Williams, M.F. Mitchell, M.Z. Atashbar, Screen-printed strain gauge for micro-strain detection applications, IEEE Sens J. 20 (2020) 12652–12660.
<https://doi.org/10.1109/JSEN.2020.3002388>.
- [6] J. Longtin, S. Sampath, S. Tankiewicz, R.J. Gambino, R.J. Greenlaw, Sensors for Harsh Environments by Direct-Write Thermal Spray, IEEE Sens J. 4 (2004) 118–121.
<https://doi.org/10.1109/JSEN.2003.822218>.
- [7] L. Overmeyer, J.F. Duesing, O. Suttmann, U. Stute, Laser patterning of thin film sensors on 3-D surfaces, CIRP Annals. 61 (2012) 215–218.
<https://doi.org/10.1016/J.CIRP.2012.03.087>.
- [8] O. Suttmann, M. Gosselin, U. Klug, R. Kling, Picosecond laser patterning of NiCr thin film strain gages, Frontiers in Ultrafast Optics: Biomedical, Scientific, and Industrial Applications X. 7589 (2010) 758914. <https://doi.org/10.1117/12.840842>.

- [9] L. Li, M. Hong, M. Schmidt, M. Zhong, A. Malshe, B. Huis In'tveld, V. Kovalenko, Laser nano-manufacturing – State of the art and challenges, *CIRP Annals*. 60 (2011) 735–755. <https://doi.org/10.1016/J.CIRP.2011.05.005>.
- [10] F. Warkusz, Electrical and mechanical properties of thin metal films: Size effects, *Prog Surf Sci*. 10 (1980) 287–382. [https://doi.org/10.1016/0079-6816\(80\)90003-9](https://doi.org/10.1016/0079-6816(80)90003-9).
- [11] Y.F. Lu, M. Takai, S. Komuro, T. Shiokawa, Y. Aoyagi, Surface cleaning of metals by pulsed-laser irradiation in air, 1994.
- [12] W.M. Steen, J. Mazumder, *Laser material processing*, (2010) 558. https://books.google.com/books/about/Laser_Material_Processing.html?id=gPsq0HHAU4UC (accessed June 25, 2022).
- [13] M. Kasuga, T. Sano, A. Hirose, Grain refining in weld metal using short-pulsed laser ablation during CW laser welding of 2024-T3 aluminum alloy, *International Journal of Extreme Manufacturing*. 1 (2019) 045003. <https://doi.org/10.1088/2631-7990/AB563A>.
- [14] M.S. Brown, C.B. Arnold, *Fundamentals of Laser-Material Interaction and Application to Multiscale Surface Modification*, Springer Series in Materials Science. 135 (2010) 91–120. https://doi.org/10.1007/978-3-642-10523-4_4/COVER/.
- [15] T.H. MAIMAN, Stimulated Optical Radiation in Ruby, *Nature*. 187 (1960) 493–494. <https://doi.org/10.1038/187493a0>.
- [16] Joan Lisa Bromberg, *The Laser in America*, MIT Press. (1991). https://books.google.ca/books?hl=en&lr=&id=P6Ta1MPiOM8C&oi=fnd&pg=PR7&dq=Bromberg,+J.+The+Laser+in+America,+1950%E2%80%931970%3B+MIT+Press:+Cambridge,+MA,+1991%3B+p+202.&ots=83zHGkQr_w&sig=It47XRwH6jUkZZ8EMFAYtRSsCK0#v=onepage&q&f=false (accessed June 25, 2022).
- [17] D. Zhang, L. Guan, Laser Ablation, in: *Comprehensive Materials Processing*, Elsevier Ltd, 2014: pp. 125–169. <https://doi.org/10.1016/B978-0-08-096532-1.00406-4>.
- [18] J. Mazumder, Laser Welding: State of the Art Review, *JOM*. 34 (1982) 16–24. <https://doi.org/10.1007/BF03338045>.

- [19] S.K. Lee, S.J. Na, KrF excimer laser ablation of thin Cr film on glass substrate, *Appl. Phys. A*. 68 (1999) 417–423. <https://doi.org/10.1007/s003399900007>.
- [20] G.Y.; T.D.J.; H.E.C. Liu, Evaluation of excimer laser ablation of thin Cr film on glass substrate by analysing acoustic emission, *Opt Lasers Eng.* (2004). <https://www.hanspub.org/reference/ReferencePapers.aspx?ReferenceID=14025&&PaperID=11814> (accessed June 25, 2022).
- [21] F. Brandi, N. Burdet, R. Carzino, A. Diaspro, Very large spot size effect in nanosecond laser drilling efficiency of silicon, *Opt Express*. 18 (2010) 23488. <https://doi.org/10.1364/OE.18.023488>.
- [22] S. Ravi-Kumar, B. Lies, X. Zhang, H. Lyu, H. Qin, Laser ablation of polymers: a review, *Polym Int*. 68 (2019) 1391–1401. <https://doi.org/10.1002/pi.5834>.
- [23] R. Paschotta, *Encyclopedia of Laser Physics and Technology*, RP Photonics. (2017). <https://www.rp-photonics.com/encyclopedia.html> (accessed June 25, 2022).
- [24] A. Laskin, P. Kaiser, V. Laskin, A. Ostrun, Laser beam shaping for biomedical microscopy techniques, <https://doi.org/10.1117/12.2217927>. 9887 (2016) 251–260. <https://doi.org/10.1117/12.2217927>.
- [25] W. Wang, X. Mei, G. Jiang, S. Lei, C. Yang, Effect of two typical focus positions on microstructure shape and morphology in femtosecond laser multi-pulse ablation of metals, *Appl Surf Sci*. 255 (2008) 2303–2311. <https://doi.org/10.1016/j.apsusc.2008.07.100>.
- [26] Z.K. Wang, W.L. Seow, X.C. Wang, H.Y. Zheng, Effect of laser beam scanning mode on material removal efficiency in laser ablation for micromachining of glass, *J Laser Appl*. 27 (2015) S28004. <https://doi.org/10.2351/1.4906475>.
- [27] E. Kaselouris, I.K. Nikolos, Y. Orphanos, E. Bakarezos, N.A. Papadogiannis, M. Tatarakis, V. Dimitriou, A Review of Simulation Methods of Laser Matter Interactions Focused on Nanosecond Laser Pulsed Systems, <http://dx.doi.org/10.1142/S1756973713300013>. 05 (2015) 1330001. <https://doi.org/10.1142/S1756973713300013>.

- [28] I. Bozsóki, B. Balogh, P. Gordon, 355 nm nanosecond pulsed Nd:YAG laser profile measurement, metal thin film ablation and thermal simulation, *Opt Laser Technol.* 43 (2011) 1212–1218. <https://doi.org/10.1016/J.OPTLASTEC.2011.03.011>.
- [29] B.J. Garrison, T.E. Itina, L. v. Zhigilei, Limit of overheating and the threshold behavior in laser ablation, *Phys Rev E.* 68 (2003) 041501. <https://doi.org/10.1103/PhysRevE.68.041501>.
- [30] M. Follstaedt, J.E. E Baglin B R Appleton, G.K. Celler, Laser and Electron Beam Interactions with Solids, *MRS Bulletin* 1982 7:1. 7 (2013) 4–5. <https://doi.org/10.1557/S0883769400049460>.
- [31] IPG Photonics, (n.d.). [https://www.ipgphotonics.com/cn/products/lasers/pico-femtosecond-fiber-lasers/1-03-1-06-micron/yfpp-5-20-ps-series#\[vs\]](https://www.ipgphotonics.com/cn/products/lasers/pico-femtosecond-fiber-lasers/1-03-1-06-micron/yfpp-5-20-ps-series#[vs]) (accessed June 28, 2022).
- [32] J. Zhang, R. Qin, W. Zhu, J. Vorberger, Energy Relaxation and Electron–Phonon Coupling in Laser-Excited Metals, *Materials.* 15 (2022). <https://doi.org/10.3390/MA15051902>.
- [33] X. Liu, D. Du, G. Mourou, Laser ablation and micromachining with ultrashort laser pulses, *IEEE J Quantum Electron.* 33 (1997) 1706–1716. <https://doi.org/10.1109/3.631270>.
- [34] D.J. Elliott, Ultraviolet laser technology and applications, (1995) 350. https://books.google.com/books/about/Ultraviolet_Laser_Technology_and_Applica.html?id=6-tRAAAAMAAJ (accessed June 28, 2022).
- [35] Y. Cao, X. Zeng, Z. Cai, J. Duan, Laser micro/nano-fabrication techniques and their applications in electronics, *Advances in Laser Materials Processing: Technology, Research and Application.* (2010) 629–670. <https://doi.org/10.1533/9781845699819.7.629>.
- [36] F. Kokai, H. Niino, A. Yabe, Laser ablation of polysulfone films: a laser ionization TOF mass spectrometric study, *Applied Physics A* 1998 67:5. 67 (1998) 607–612. <https://doi.org/10.1007/S003390050831>.

- [37] S. Kon, K. Oldham, R. Horowitz, Piezoresistive and piezoelectric MEMS strain sensors for vibration detection, *Sensors and Smart Structures Technologies for Civil, Mechanical, and Aerospace Systems* 2007. 6529 (2007) 65292V. <https://doi.org/10.1117/12.715814>.
- [38] J. Li, J. Longtin, S. Tankiewicz, ... A.G.-S. and A.A., undefined 2007, Interdigital capacitive strain gauges fabricated by direct-write thermal spray and ultrafast laser micromachining, Elsevier. (n.d.).
https://www.sciencedirect.com/science/article/pii/S0924424706002883?casa_token=g5yjD8VIC70AAAAA:LI9OVr5dwM2Aa0yRZo5t35S1p-ZZncavUZxDHVeptnNALECyNCVAvAb0lVHR-VROuhHt5HLwot4 (accessed July 30, 2022).
- [39] K. Hoffmann, *An introduction to measurements using strain gages*, (1989).
https://www.academia.edu/download/44775005/An_Introduction_to_Measurements_using_Strain_Gages.pdf (accessed July 26, 2022).
- [40] H. Liu, Q. Li, S. Zhang, R. Yin, X. Liu, Y. He, K. Dai, C. Shan, J. Guo, C. Liu, C. Shen, X. Wang, N. Wang, Z. Wang, R. Wei, Z. Guo, Electrically conductive polymer composites for smart flexible strain sensors: a critical review, *J Mater Chem C Mater*. 6 (2018) 12121–12141. <https://doi.org/10.1039/C8TC04079F>.
- [41] M. Amjadi, A. Pichitpajongkit, S. Lee, S. Ryu, I. Park, Highly stretchable and sensitive strain sensor based on silver nanowire-elastomer nanocomposite, *ACS Nano*. 8 (2014) 5154–5163. <https://doi.org/10.1021/NN501204T>.
- [42] A. Qiu, P. Li, Z. Yang, Y. Yao, I. Lee, J. Ma, A Path Beyond Metal and Silicon: Polymer/Nanomaterial Composites for Stretchable Strain Sensors, *Adv Funct Mater*. 29 (2019) 1806306. <https://doi.org/10.1002/ADFM.201806306>.
- [43] *Theory and Design for Mechanical Measurements* - Richard S. Figliola, Donald E. Beasley - Google Books, (n.d.).
<https://books.google.ca/books?hl=en&lr=&id=kh7zDwAAQBAJ&oi=fnd&pg=PA1&dq=R.+S.+Figliola,+D.+Beasley,+Theory+and+Design+for+Mechanical+Measurements,+John+Wiley+%26+Sons,+New+York+2015&ots=fhtlLsIIjC&sig=Ssgxa9sFWmULxaPpbjJ6V7kk4ho#v=onepage&q=gauge%20factor&f=false> (accessed July 27, 2022).

- [44] H. Souri, H. Banerjee, A. Jusufi, N. Radacsi, A.A. Stokes, I. Park, M. Sitti, M. Amjadi, Wearable and Stretchable Strain Sensors: Materials, Sensing Mechanisms, and Applications, *Advanced Intelligent Systems*. 2 (2020) 2000039. <https://doi.org/10.1002/AISY.202000039>.
- [45] M. Brauwers, F. Brouers, Temperature and strain effect on electrical resistivity of transition metal alloys: application to strain gauges, *Journal of Physics F: Metal Physics*. 6 (1976) 1331. <https://doi.org/10.1088/0305-4608/6/7/014>.
- [46] K. Arshak, D. Morris, A. Arshak, O. Korostynska, Development of high sensitivity oxide based strain gauges and pressure sensors, *Journal of Materials Science: Materials in Electronics*. 17 (2006) 767–778. <https://doi.org/10.1007/S10854-006-0013-4>.
- [47] Y. Wang, L. Wang, T. Yang, X. Li, X. Zang, M. Zhu, K. Wang, D. Wu, H. Zhu, Wearable and Highly Sensitive Graphene Strain Sensors for Human Motion Monitoring, *Adv Funct Mater*. 24 (2014) 4666–4670. <https://doi.org/10.1002/ADFM.201400379>.
- [48] C. Yan, J. Wang, W. Kang, M. Cui, X. Wang, C.Y. Foo, K.J. Chee, P.S. Lee, Highly Stretchable Piezoresistive Graphene–Nanocellulose Nanopaper for Strain Sensors, *Advanced Materials*. 26 (2014) 2022–2027. <https://doi.org/10.1002/ADMA.201304742>.
- [49] M. Amjadi, K.U. Kyung, I. Park, M. Sitti, Stretchable, Skin-Mountable, and Wearable Strain Sensors and Their Potential Applications: A Review, *Adv Funct Mater*. 26 (2016) 1678–1698. <https://doi.org/10.1002/ADFM.201504755>.
- [50] D. Rus, M.T. Tolley, Design, fabrication and control of soft robots, *Nature* 2015 521:7553. 521 (2015) 467–475. <https://doi.org/10.1038/nature14543>.
- [51] C. Wang, K. Xia, H. Wang, X. Liang, Z. Yin, Y. Zhang, Advanced Carbon for Flexible and Wearable Electronics, *Advanced Materials*. 31 (2019). <https://doi.org/10.1002/adma.201801072>.
- [52] D.J. Lichtenwalner, A.E. Hydrick, A.I. Kingon, Flexible thin film temperature and strain sensor array utilizing a novel sensing concept, *Sens Actuators A Phys*. 135 (2007) 593–597. <https://doi.org/10.1016/J.SNA.2006.07.019>.

- [53] J.U. Lind, M. Yadid, I. Perkins, B.B. O'Connor, F. Eweje, C.O. Chantre, M.A. Hemphill, H. Yuan, P.H. Campbell, J.J. Vlassak, K.K. Parker, Cardiac microphysiological devices with flexible thin-film sensors for higher-throughput drug screening, *Lab Chip*. 17 (2017) 3692–3703. <https://doi.org/10.1039/C7LC00740J>.
- [54] Evanohm® R Strip and Foil | Re-rolled Strip and Thin Foil with High electrical resistivity, (n.d.). <https://www.hpmetals.com/products/materials/evanohm-r-strip-foil> (accessed July 28, 2022).
- [55] D. Depla, S. Mahieu, J.E. Greene, Sputter Deposition Processes, *Handbook of Deposition Technologies for Films and Coatings*. (2010) 253–296. <https://doi.org/10.1016/B978-0-8155-2031-3.00005-3>.
- [56] I.H. Kazi, P.M. Wild, T.N. Moore, M. Sayer, Characterization of sputtered nichrome (Ni-Cr 80/20 wt.%) films for strain gauge applications, *Thin Solid Films*. 515 (2006) 2602–2606. <https://doi.org/10.1016/j.tsf.2005.10.077>.
- [57] Y.H. Kwak, J. Kim, K. Kim, Sleep monitoring sensor using flexible metal strain gauge, *Jpn J Appl Phys*. 57 (2018) 05GD03. <https://doi.org/10.7567/JJAP.57.05GD03/XML>.
- [58] R. Matsuzaki, T. Keating, A. Todoroki, N. Hiraoka, Rubber-based strain sensor fabricated using photolithography for intelligent tires, *Sens Actuators A Phys*. 148 (2008) 1–9. <https://doi.org/10.1016/J.SNA.2008.08.001>.
- [59] S. Khan, L. Lorenzelli, R.S. Dahiya, Technologies for printing sensors and electronics over large flexible substrates: A review, *IEEE Sens J*. 15 (2015) 3164–3185. <https://doi.org/10.1109/JSEN.2014.2375203>.
- [60] J. Li, J.P. Longtin, S. Tankiewicz, A. Gouldstone, S. Sampath, Interdigital capacitive strain gauges fabricated by direct-write thermal spray and ultrafast laser micromachining, *Sens Actuators A Phys*. 133 (2007) 1–8. <https://doi.org/10.1016/j.sna.2006.04.008>.
- [61] O. Suttmann, J.F. Duesing, J. Koch, L. Overmeyer, Laser patterning of thin film strain gauges, *ICALEO 2013 - 32nd International Congress on Applications of Lasers and Electro-Optics*. 877 (2013) 877–881. <https://doi.org/10.2351/1.5062983>.

- [62] Q. Bian, X. Yu, B. Zhao, Z. Chang, S. Lei, Femtosecond laser ablation of indium tin-oxide narrow grooves for thin film solar cells, *Opt Laser Technol.* 45 (2013) 395–401. <https://doi.org/10.1016/j.optlastec.2012.06.018>.
- [63] M. Esakkimuthu, S. Balakrishnapillai Suseela, R. Sankararajan, A. Gupta, G. Rana, Laser Patterning of Thin Film Copper and ITO on Flexible Substrates for Terahertz Antenna Applications, *JLMN-Journal of Laser Micro/Nanoengineering.* 12 (2017). <https://doi.org/10.2961/jlmn.2017.03.0023>.
- [64] M.D. Dankoco, E. Bènevent, E. Bergeret, L. Gallais, M. Bendahan, Temperature sensor on flexible substrate patterned by laser ablation, *Conference Proceedings - 10th International Conference on Advanced Semiconductor Devices and Microsystems, ASDAM 2014.* (2014) 9–12. <https://doi.org/10.1109/ASDAM.2014.6998634>.
- [65] P.S. Das, A. Chhetry, P. Maharjan, M.S. Rasel, J.Y. Park, A laser ablated graphene-based flexible self-powered pressure sensor for human gestures and finger pulse monitoring, *Nano Research* 2019 12:8. 12 (2019) 1789–1795. <https://doi.org/10.1007/S12274-019-2433-5>.
- [66] J. Duesing, O. Suttman, J. Koch, ... U.S.-J. of L.M., undefined 2012, Ultrafast laser patterning of thin films on 3-D shaped surfaces for strain sensor applications, *Jlps.Gr.Jp.* 7 (2012). <https://doi.org/10.2961/jlmn.2012.03.0014>.
- [67] J. Düsing, T. Eichele, J. Koch, ... O.S.-P., undefined 2014, Laser surface processing of integrated thin film systems on arbitrarily shaped components, Elsevier. (n.d.). <https://www.sciencedirect.com/science/article/pii/S2212017314001789> (accessed July 28, 2022).
- [68] M.S. Brown, C.B. Arnold, *Laser Precision Microfabrication*, 135 (2010) 91–120. <https://doi.org/10.1007/978-3-642-10523-4>.
- [69] F. Brygo, C. Dutouquet, F. le Guern, R. Oltra, A. Semerok, J.M. Weulersse, Laser fluence, repetition rate and pulse duration effects on paint ablation, *Appl Surf Sci.* 252 (2006) 2131–2138. <https://doi.org/10.1016/j.apsusc.2005.02.143>.

- [70] P.D. Enrique, C. DiGiovanni, N. Mao, R. Liang, S. Peterkin, N.Y. Zhou, Resistance is not futile: The use of projections for resistance joining of metal additively and conventionally manufactured parts, *J Manuf Process*. 66 (2021) 424–434.
<https://doi.org/10.1016/J.JMAPRO.2021.04.035>.
- [71] C. von der Heide, M. Grein, G. Bräuer, A. Dietzel, Methodology of selective metallic thin film ablation from susceptible polymer substrate using pulsed femtosecond laser, *Opt Express*. 28 (2020) 33413. <https://doi.org/10.1364/OE.391084>.
- [72] A. Dietzel, C. von der Heide, G. Bräuer, M. Grein, Methodology of selective metallic thin film ablation from susceptible polymer substrate using pulsed femtosecond laser, *Optics Express*, Vol. 28, Issue 22, Pp. 33413-33432. 28 (2020) 33413–33432.
<https://doi.org/10.1364/OE.391084>.
- [73] S.I. ANISIMOV, VAPORIZATION OF METAL ABSORBING LASER RADIATION, (1996) 14–15. https://doi.org/10.1142/9789814317344_0002.
- [74] S. Harimkar, A. Samant, N.D.-J. of A. Physics, undefined 2007, Temporally evolved recoil pressure driven melt infiltration during laser surface modifications of porous alumina ceramic, *Aip.Scitation.Org*. 101 (2007) 54911.
<https://doi.org/10.1063/1.2710288>.
- [75] H.D. Vora, S. Santhanakrishnan, S.P. Harimkar, S.K.S. Boetcher, N.B. Dahotre, One-dimensional multipulse laser machining of structural alumina: Evolution of surface topography, *International Journal of Advanced Manufacturing Technology*. 68 (2013) 69–83. <https://doi.org/10.1007/s00170-012-4709-8>.
- [76] R. Srinivasan, *Ablation of Polymers and Biological Tissue by Ultraviolet Lasers*, 1986.
- [77] J.H. Brannon, J.R. Lankard, A.I. Baise, F. Burns, J. Kaufman, Excimer laser etching of polyimide, *J Appl Phys*. 58 (1998) 2036. <https://doi.org/10.1063/1.336012>.
- [78] C.A. Aguilar, Y. Lu, S. Mao, S. Chen, Direct micro-patterning of biodegradable polymers using ultraviolet and femtosecond lasers, *Biomaterials*. 26 (2005) 7642–7649.
<https://doi.org/10.1016/j.biomaterials.2005.04.053>.
- [79] J.M. Liu, Simple technique for measurements of pulsed Gaussian-beam spot sizes, 1982.

- [80] B. Neuenschwander, B. Jaeggi, M. Schmid, A. Dommann, A. Neels, T. Bandi, G. Hennig, Factors controlling the incubation in the application of ps laser pulses on copper and iron surfaces, in: *Laser Applications in Microelectronic and Optoelectronic Manufacturing (LAMOM) XVIII*, SPIE, 2013: p. 86070D. <https://doi.org/10.1117/12.2004136>.
- [81] M.F. Becker, R.M. Walser, Y. Jee, Laser-induced damage on single-crystal metal surfaces, *JOSA B*, Vol. 5, Issue 3, Pp. 648-659. 5 (1988) 648–659. <https://doi.org/10.1364/JOSAB.5.000648>.
- [82] P.T. Mannion, J. Magee, E. Coyne, G.M. O’Connor, T.J. Glynn, The effect of damage accumulation behaviour on ablation thresholds and damage morphology in ultrafast laser micro-machining of common metals in air, *Appl Surf Sci*. 233 (2004) 275–287. <https://doi.org/10.1016/J.APSUSC.2004.03.229>.
- [83] F. di Niso, C. Gaudiuso, T. Sibillano, F.P. Mezzapesa, A. Ancona, P.M. Lugarà, Role of heat accumulation on the incubation effect in multi-shot laser ablation of stainless steel at high repetition rates, *Opt Express*. 22 (2014) 12200. <https://doi.org/10.1364/oe.22.012200>.
- [84] A. Ancona, A. Tünnermann, F. Röser, J. Limpert, K. Rademaker, S. Nolte, High speed laser drilling of metals using a high repetition rate, high average power ultrafast fiber CPA system, *Optics Express*, Vol. 16, Issue 12, Pp. 8958-8968. 16 (2008) 8958–8968. <https://doi.org/10.1364/OE.16.008958>.
- [85] F. Dausinger, F. Lichter, H. Lubatschowski, Plasma evolution during metal ablation with ultrashort laser pulses, *Optics Express*, Vol. 13, Issue 26, Pp. 10597-10607. 13 (2005) 10597–10607. <https://doi.org/10.1364/OPEX.13.010597>.
- [86] Resistalloy International Resistalloy 8020 Nickel Chromium Electrical Resistance Alloy, (n.d.). <https://www.matweb.com/search/DataSheet.aspx?MatGUID=eb55974581ca4a74b3d72aed2ba8c4cd&ckck=1> (accessed July 19, 2022).
- [87] Heat Transfer Module User’s Guide, 1998. www.comsol.com/blogs.
- [88] Z.H. Dong, D. Sergeev, D. Kobertz, N. D’Souza, S. Feng, M. Müller, H.B. Dong, Vaporization of Ni, Al and Cr in Ni-Base Alloys and Its Influence on Surface Defect

- Formation During Manufacturing of Single-Crystal Components, *Metall Mater Trans A Phys Metall Mater Sci.* 51 (2020) 309–322. <https://doi.org/10.1007/S11661-019-05498-1/FIGURES/11>.
- [89] E. Kannatey-Asibu, *Principles of laser materials processing*, (2009) 819.
- [90] Nickel - Melting Point - Boiling Point | nuclear-power.com, (n.d.). <https://www.nuclear-power.com/nickel-melting-point-boiling-point/> (accessed July 20, 2022).
- [91] UV Laser Marking | Knowledge | Laser Marking Basics | KEYENCE Canada, (n.d.). <https://www.keyence.ca/ss/products/marketing/lasermarker/knowledge/uv-laser.jsp> (accessed July 19, 2022).
- [92] C.A. Aguilar, Y. Lu, S. Mao, S. Chen, Direct micro-patterning of biodegradable polymers using ultraviolet and femtosecond lasers, *Biomaterials.* 26 (2005) 7642–7649. <https://doi.org/10.1016/J.BIOMATERIALS.2005.04.053>.
- [93] L. Wang, Z. Wang, A.N. Bakhtiyari, H. Zheng, A Comparative Study of Laser-Induced Graphene by CO₂ Infrared Laser and 355 nm Ultraviolet (UV) Laser, *Micromachines* 2020, Vol. 11, Page 1094. 11 (2020) 1094. <https://doi.org/10.3390/MII11121094>.
- [94] M.S. Brown, C.B. Arnold, *Fundamentals of Laser-Material Interaction and Application to Multiscale Surface Modification*, in: *Laser Precision Microfabrication*, 2010: pp. 91–120. <https://doi.org/10.1007/978-3-642-10523-4>.
- [95] S. Besner, M. Meunier, *Laser Synthesis of Nanomaterials*, in: K. Sugioka, M. Meunier, A. Piqué (Eds.), *Springer Berlin Heidelberg*, Berlin, Heidelberg, 2010: pp. 163–187. https://doi.org/10.1007/978-3-642-10523-4_7.
- [96] Hewlett-Packard Co., *Practical Strain Gage Measurements*. Application Note 290-1, Hewlett-Packard Co., Palo Alto, California, 1981.
- [97] G.R. Witt, The electromechanical properties of thin films and the thin film strain gauge, *Thin Solid Films.* 22 (1974) 133–156. [https://doi.org/10.1016/0040-6090\(74\)90001-7](https://doi.org/10.1016/0040-6090(74)90001-7).
- [98] H. Jung, C. Park, H. Lee, S. Hong, H. Kim, S.J. Cho, Nano-Cracked Strain Sensor with High Sensitivity and Linearity by Controlling the Crack Arrangement, *Sensors.* 19 (2019) 2834. <https://doi.org/10.3390/s19122834>.

- [99] Vishay Precision Group, *Fatigue Characteristics of Micro-Measurements Strain Gages*, 2010.
- [100] O. Kraft, R. Schwaiger, P. Wellner, *Fatigue in thin films: Lifetime and damage formation*, *Materials Science and Engineering A*. 319–321 (2001) 919–923.
[https://doi.org/10.1016/S0921-5093\(01\)00990-X](https://doi.org/10.1016/S0921-5093(01)00990-X).
- [101] G.P. Zhang, C.A. Volkert, R. Schwaiger, P. Wellner, E. Arzt, O. Kraft, *Length-scale-controlled fatigue mechanisms in thin copper films*, *Acta Mater.* 54 (2006) 3127–3139.
<https://doi.org/10.1016/j.actamat.2006.03.013>.
- [102] B.J. Kim, H.A.S. Shin, I.S. Choi, Y.C. Joo, *Electrical failure and damage analysis of multi-layer metal films on flexible substrate during cyclic bending deformation*, *Proceedings of the International Symposium on the Physical and Failure Analysis of Integrated Circuits, IPFA*. (2011). <https://doi.org/10.1109/IPFA.2011.5992725>.
- [103] X.M. Luo, B. Zhang, G.P. Zhang, *Fatigue of metals at nanoscale: Metal thin films and conductive interconnects for flexible device application*, *Nano Materials Science*. 1 (2019) 198–207. <https://doi.org/10.1016/J.NANOMS.2019.02.003>.